Doctoral Thesis at NTNU 2006:66

- **ISBN 82-471-7881-8 (electronic)**
- **ISBN 82-471-7882-6 (printed)**

Krishna Prasad Aryal

Slope Stability Evaluations by Limit Equilibrium and Finite Element Methods

Norwegian University of Science and Technology
Faculty of Engineering Science and Technology
Department of Civil and Transport Engineering

Krishna Prasad Aryal

Slope Stability Evaluations by Limit Equilibrium and Finite Element Methods

Trondheim, April 2006

Thesis submitted to the Faculty of Engineering Science and Technology, Norwegian University of Science and Technology in partial fulfilments of the requirements for the degree of philosophiae doctor in civil engineering.

Norwegian University of Science and Technology
Faculty of Engineering Science and Technology
Department of Civil and Transport Engineering
Geotechnical Division, Trondheim, Norway

The committee for the appraisal of this thesis was comprised of the following members:

Professor Dr. Sven Knutsson
Department of Civil, Mining and Environmental Engineering
Luleå University of Technology, Sweden

Dr. ing. Signe Kirkebø
Multiconsult, Oslo, Norway

Professor emeritus Kåre Senneset (administrator)
Norwegian University of Science and Technology, Trondheim, Norway

---

The thesis was supervised by the following Professors:

Associate Professor, dr. ing. Rolf Sandven (main adviser)
NTNU, Geotechnical Division, Trondheim

Professor, dr. ing. Lars Grande (co-adviser)
NTNU, Geotechnical Division, Trondheim

Professor, dr. ing. Steinar Nordal (co-adviser)
NTNU, Geotechnical Division, Trondheim

The thesis is dedicated to my parents.

Acknowledgement

The work presented in this thesis has been carried out at the Geotechnical Division, Department of Civil and Transport Engineering, Norwegian University of Science and Technology, NTNU under the supervision of Associate Professor Rolf Sandven as the main adviser and Professors Lars Grande and Steinar Nordal as co-advisers. I am very grateful to their valuable guidance, discussions and encouragement throughout the study period. All kinds of contributions from them for this study are highly appreciated. Appreciation by words is not sufficient to adviser Rolf Sandven who not only encouraged to apply, but also made the study successfully complete.

I would also like to thank Assistant Professor Arnfinn Emdal for his valuable feedbacks, suggestions and comments during the PhD seminars and study period. Assistance from Kjell Roksvåg and Jan Jønland during the laboratory investigations is highly appreciated. Without their cooperation, the laboratory investigation works would have been incomplete. I am also thankful to PhD colleagues in the division, including Shaoli Yang, Tewodros Tefera and Gustav Grimstad for their cooperation and creating a good working environment.

I am very much thankful to Marit Skjåk-Bræk, administrative adviser in the division, for facilitating all kind of practical and personal matters. Her kindness and excellent management skills are remarkable. Moreover, I would like to express my thanks to all the staff in the division and SINTEF geotechnical engineering for spending time in a good environment. Thus, the study period in the University, in particular the memorable time at the Division, has been very interesting and most valuable in my professional and academic carrier.

The author would like to appreciate the permission given by then Project Director Mr. Shashi Raj Shrestha, NEA, and then Project Manager Mr. Martin Buchli, Fichtner JV, for the case study from the MMHEP Nepal. The Fichtner JV Project Manager, Engineers and Engineering Geologists are appreciated for their cooperation. Feedbacks from Dr. Mike Long, University College of Dublin, are greatly acknowledged. The author is also thankful to those whose names are not mentioned here, but have their direct or indirect contributions to this study.

This study was made possible by the scholarship grant from the Faculty of Engineering Science and Technology, NTNU. A special appreciation goes to the Faculty Director, Erik Lund and to the adviser, Rolf Sandven who selected me as a research fellow in the Geotechnical Division.

Finally, I would like to thank my wife, Nirmala for her encouragement for the study. Her patience and hardship of taking home responsibility are highly appreciable. Similarly, my son, Sanjay and daughter, Seema are acknowledged for their good understanding about their father's absence and late arrival home from the University.

Krishna Prasad Aryal
Trondheim, Norway
April 2006

Abstract of the Thesis

This thesis deals with slope stability evolutions carried out by commonly used limit equilibrium (LE) and finite element (FE) methods. The study utilizes two LE based software (SLOPE/W and SLIDE) and one FE based software (PLAXIS). The principal difference between these two analyses approaches is that the LE methods are based on the static of equilibrium whereas FE methods utilise the stress-strain relationship or constitutive law.

To fulfil one of the aims of the study, the LE based methods are compared based on the factor of safety (FOS) obtained for various load combinations. The comparison is mainly based on simplified slope geometry and assumed input parameters. Among the LE methods, the Bishop simplified (BS), Janbu simplified (JS) and Janbu GPS methods are compared with the Morgenstern-Price method (M-PM). The two latter methods satisfy both force and moment equilibriums. In addition, M-PM allows a variable interslice force function. These LE methods are well established for many years, and thus some of them are still commonly used in practice for stability analysis. Simplicity and relatively good results are the advantages of these methods.

The comparative study among the LE methods shows that BSM is as good as M-PM for normal condition in circular shear surface (SS) analysis. Similarly, JSM is as good as M-PM for plane SS analysis. Moreover, the study shows that BSM is insensitive to interslice forces in circular SS analysis, whereas JSM is insensitive to interslice forces in plane SS analysis. This is true for the analyses without any external forces acting in slopes. With some external forces, both methods may be sensitive to the interslice force function, and thus the analyses may result in either higher or lower FOS compared with M-PM. Even if the M-PM assumes an interslice force function in analysis, the method is found suitable, because the method satisfies both force and moment equilibrium conditions. The comparison between Janbu's GPS method and the M-PM shows a very good agreement with nominal difference (<2%) in the FOS.

Moreover, the M-PM has been compared with results from the FE analyses. Compared with the FE (PLAXIS) analyses, the LE (M-PM) analyses may estimate 5 – 14% higher FOS, depending on the conditions of a dry slope and a fully saturated slope with hydrostatic pore pressure distributions. For fully saturated conditions in the slope, inaccurate computation of stresses in LE methods may have resulted in larger difference in the computed FOS.

Since, the FE software is based on stress-strain relationship, stress redistributions are surely better computed even for a complicated problem. This has been found one of the advantages in FE simulations. A parameter study shows that the application of a positive dilatancy angle in FE analysis can significantly improve the FOS (4 - 10%). On contrast, the shear surface optimization in LE (M-PM in SLOPE/W) analysis results in lower FOS, and thus minimizing the difference in FOS compared with FE analysis. Thus, the optimisation of the circular SS in LE analyses and application of dilatancy angle in FE analyses may provide very good agreement in FOS keeping the variations less than 5%.

Instability of natural and built-in slopes has been a serious geotechnical challenge, particularly in mountainous countries like Nepal, where a large number of water-induced disasters are experienced every year. Since the country lies in a relatively active earthquake zone, earthquake events may adversely affect the long-term stability of slopes along the highways, around hydropower installations and elsewhere. The selected case study from the Middle Marsyangdi Hydroelectric Project (MMHEP) in Nepal was carried out, focusing on both the groundwater and earthquake effects on long-term stability of slopes. In addition, the analyses were performed for pore pressure distributions by seepage analyses and pseudo-static and dynamic earthquake events imposed in the case slopes.

Another important contribution of this study has been the investigations of the shear strength parameters for the case study slopes. The investigation ranges from the basic index tests, which were carried out to characterize material properties and establish a basis for building-in the test specimens, to the most advanced triaxial tests. Additionally, both consolidated drained and undrained triaxial tests were conducted, aiming to find any differences in the strength parameters. A total of twenty-four triaxial tests from four different soil samples, taken from the case study slopes, were conducted to define the Mohr-Coulomb failure envelope, and thus obtained the effective shear strength parameters (c', ϕ') for stability evaluations. In addition, the coefficients of permeability were investigated as an important input for seepage analyses.

Two slopes, one located at the dam site and the other at the powerhouse of the MMHEP, were evaluated for long-term stability conditions. The study, carried out using the monitored groundwater table, reveals that the groundwater is the potential destabilizing factor in the slopes. Both hydrostatic pore pressure distributions with phreatic surface correction and seepage analysis were carried out in the stability analysis. The pore pressure distributions from the seepage analyses indicated critically stable slopes particularly at the toe areas. However, a significant improvement in the FOS was found with lowered groundwater table. Moreover, the study, carried out for the pseudo-static analysis with the selected earthquake acceleration coefficient, shows that otherwise stable slopes become critical in earthquake events. However, the case slopes were found to have higher FOS than the recommended minimum value for such conditions. The dynamic earthquake simulations indicate both positive excess pore pressure and suction developed during the earthquakes. The applied earthquake acceleration of 0.15g (35% of PGA, where PGA = 4.2 m/s^2)) shows critical conditions in the slopes. Moreover, larger accumulated displacements were found close to the slope surface compared to the inner side of the slopes. In addition, the dynamic analyses further indicate plastic points all over the slopes and increased shear strains in a particular location.

Nevertheless, the difference in FOS found from the LE and FE analyses may have a little interest, if there is a large uncertainty in the input parameters. Therefore, priority should be given to investigate the shear strength parameters and precise mapping of the slope geometry before selecting an appropriate analysis method. Most preferably, a slope should be analyzed by FE methods, else otherwise by LE based M-PM or GPS method with investigated input parameters.

List of Symbols and Abbreviations

Greek symbols

α	angle of the sliding plane
α	Rayleigh α-coefficient
α_h	horizontal earthquake coefficient
α_t	angle of inclination of the line of thrust defined in GPS method
β	Rayleigh β-coefficient
β	slope inclination angle
ε_1	major principal strain, axial strain in a triaxial test
ε_3	minor principle strain, radial strain in a triaxial test
ε_a	axial strain in a triaxial test
ε_f	axial strain at failure in a triaxial test
ε_q	shear strain
ε_r	radial strain in a triaxial test
ε_v	volumetric strain
ϕ	angle of friction
ϕ'	effective angle of friction
ϕ^b	angle indicating rate of increase in shear strength relative to the matrix suction
γ	bulk unit weight of soil (kN/m^3)
γ_d	dry unit weight of soil (kN/m^3)
γ_w	unit weight of water (kN/m^3)
λ	scale factor
$\lambda_{c\phi}$	dimensionless factor defined in JDM
ν	Poisson's ratio
ρ	mass density of soil (g/cm^3)
ρ_s	grain density of solids (g/cm^3)
Ψ	dilatancy angle
σ'	effective normal stress (kPa)
σ_1	total major principal stress ((kPa)
σ_1'	effective major principal stress ((kPa)
σ_3	total minor principle stress (kPa)
σ_3'	effective minor principal stress ((kPa)
σ_a	total axial stress (kPa)
σ_r	total radial stress (kPa)
σ_v	total vertical stress (kPa)

σ_{av} average total normal stress (kPa)

τ shear stress or mobilized shear stress (kPa)

τ_f shear strength of soil (kPa)

θ angle of inclination of interslice resultant force

ω_n natural angular frequency

ζ damping ratio

Roman symbols

a attraction defined as c/tanϕ (kPa)

b width of a slice

c apparent (total) cohesion (kPa)

c′ effective cohesion (kPa)

e void ratio

f yield function of Mohr-Coulomb model

f(x) interslice force function

g acceleration due to gravity (m/s^2)

g plastic potential function

h average height of a slice from the SS

h_t height from the mid point of the slice base to dE

k permeability coefficient (m/s)

l length of a slice or length of a specimen

n porosity of soils

n_{max} maximum porosity of soils

n_{min} minimum porosity of soils

p′ effective mean stress (kPa)

p_e effective stress in JDM (kPa)

p_d total stress in JDM (kPa)

q deviatoric stress (σ_a - $\sigma_{r)}$ (kPa)

q stress due to surcharge load (kPa)

r_u pore pressure ratio

u pore pressure (kPa)

u_a pore-air pressure (kPa)

u_w pore water pressure (kPa)

w moisture content

x length of moment arm

z depth of a slice to the SS

C	damping matrix (or damping coefficient)
C_c	critical damping coefficient
D	drained triaxial test (consolidated isotropically)
D_r	relative density of soil
E	interslice normal force (kN)
E_{50}	modulus defined by fifty percent strength (kPa)
E_{oed}	oedometer modulus (kPa)
E_{ref}	Young's modulus at reference stress (σ_v = 100 kPa) (kPa)
F	dynamic force (kN)
F	factor of safety
F_f	factor of safety for force equilibrium
F_m	factor of safety for moment equilibrium
G_{ref}	shear modulus at reference stress (σ_v = 100 kPa) (kPa)
L	total length of sliding surface or plane
H	depth of soil layer
H	total height of a slope from the toe
K	stiffness matrix (or stiffness as spring constant) (kN/m)
M	inertia matrix (or mass of soil body)
M_{sf}	incremental multiplier used in PLAXIS
N	base normal force acting on SS (kN)
N′	effective base normal force acting on SS (kN)
N_{cf}	stability number defined in JDM
P_r	relative porosity of soil
S	shear force acting at the base of a slice (kN)
S_a	available shear force (kN)
S_m	mobilized shear force (kN)
S_r	degree of saturation
T	interslice shear force (kN)
U	undrained triaxial test (consolidated isotropically)
V_p	compression wave velocity (m/s)
V_s	shear wave velocity (m/s)
W	weight of each slice or total sliding mass (kN)

Abbreviations

d1/d2	soil samples or layers for dam site slope
El.	elevation of ground surface or groundwater table
masl	meter above sea level
p1/p2	soil samples or layers for powerhouse slope
ASTM	American Society for Testing and Materials
BSM	Bishop's simplified method
CD	consolidated drained triaxial test (D)
CES	Consulting Engineers Salzgitter, GmbH, Germany
CSS	critical shear surface
CU	consolidated undrained triaxial test (U)
DHMN	Department of Hydrology and Meteorology, Nepal
DMGN	Department of Mines and Geology, Nepal
DPTCN	Development Project Technical Centre, Nepal
DUT	Delft University of Technology, the Netherlands
FE	finite element
FEM	finite element method
FOS	factor of safety
GLE	generalized limit equilibrium
GPS	general procedure of slices
GWh	gigawatt hour (a unit of energy)
GWT	ground water table
ICLD	International Commission on Large Dams
JCM	Janbu's corrected method
JDM	Janbu's direct method
JGM	Janbu's generalized method
JSM	Janbu's simplified method
JV	joint venture
KHP	Khimti Hydropower Plant
LB	left bank of dam site slope related to MMHEP
LE	limit equilibrium
LEM	limit equilibrium method
MIT	Massachusetts Institute of Technology
MMHEP	Middle Marsyangdi Hydroelectric Project
M-PM	Morgenstern-Price method
MWR	Ministry of Water Resources

NEA	Nepal Electricity Authority
NGI	Norwegian Geotechnical Institute
NS	Norwegian Standard
NTNU	Norwegian University of Science and Technology
OGL	original ground level
OM	Ordinary method (Fellenius or Swedish method)
OMC	optimum moisture content
PI	plasticity index
PGA	peak ground acceleration
PLAXIS	finite element software for geotechnical computations
PP	pore pressure
SEEP/W	finite element software for ground water (seepage) analysis
SINTEF	Stiftelsen for industriell og teknisk forskning ved Norges Tekniske Høgskole (English: Foundation for Scientific and Industrial Research at the Norwegian Institute of Technology in Norway)
SLIDE	limit equilibrium software for groundwater and slope stability analyses
SLOPE/W	limit equilibrium software for slope stability analysis
SM	Spencer's method
SS	shear surface
STABLE	geotechnical software for slope stability analysis
TU	Tribhuwan University, Nepal

Table of Contents

List of Appendices

List of Figures and Tables

List of Figures

List of Tables

Author's publications during the study period

1. Aryal, K. Sandven, R. and Nordal, S. (2005). *Limit Equilibrium and Finite Element Methods*. Proc. of the 16th Int. Conf. on Soil Mech. And Geotech. Engineering, 16 ICSMGE, Osaka, Japan, pp. 2471-76.
2. Aryal, K. and Sandven, R. (2005). *Risk evaluation of a slope and mitigation measures*: *A case study from Nepal*. Landslides and Avalanches, ICFL 2005, Norway, pp. 31-36.
3. Aryal, K., Rohde, J. K. and Sandven, R. (2004). *Slope Stability, Stabilization and Monitoring: A Case Study from Khimti Power Plant, Nepal.* Int. Conf. on Geosynthetics and Geoenvironmental Engineering, ICGGE – 2004, Bombay, India, pp. 100-05.

Chapter 1

Introduction

1.1 Background

Instability related issues in engineered as well as natural slopes are common challenges to both researchers and professionals. In construction areas, instability may result due to rainfall, increase in groundwater table and change in stress conditions. Similarly, natural slopes that have been stable for many years may suddenly fail due to changes in geometry, external forces and loss of shear strength (Abramson et al. 2002). Thielen et al. (2005) say, "The combination of intense rainfalls, steep topography and soil conditions are critical". Nepal has been facing challenges of large number of water-induced disasters such as landslides or slope failures mainly along the Highways. Likewise, Tayler & Burns (2005) say, "Earthquakes are the greatest threat to the long-term stability of slopes in earthquake active zones". In addition, the long-term stability is also associated with the weathering and chemical influences that may decrease the shear strength and create tension cracks. In such circumstances, the evaluation of slope stability conditions becomes a primary concern everywhere.

The engineering solutions to slope instability problems require good understanding of analytical methods, investigative tools and stabilisation measures (Abramson et al. 2002). According to Nash (1987), a quantitative assessment of the safety factor is important when decisions are made. Likewise, Chowdhury (1978) says, "The primary aim of slope stability analyses is to contribute to the safe and economic design of excavation, embankment and earth dams". Development activities may face great challenges due to unstable grounds. Similarly, the slope failure may interrupt the established imperative services like traffic movement, drinking water supply, power production and similar infrastructures. In this way, the main motivation of stability analyses is to save human lives, reduce property damages and provide continuous services. Therefore, the most suitable and reliable stability analysis methods have great scope and thus, they are increasingly demanding. The chosen method should be able to identify the existing safety conditions and suggest for technically feasible and economically viable solutions.

1.2 Scope and objective of the study

Like other mountainous countries, Nepal has large variations in its topography. The High Himalayas in the north, the gentle to steep mountains in the middle and the flat land in the south have provided both opportunities and challenges. Most of the development activities today are centred mainly in the cities and in the southern part of the country. On one hand, the infrastructures, such as roads, have been a great challenge to build and maintain, mainly because of the rugged topography with the steep slopes. Though there are many roads under construction and thus, Nepal may be regarded as "a museum of mountain roads" (Deoja 2000), the country has not been able to provide integrated road access network in mountainous region. On the other hand, the suitable topography and numerous rivers fed by glacial meltwater have provided the country with huge potential of more than 42 GW technically feasible hydropower installations (MWR 2003). Looking into the present developments, less than 2% of the hydro resources have been harnessed so far. In addition, the high-energy demand inside and outside the country will increase the construction activities in the years to come. All types of development activities are interdisciplinary and slope instability in general will be a common challenge in many countries around the world.

Fig. 1.1 Highway slope failure at Krishnabhir, Tribhuwan highway Nepal (photo from 2003)

Fig. 1.1 illustrates one of the biggest landslides caused by the yearly monsoon in Nepal. This is a highway slope failure, which was potentially active for several years. The highway is the only entry point to Kathmandu, the capital city of Nepal. Though the slope seems relatively stable in the dry period, it suffers substantial stability problems in the monsoons. When the first slide

occurred, it created a shortage of daily supplies to the capital due to the traffic stoppage for several weeks. As discussed above, the monsoon rain is one of the triggering mechanisms of slope failures in several mountainous countries in this region. Due to rainwater, the erosion potential is increased and weathering processes are activated. Moreover, water infiltrates the soil and groundwater table rises in the slope. About the causes of such landslides, Edgers and Nadim (2004) say, "Development of positive pore pressure, and in some cases the reduction in suction, may be sufficient to cause a landslide."

Generally, hydropower intallations are located at the base of hill slopes. Fig. 1.2 shows such installations made for the Khimti hydropower plant (KHP) in Nepal, where the structures were built to divert the river flow into the tunnel for power generation. In such environment, there is always a potential risk of landslides, defined as the product of probability of slope failure and the consequences, during the monsoon, and particularly during the events of earthquakes. However, periodical monitoring, risk evaluation and routine maintenance works may lower the associated risk of large-scale slope failures (Aryal & Sandven 2005, Aryal et al. 2004). If the slope fails within the operation period, the economic consequences will be enormous.

Fig. 1.2 Important structures built at the base of the slope (KHP) (Aryal & Sandven 2005)

The major hydropower plants in Nepal, like Kali Gandakai (144 MW), Khimti (60 MW) and Bhotekoshi (36 MW) may be prone to risk of slope failure in the future. Post-construction damage of the important hydropower structures due to slope failure may cause several times higher economic loss than the loss caused by such failures during the construction period. Detailed analytical studies in the design stage are thus very important to alleviate the adverse factors that may cause slope instability in the long-term basis.

The scope of this study: "Slope stability evaluations by LE and FE methods" is expected to address such instability problems. The analytical solutions to the instability problems, including the effects of groundwater variations and earthquake effects, are expected to contribute to improve the knowledge of these processes, both with respect to the benefit of engineering in Nepal and the international society.

The aim of the study has been to fulfill three main objectives. The first objective has been to compare the most common limit equilibrium (LE) methods. Moreover, the most accurate LE methods have been selected for comparison with the more advanced finite element (FE) method. The second objective has been to evaluate the stability conditions of the slopes situated at the Middle Marsyangdi Hydroelectric Project as a case study. The third objective has been to determine the appropriate shear strength parameters for stability analysis at the site. Within this framework, the study has focused on the following topics:

- Comparison and evaluation of slope stability (LE and FE) methods,
- Evaluation to the long-term stability condition of natural slopes, and
- Investigations of shear strength and other relevant parameters for stability analyses.

Available approaches are utilised to achieve the outlined objectives in this study. The first two objectives are fulfilled using following three computer based geotechnical software codes:

- SLOPE/W, based on LE principles,
- SLIDE, also based on LE principles, and
- PLAXIS, based on FE principles.

Among the most common LE based methods, which are incorporated in both SLOPE/W and SLIDE software, Bishop and Janbu's simplified methods, Janbu's generalised method and the Morgenstern-Price method are considered for comparison purposes. The factor of safety (FOS) from these methods is further compared with the FOS obtained by the FEM code PLAXIS. The comparisons are based on a simplified slope analysed for various load combinations. Moreover, the long term-stability of natural slopes has been evaluated under the second objective with the most adverse load combinations. The stability evaluations of real slopes are again based on the selected LE methods from the simplified slope analyses and FE software PLAXIS. The third objective is achieved from the field and laboratory investigations. Several tests were conducted to determine the relevant input parameters. Finally, the shear strength parameters were investigated using advanced triaxial tests.

1.3 Brief introduction of the case study

The case study with the relevant slopes was taken from the Middle Marsyangdi Hydroelectric Project (MMHEP) in Nepal. The project, whose location map is given in Fig. 1.3, is now in the construction stage and aims to generate 470 GWh annual energy after 2007 (CES 2005). Besides

MMHEP, there are two other projects shown in Fig. 1.3, the Lower Marsyangdi Hydropower Project (LMEHP), which is in the operation stage, and the Upper Marsyangdi Hydropower Project (UMHEP), which is currently in the planning stage. The water resources of Marsyangdi River are glaciers from the Annapurna Himalayan range along the China (Tibet) boarder, as shown in Fig. 1.3.

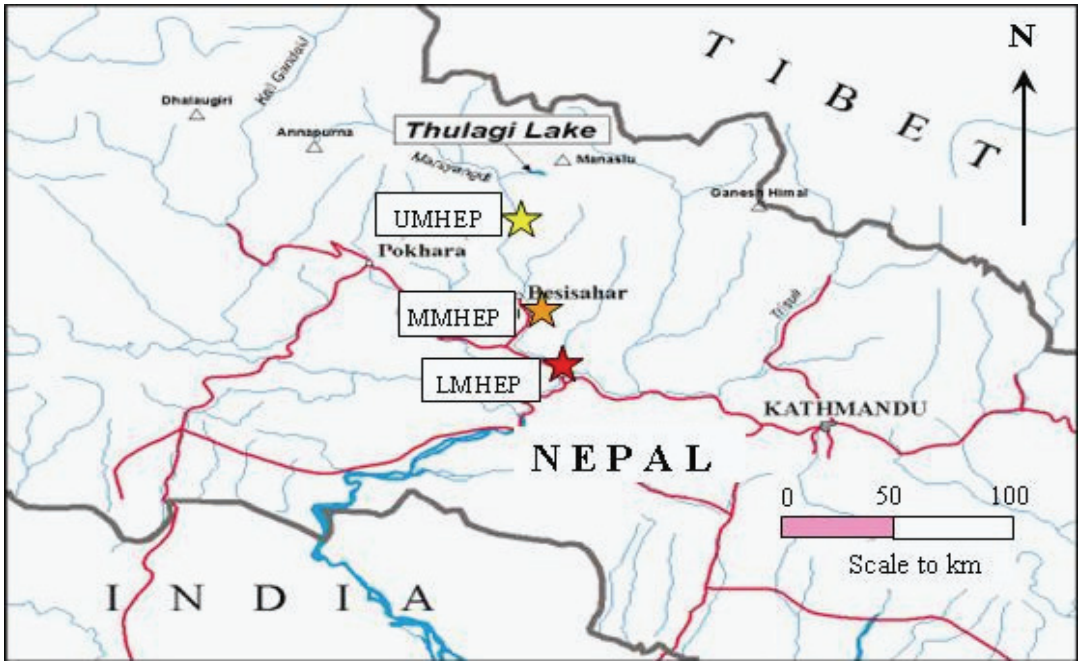

Fig. 1.3 Location map of MMHEP in Nepal (Nepal & Olsson 2001)

Two slopes as the case study from the MMHEP project were considered for detailed stability analysis. One was from the dam site left bank and another from the powerhouse area. Details of the case study slopes and a corresponding site description are given in Chapters 4 and 6. By linking the background theoretical considerations of different stability calculation approaches to this local project in Nepal, the research work may contribute to the understanding of slope stability analysis as an integrated approach to the conditions representative to Nepal and other regions with similar geological and climatic conditions.

1.4 Presentation of the thesis

Presentation of this thesis has been organised in several Chapters and Appendices. A brief description is given here. Chapter 2 describes the literature review on stability analysis methods. The review focuses on the LE principles in FOS determination. Moreover, most of the LE methods are discussed with highlights on their fundamental differences and limitations in practical applications. Besides, a theoretical comparison of the LE methods has been presented. Finally, the chapter ends with introducing brief working principles of three computer software codes (SLOPE/W, SLIDE and PLAXIS) that are applied in the present study. Comparisons of the LE and FE methods have been given in Chapter 3, where a simplified and idealised slope has

been analysed by the given software. Three following conditions have been considered to compare the selective methods:

- dry slope,
- fully saturated slope, and
- the slope exposed to combinations of earthquakes and surcharge loads.

Finally, the respective FOS obtained from the LE and FE analyses has been compared.

Chapter 4 includes data collection for the case study slopes located in Nepal. A brief description of the case study has been given, together with relevant information. Details of the sampling for subsequent laboratory investigations are also presented. Furthermore, the climatic condition has been discussed, and 10 years of rainfall data are presented. Likewise, a brief coverage of seismic events around the project area and groundwater records from the site-specific slopes is included. The shear strength parameters determined by the previous laboratory investigations are presented as reference soil data. Finally, the chapter concludes with a review of previous stability analyses of the selected case study slopes.

Chapter 5 includes the relevant in situ and detailed laboratory investigations carried out to characterise the materials and identify shear strength parameters for slope stability analyses. A short description of laboratory test procedures used has been given for some of the tests. Results from index tests, permeability tests and compression tests are presented. Likewise, the results from mineralogical tests are summarised. This chapter, however, focuses on the results from numerous triaxial tests that were conducted in drained and undrained conditions, and the results are presented and discussed at the end of this chapter.

The stability analyses of the case study slopes have been presented in Chapter 6. Two slopes, one from the dam site and another from the powerhouse site have been analysed for various load conditions. Some of the critical load cases, including groundwater seepage analyses and earthquake conditions have been studied in closer details. This chapter hence provides both comparisons of the selected approaches and the stability conditions of the slopes in different loading conditions. The same methods and computer codes as used in Chapter 3 are used for stability analyses of the studied slopes.

Chapter 7 includes discussions and comments on the applied methods, specific stability conditions due to various loads and comparison of LE and FE methods. The discussion is also related back to the theoretical study in Chapter 2 and the highlights from the comparisons carried out in Chapter 3. Some discussions have been carried out on the shear strength parameters investigated in the laboratory and presented in Chapter 5. Similarly, the stability analyses results of the case study slopes are discussed, referring back to the findings presented in Chapter 6. Finally, the main findings on the slope stability evaluations from the study are summarized in Chapter 8, including recommendations for further study.

Chapter 2

Review of Stability Analysis Methods

2.1 Limit equilibrium principles

All limit equilibrium methods utilise the Mohr-Coulomb expression to determine the shear strength (τ_f) along the sliding surface. The shear stress at which a soil fails in shear is defined as the shear strength of the soil. According to Janbu (1973), a state of limit equilibrium exists when the mobilised shear stress (τ) is expressed as a fraction of the shear strength. Nash (1987) says, "At the moment of failure, the shear strength is fully mobilised along the failure surface when the critical state conditions are reached". The shear strength is usually expressed by the Mohr-Coulomb linear relationship, where the τ_f and τ are defined by:

Shear strength (available): $$\tau_f = c' + \sigma' \tan\phi' \text{ or } (a + \sigma')\tan\phi' \quad (2.1)$$

Shear stress (mobilised): $$\tau = \frac{\tau_f}{F} = \frac{c' + \sigma' \tan\phi'}{F} \quad (2.2)$$

where,

a, c′ and ϕ′ = attraction, cohesion and friction angle respectively in effective stress terms, and

F = factor of safety (FOS).

The available shear strength depends on the type of soil and the effective normal stress, whereas the mobilized shear stress depends on the external forces acting on the soil mass. This defines the FOS as a ratio of the τ_f to τ in a limit equilibrium analysis (Janbu 1954), as defined in Eq. (2.2).

However, the FOS can be defined in three ways: Limit equilibrium, force equilibrium and moment equilibrium (Abramson et al. 2002). These definitions are given in Fig. 2.1. As explained above, the first definition is based on the shear strength, which can be obtained in two ways: A total stress approach (s_u-analysis) and an effective stress approach (a-ϕ –analysis). The type of strength consideration depends on the soil type, the loading conditions and the time elapsed

after excavation. The total stress strength is used for short–term conditions in clayey soils, whereas the effective stress strength is used in long-term conditions in all kinds of soils, or any conditions where the pore pressure is known (Janbu 1973, Grande 1977). The second and third definitions are based on force equilibrium and movement equilibrium conditions for resisting and driving force and moment components respectively.

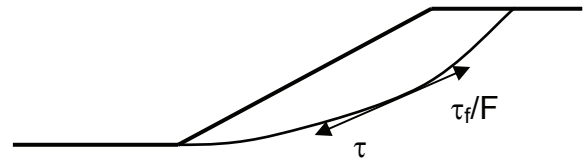

Limit equilibrium

Limit equilibrium:

$$F = \frac{s_u}{\tau} \qquad \text{(Total stress)}$$

$$F = \frac{c' + \sigma' \tan\phi'}{\tau} \qquad \text{(Effective stress)}$$

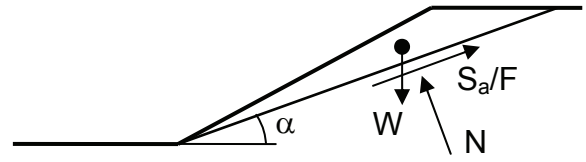

Force equilibrium

Force equilibrium:

$$F = \frac{\text{Sum of resisting forces}}{\text{Sum of driving forces}}$$

$$F = \frac{S_a}{W \sin\alpha} = \frac{\text{cL+Ntan}\phi}{\text{Wsin}\alpha}$$

where,

L = total length of the sliding plane

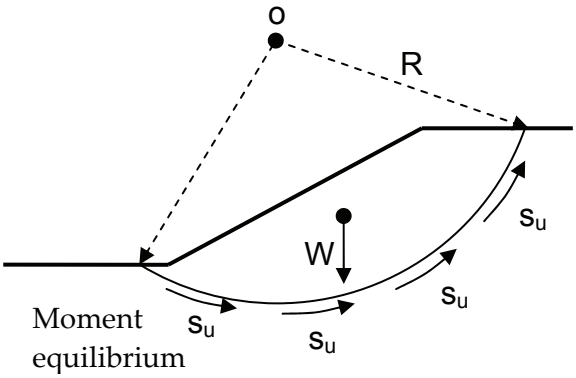

Moment equilibrium

Moment equilibrium:

$$F = \frac{\text{Sum of resisting moments}}{\text{Sum of driving moments}}$$

$$F = \frac{R\int_0^L s_u dl}{W.x}$$

Fig. 2.1 Various definitions of the factor of safety (FOS) (Abramson et al. 2002)

The last two definitions may sometimes be confusing while defining the terms, whether the force or moment components are contributing on resisting or driving sides. The reason can be explained with simple examples. The support force component along the sliding surface can be considered on the resisting side as a positive contribution, since it increases resistance capacity against the movement. At the same time, this component can also be considered on driving side as negative contribution, since it decreases the driving tendency. Similarly, the moments from the self weight of slices located at the toe are sometimes resisting and thus, considered either on the resisting side as positive contribution or on the driving side as negative contribution. These two different considerations result in different FOS. But this is not a case in the first definition.

2.2 Limit equilibrium methods

Several limit equilibrium (LE) methods have been developed for slope stability analyses. Fellenius (1936) introduced the first method, referred to as the Ordinary or the Swedish method, for a circular slip surface. Bishop (1955) advanced the first method introducing a new relationship for the base normal force. The equation for the FOS hence became non-linear. At the same time, Janbu (1954a) developed a simplified method for non-circular failure surfaces, dividing a potential sliding mass into several vertical slices. The generalised procedure of slices (GPS) was developed at the same time as a further development of the simplified method (Janbu 1973). Later, Morgenstern-Price (1965), Spencer (1967), Sarma (1973) and several others made further contributions with different assumptions for the interslice forces. A procedure of General limit equilibrium (GLE) was developed by Chugh (1986) as an extension of the Spencer and Morgenstern-Price methods, satisfying both moment and force equilibrium conditions (Krahn 2004, Abramson et al. 2002). These developments are reviewed in the following section, which aims to find out the key differences in the various approaches for FOS determination.

All LE methods are based on certain assumptions for the interslice normal (E) and shear (T) forces, and the basic difference among the methods is how these forces are determined or assumed. In addition to this, the shape of the assumed slip surface and the equilibrium conditions for calculation of the FOS are among the others. A summary of selected LE methods and their assumptions are presented in Table 2.1.

Table 2.1 Summary of LE methods (Abramson et al. 2002, Nash 1987)

Methods	Circular	Non-cir.	∑M = 0	∑F = 0	Assumptions for T and E
Ordinary	√	-	√	-	Neglects both E and T
Bishop simplified	√	(*)	√	(**)	Considers E, but neglects T
Janbu simplified	(*)	√	-	√	Considers E, but neglects T
Janbu GPS	√	√	(***)	√	Considers both E and T, act at LoT
Lowe-Karafiath	-	√	-	√	Resultant inclines at, $\theta = \frac{1}{2}(\alpha + \beta)$
Corps of Engrs.	-	√	-	√	Resultant inclines at, $\theta = \frac{1}{2}(\alpha_1 + \alpha_2)$
Sarma	√	√	√	√	Interslice shear, $T = ch + E\tan\phi$
Spencer	√	(*)	√	√	Constant inclination, $T = \tan\theta\, E$
Morgenst.-Price	√	√	√	√	Defined by f(x), $T = f(x).\lambda.E$

(*) Can be used for both circular and non-circular failure surfaces,

(**) satisfies vertical force equilibrium for base normal force, and

(***) satisfies moment equilibrium for intermediate thin slices (Janbu 1957, Grande 1997)

The interslice forces depend on a number of factors, including stress-strain and deformation characteristics of the materials. Their evaluation, however, becomes complicated in the LE methods. Therefore, simplified assumptions are made in most methods either to neglect both or to one of them. Nevertheless, the most advanced methods consider these forces in the LE analyses. Some of the basic principles behind the methods are briefly described below.

2.2.1 The Ordinary method

The Ordinary method (OM) satisfies the moment equilibrium for a circular slip surface, but neglects both the interslice normal and shear forces. The advantage of this method is its simplicity in solving the FOS, since the equation does not require an iteration process. The FOS is based on moment equilibrium and computed by (Abramson et al. 2002, Nash 1987):

$$F_m = \frac{\sum(c'l + N'\tan\phi')}{\sum W \sin\alpha} \tag{2.3}$$

$$N' = (W\cos\alpha - ul) \tag{2.4}$$

Where,

u = pore pressure,

l = slice base length and

α = inclination of slip surface at the middle of slice

In summary, OM

- satisfies moment equilibrium condition,
- neglects the interslice normal and shear forces,
- gives the most conservative FOS, and
- is useful only for demonstrations.

The forces considered in OM are shown in the sketch.

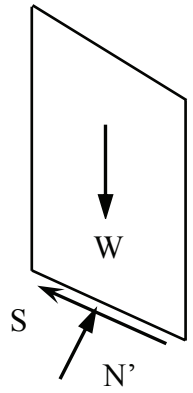

2.2.2 Bishop's methods

Bishop's simplified method (BSM) is very common in practice for circular shear surface (SS). This method considers the interslice normal forces but neglects the interslice shear forces (Abramson et al. 2002). It further satisfies vertical force equilibrium to determine the effective base normal force (N'), which is given by:

$$N' = \frac{1}{m_\alpha}\sum\left(W - \frac{c'l\sin\alpha}{F} - ul\cos\alpha\right) \tag{2.5}$$

where,

$$m_\alpha = \cos\alpha(1 + \tan\alpha \frac{\tan\phi'}{F}) \tag{2.6}$$

Since the BSM also assumes a circular failure surface, the same Eq. (2.3) is utilised to determine the FOS. However, computation requires an iterative procedure because of the nonlinear relationship as the FOS appears on both sides.

In summary, BSM

- satisfies moment equilibrium for FOS,
- satisfies vertical force equilibrium for N,
- considers interslice normal force,
- more common in practice, and
- applies mostly for circular shear surfaces.

The forces considered in BSM are shown in the sketch.

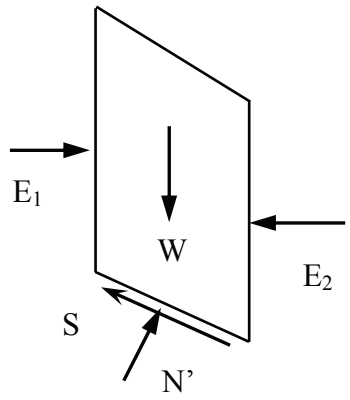

The Bishop rigorous method (BRM) considers the interslice shear forces (T) in addition to interslice normal forces (E). The method further assumes a unique distribution of their resultant forces and satisfies moment equilibrium of each slice. The interslice T and E forces, and hence the FOS are determined by an iteration procedure (Abramson et al. 2002).

2.2.3 Janbu's methods

The simplified method, generalised method (GPS) and direct method developed by Janbu (1954, 1968) are very common in stability analysis. The fundamental differences in these methods are briefly reviewed below.

2.2.3.1 Janbu's simplified method

Janbu's simplified method (JSM) is based on a composite SS (i.e. non-circular) and the FOS is determined by horizontal force equilibrium. As in BSM, the method considers interslice normal forces (E) but neglects the shear forces (T). The base normal force (N) is determined in the same way as in BSM and the FOS is computed by:

$$F_f = \frac{\sum\left(c'l + (N - ul)\tan\phi'\right)\sec\alpha}{\sum W\tan\alpha + \sum\Delta E} \tag{2.7}$$

where,

$\sum\Delta E = E_2 - E_1$ = net interslice normal forces (zero if there is no horizontal force).

The derivations of the FOS based on both force and moment equilibrium is given in Appendix G. In stress terms originally presented by Janbu (1954), the Eq. (2.7) is written as:

$$F_o = \frac{\sum\left\{\frac{b\left(c' + (p-u)\tan\phi'\right)}{n_\alpha}\right\}}{\sum p.b\tan\alpha} \tag{2.8}$$

$$\mathrm{n}_\alpha = \cos^2\alpha\left(1 + \tan\alpha\frac{\tan\phi'}{F}\right) \tag{2.9}$$

where,

$p = W/b$ = total vertical stress and b = width of slice

In summary, JSM

- satisfies both force equilibriums,
- does not satisfy moment equilibrium,
- considers interslice normal forces, and
- is commonly used for composite shear surface.

The forces considered in JSM are indicated in the sketch.

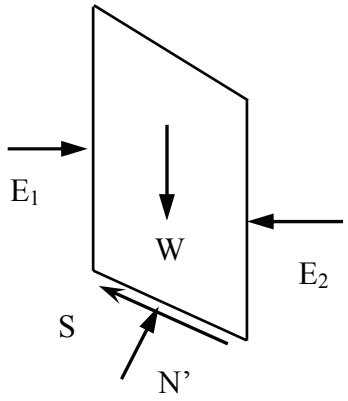

Janbu introduced a correction factor (f_o), in the original FOS (F_o), to accommodate the effects of the interslice shear forces. With this modification, Janbu's corrected method (JCM) gives higher FOS, as:

$$F_f = f_o.F_o \tag{2.10}$$

The correction factor depends on the depth to length ratio (d/L) of the failure surface. The FOS, with this correction factor, can increase by 5 -12%, giving the lower range in friction only soils, i.e. the soils without cohesion and the higher range for clayey soils (Abramson et al. 1996, 2002).

2.2.3.2 Janbu's generalised method

Janbu's generalised method (JGM) or Janbu's generalised procedure of slices (GPS) (Janbu 1973) considers both interslice forces and assumes a line of thrust to determine a relationship for interslice forces. As a result, the FOS becomes a complex function with both interslice forces (Nash 1987):

$$F_f = \frac{\sum\left[\left\{c'l + (N-ul)\tan\phi'\right\}\sec\alpha\right]}{\sum\left\{W - (T_2 - T_1)\right\}\tan\alpha + \sum(E_2 - E_1)} \tag{2.11}$$

Similarly, the total base normal force (N) becomes a function of the interslice shear forces (T) as:

$$N = \frac{1}{m_\alpha}\left\{W - (T_2 - T_1) - \frac{1}{F}(c'l - ul\tan\phi')\sin\alpha\right\} \quad (2.12)$$

This is the first method that satisfies both force and moment equilibrium. The moment equilibrium for the total sliding mass is explicitly satisfied by considering an infinitesimal slice width (dx) and taking moments about the mid point of the slice base (Janbu 1957, 1973). The infinitesimal slice width was introduced to avoid the confusion about the point of application of base normal force. This equilibrium condition in fact gives the relationship between the interslice forces (E and T) as:

$$T = \tan\alpha_t E - \frac{dE}{dx}h_t \quad (2.13)$$

where,

$tan\alpha_t$ = slope of the line of thrust, and

h_t = height from the mid point of the slice base to dE.

The interslice force relationship obtained in Eq. (2.13) is the same as Janbu first established, except for the interslice shear force direction, which is assumed here counter-clockwise for a slide occurring from left to right as shown in the sketch. The last term in Eq. (2.13) cannot be ignored because of the gradient of interslice normal force with respect to distance.

The line of thrust follows the centroid of the earth pressure (Janbu 1973, Nash 1987). However, for statically determinate solutions, the actual location is searched for by an iteration procedure until the total equilibrium is satisfied (Abramson et al. 2002). Since the overall force equilibrium is satisfied by the interslice forces, the moment equilibrium automatically fulfils for the sliding mass (Nash 1987, Grande 1997).

In summary, JGM (GPS)

- considers both interslice forces,
- assumes a line of thrust for interslice forces,
- satisfies both force and moment equilibriums,
- handles complex geometry and failure surfaces,
- is an advanced method among LE methods.

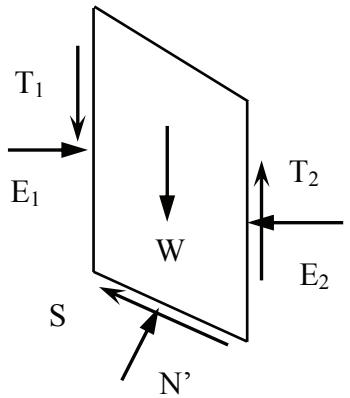

The forces considered are indicated in the sketch.

The derivations of the force and moment equilibriums are presented in Appendix G.

2.2.3.3 Janbu's direct method

Janbu's direct method (JDM) is based on dimensionless parameters and series of stability charts (Janbu 1954a). These charts provide a powerful tool to carry out slope stability analysis, also including various load conditions such as groundwater, surcharge and tension cracks. In addition to this, the method can be used for both total and effective stress analyses.

The FOS for cohesive and frictional soils can be computed by (Janbu, 1954a, 1996):

$$F = N_{cf}\frac{c}{p_d}, \qquad \lambda_{c\phi} = \frac{p_e}{c}\tan\phi \quad \text{and} \quad p_e = (1-r_u)p_d \tag{2.14}$$

where,

p_d = γH = total stress, p_e = effective stress,

N_{cf} = stability number, which depends on dimensionless factor ($\lambda_{c\phi}$), and

$r_u = u/\gamma z$ = pore pressure ratio.

As illustrated in Fig. 2.2, first the rotation centre (X_0, Y_0) for the critical circle is identified in JDM with respect to the toe of the slope. This centre, which is also a moment equilibrium point, is a function of the slope angle β and a dimensionless factor ($\lambda_{c\phi}$). The latter can be read directly from Janbu's stability charts. This method is simpler and the FOS can be computed for a circular SS geometry in a short time.

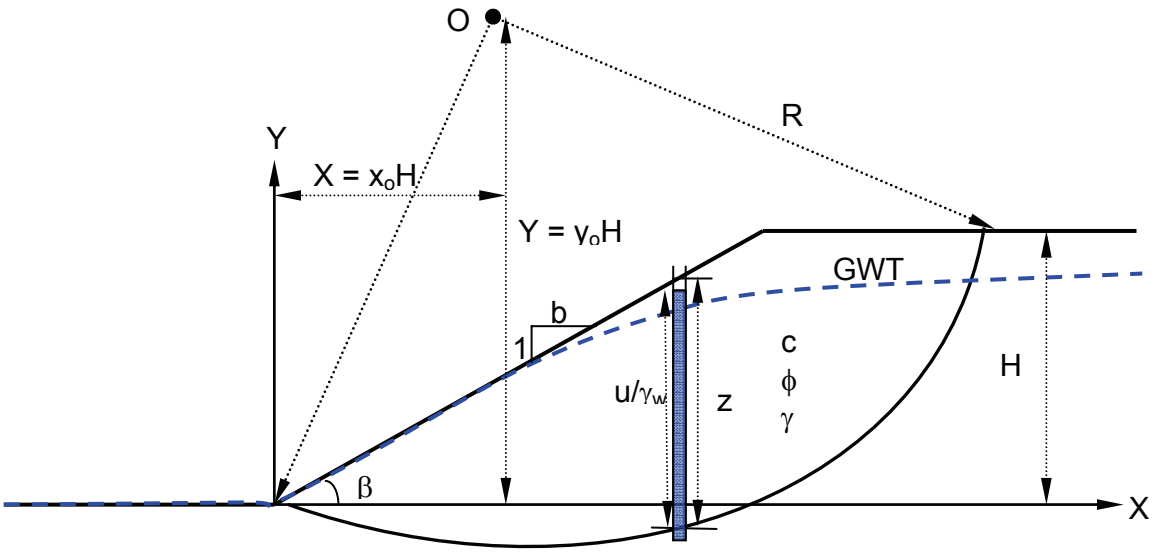

Fig. 2.2 Slope geometry illustrating Janbu's direct method

2.2.4 Lowe - Karafiath's method

Lowe - Karafiath's method (1960) satisfies only force equilibrium in FOS computation. Similar to other methods, L-KM assumes the interslice force inclination which is equal to the average of the slope surface inclination (β) and the slice base inclination (α), i.e. θ = ½(β + α), where θ is the inclination of the interslice resultant force. Thus, the interslice forces can be written as:

$$T = E \tan\theta \tag{2.15}$$

In summary, L-KM

- considers both interslice normal and shear forces,
- satisfies only force equilibrium , and
- assumes inclination for the resultant interslice force.

2.2.5 Corps of Engineers method

The Corps of Engineers (1970) method is similar to L-KM, except for the assumption of interslice force inclination. According to this method, the angle of the interslice resultant force can be assumed in two ways. First, it can be assumed parallel to the ground surface, i.e. θ =β, where β is the slope angle. Two, it can be equal to the average slope angle between the entry and exit points of the critical SS.

- In summary, CEM:
- considers both interslice normal and shear forces,
- satisfies only force equilibrium, and
- assumes inclinations in two ways.

2.2.6 Sarma method

Sarma (1973) developed a method for a non-vertical slice or for general blocks. This method satisfies both equilibrium conditions (Abramson et al. 2002). In addition, the interslice force relationship is assumed as a linear Mohr-Coulomb expression:

$$T = ch + E \tan\phi \tag{2.16}$$

where,
c, ϕ = shear strength parameters, and h = slice height.

The interslice forces are adjusted until the FOS for force and moment equilibrium is satisfied.

In summary, Sarma's approach:

- considers both interslice normal and shear forces,
- satisfies both moment and force equilibrium, and
- relates the interslice forces by a quasi-shear strength equation.

2.2.7 Morgenstern-Price method

The Morgenstern- Price method (M-PM) also satisfies both force and moment equilibriums and assumes the interslice force function. According to M-PM (1965), the interslice force inclination can vary with an arbitrary function (f(x)) as:

$$T = f(x).\lambda.E \tag{2.17}$$

where,

f(x) = interslice force function that varies continuously along the slip surface,

λ = scale factor of the assumed function.

The method suggests assuming any type of force function, for example half-sine, trapezoidal or user defined. The relationships for the base normal force (N) and interslice forces (E, T) are the same as given in JGM. For a given force function, the interslice forces are computed by iteration procedure until, F_f is equals to F_m in Eqs. (2.18) and (2.19) (Nash 1987). The derivations of the force and moment equilibriums FOS are presented in Appendix G.

$$F_f = \frac{\sum\left[\left\{c'l + (N - ul)\tan\phi'\right\}\sec\alpha\right]}{\sum\left\{W - (T_2 - T_1)\right\}\tan\alpha + \sum(E_2 - E_1)} \tag{2.18}$$

$$F_m = \frac{\sum(c'l + (N - ul)\tan\phi')}{\sum W\sin\alpha} \tag{2.19}$$

In summary, M-PM

- considers both interslice forces,
- assumes a interslice force function, f(x),
- allows selection for interslice force function,
- computes FOS for both force and moment equilibrium.

The forces considered are shown in the sketch.

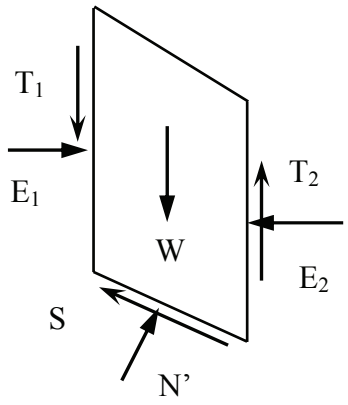

2.2.8 Spencer's method

Spencer's method (SM) is the same as M-PM except the assumption made for interslice forces. A constant inclination is assumed for interslice forces and the FOS is computed for both equilibriums (Spencer 1967). According to this method, the interslice shear force is related to:

$$T = E\tan\theta \tag{2.20}$$

In summary, SM

- considers both interslice forces,
- assumes a constant interslice force function, and
- satisfies both moment and force equilibrium, and
- computes FOS for force and moment equilibrium.

The forces considered are shown in the margin sketch.

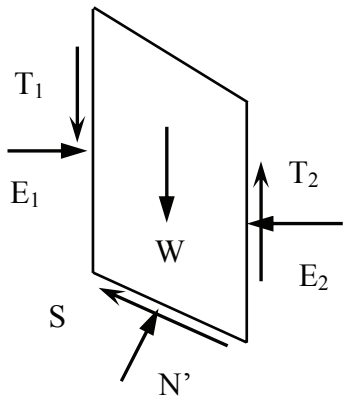

2.2.9 General limit equilibrium procedure

The general limit equilibrium (GLE) procedure incorporates all the assumptions and development made by the latest LE methods. In fact, this is an extension of Spencer and Morgenstern-Price methods where, the interslice slope, tanθ = λ. f(x) is assigned to determine the interslice forces (Krahn 2004, Abramson et al. 2002). In this way, the GLE procedure is good to compare the most common methods in a FOS versus λ diagram as shown in Fig. 2.3. The most likely inclinations of force equilibrium FOS (F_f) and moment equilibrium FOS (F_m) has been indicated particularly for circular SS analysis. The plane SS analysis may have revered position of F_f and F_m (Krahn 2004). However, more discussion on this matter is presented in Chapter 7.

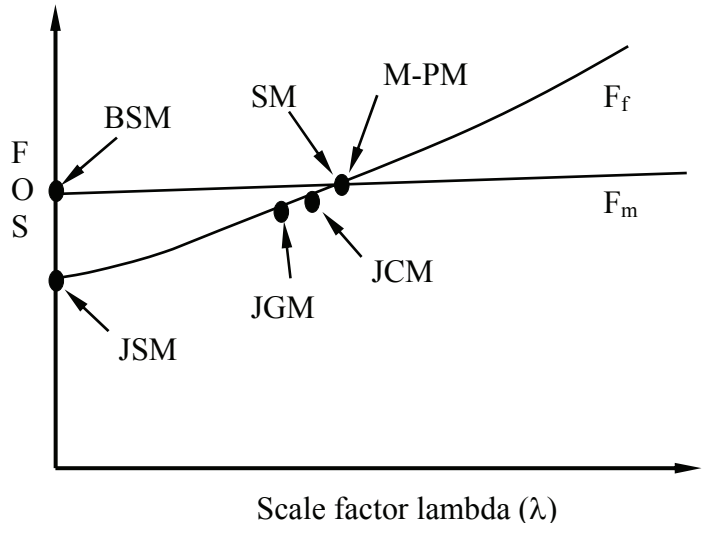

Fig. 2.3 Presentation of the most common methods (Fredlund and Krahn 1977)

When λ = 0, the FOS is obtained for BSM and JSM, as indicated in Fig. 2.3. Similarly, the intersection point gives the FOS for SM or M-PM. According to Fredlund and Krahn (1977), Janbu's corrected and generalised methods are close to the intersecting point (see Fig. 2.3). Thus, the GLE procedure has an advantage of making comparisons of FOS in the same diagram.

Stability analysis for both circular and composite SS is possible in this procedure (Fredlund et al. 1981, Chugh 1986). A variable interslice force function, as related to Eq. (2.17), defines the inclination of the interslice forces after subsequent iterations (Nash, 1987).

In summary, GLE procedure:

- considers both interslice normal and shear forces,
- satisfies both moment and force equilibriums,
- allows selection for interslice force function , and
- shows comparison of most common and advanced LE methods.

2.2.10 Summary of the LE methods

The OM is limited to hand calculations and demonstration purposes only, whereas BS and JSMs have been widely used for stability analyses in many years. These methods are common because the FOS in most cases can be calculated with adequate accuracy. However, these methods have limitations in satisfying both force and moment equilibrium. Abramson et al. (2002) recommend BSM to use only for the circular shear surface analysis. Similarly, JSM is more flexible in evaluating the FOS for non-circular surfaces. The main advantage over JGM is that it can effectively handle both irregular slopes and failure surfaces. Moment equilibrium for slices gives the complete solution for force equilibrium FOS, which is close to the FOS from M-P method.

For circular SS, BSM always gives higher FOS than JSM and falls within ± 5% of the FOS obtained from the more rigorous methods. However, the FOS can differ by ± 15% as compared with the results calculated by Spencer and Morgenstern-Price methods (Abramson et al. 2002).

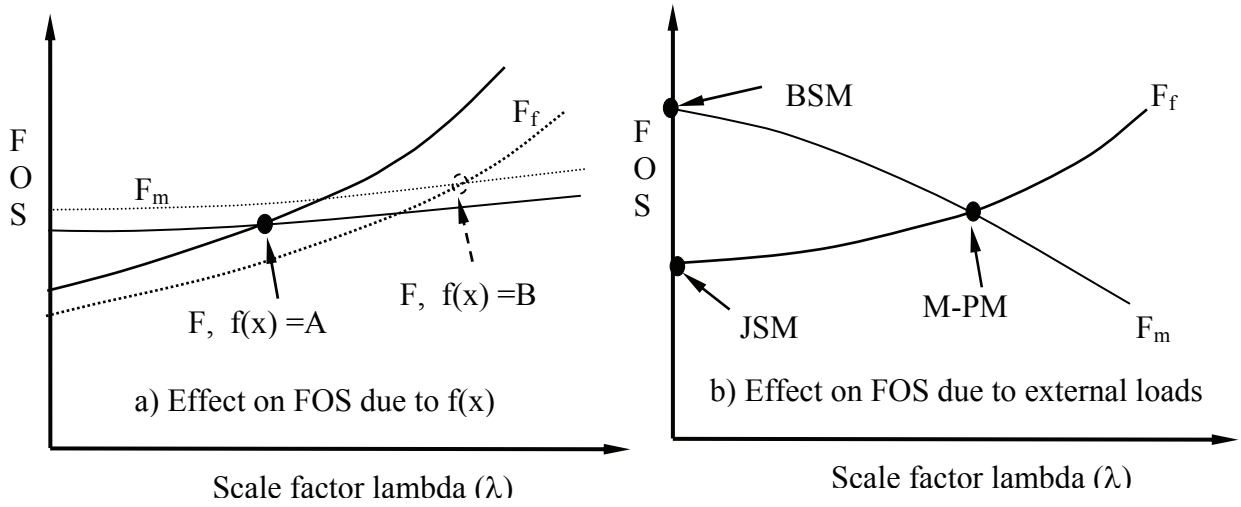

Fig. 2.4 Effects on FOS due to a) f(x) and b) external loads (SLOPE/W 2002)

Fig. 2.4 shows the possible variation in FOS due to f(x) and application of point loads or anchor forces (SLOPE/W 2002). The FOS from the force equilibrium is seen to be more sensitive to f(x) than from the moment equilibrium (see Fig. 2.4a). This is the case probably for circular SS. However, an investigation carried out by Fredlund and Krahn (1977) shows that the FOS is insensitive to the choice of f(x). In the case of point loads or anchors, the moment equilibrium FOS has considerable shifting towards lower FOS (see Fig. 2.4b). This shows that the FOS, from moment equilibrium, is more sensitive to the application of external forces. Due to the point loads or anchor forces, the interslice shear force is increased. This further reduces the base normal force (see Eq. (2.12)) and consequently the shear strength is reduced. The effects of the interslice force function and applied external forces on FOS in circular SS analysis are summarised and presented in Table 2.2.

Table 2.2 Sensitivity of FOS in circular SS analysis (SLOPE/W 2002)

Parameter	Force equilibrium FOS	Moment equilibrium FOS
Scale factor (λ)	More sensitive (FOS vs λ plot shows steeper slope, see Fig. 2.3)	Insensitive, (relatively flat slope is found, referring to Fig. 2.3)
Interslice force function (f(x))	Significantly affected as the plot shows considerable shifting (referring to Fig. 2.4a)	Miner effect, not much shifting is found (referring to Fig. 2.4a)
Point load or anchor force (Q)	The FOS gradient is found almost unchanged as in Fig. 2.4b	Found very sensitive and largely affected (referring to Fig. 2.4b)

2.3 Software used for stability analysis

Slope stability analyses today can be performed by using various computer based geotechnical software. Software utilizing LE formulations has been used for many years. Similarly, finite element (FE) software, based on constitutive laws and appropriate soil models, has drawn growing interest both of researchers and of professionals. Today, both LE and FE based software are commonly used in geotechnical computations. A brief introduction and working principles of the software that are used in this study is briefly introduced in the following sections.

2.3.1 SLOPE/W software

SLOPE/W, developed by GEO-SLOPE International Canada, is used for slope stability analysis. This software is based on the theories and principles of the LE methods discussed in the previous sections. In this study, SLOPE/W has been applied separately and together with

SEEP/W, other software program, which computes the pore pressure distributions, based on finite elements mesh and groundwater seepage analyses. Finally, the pore pressure distributions were coupled with slope stability analysis and FOS was determined. The software SLOPE/W computes FOS for various shear surfaces, for example circular, non-circular and user-defined surfaces (SLOPE/W 2002, Krahn 2004). However, only the circular SS is automatically searched.

2.3.1.1 Computation of FOS

A simple model presented in Chapter 3 and the case study from MMHEP given in Chapter 6 were analysed to find the critical SS and minimum FOS using different search options. The selected search options (grid and radius, entry and exit and auto-locate) were used in the study. The procedure described here is related to the analyses carried out in Chapters 3 and 6.

The *Grid and radius* option was selected to define the rotation centres and tangent lines as shown in Fig. 2.5. The circular CSS was searched among the number of trial surfaces within the tangent lines. Similarly, moment equilibrium was satisfied at a point within the grid, which was also the rotation centre of the CSS. Further refinements in grid and tangent lines improved the accuracy in finding the minimum FOS.

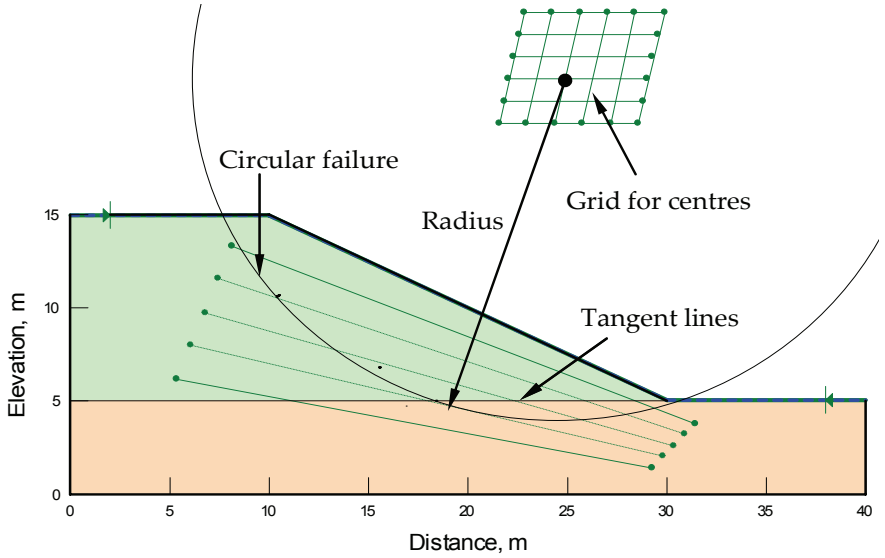

Fig. 2.5 Grid and radius option used to search for circular CSS

The *Entry and exit* option was applied on the surface of the model as indicated in Fig. 2.6. The software searched for the circular CSS among the number of trial surfaces within the given entry and exit ranges. The FOS is indicated at the axis of rotation, around which, the moment equilibrium is satisfied. Unlikely in the previous option, the centre of the circle and the moment equilibrium point are not the same in this option (see Fig. 2.6).

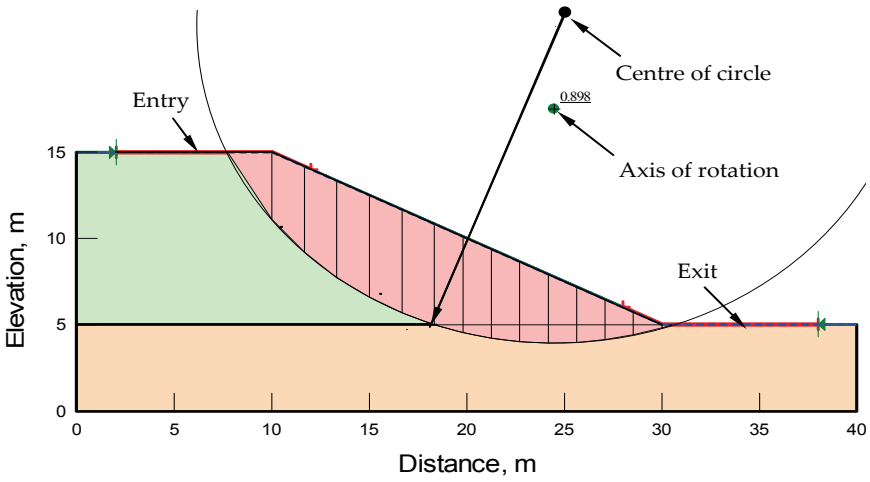

Fig. 2.6 Entry and exit option used to search for circular CSS

The stability analysis methods satisfying only moment equilibrium may be affected by manual selected rotation point (Krahn 2004). In such case, it either should be specified close to the centre of the possible CSS or should be left to locate automatically. However, FOS is insensitive with the rotation point for the methods that satisfy both moment and force equilibriums.

The *Auto-locate option* was selected to check the position of CSS and the FOS computed by the above two options. Moreover, this option is the combination of entry and exit, and optimisation, which results in slightly non-circular CSS. All three options, which were refined until a constant FOS was found, produced the same FOS for the CSS without optimisation in this study.

2.3.1.2 Shear surface optimisation

The CSS searched by GLE procedure for M-PM can be optimised and slightly lower FOS is found. After finding the CSS by one of the first two options above, the optimisation was carried out by the auto-locate CSS option. Accordingly, the software divides the CSS into number of line segments and the ends of the segments are moved towards the lower FOS resulting in slightly non-circular CSS, see Fig. 3.15 in Chapter 3.

2.3.1.3 Comparison of LE methods

The LE methods in SLOPE/W can be compared in two ways. The first is based on the CSS searched by each method and the corresponding FOS; the other is based on the CSS searched by GLE procedure and the corresponding FOS. The first comparison can be done directly by looking into the "minimum FOS" for the selected methods. This appears immediately after completion of the computation. The second comparison can either be done by the λ versus FOS plot or by the FOS found under the "slip surface with force data available" (optimised or non-optimised FOS). The comparisons of LE methods have been carried out in Chapters 3, 6 and 7.

2.3.2 The SLIDE software

SLIDE software, developed by Rocscience Inc Toronto Canada, is also used for slope stability analysis for soil and rock slopes. The software is also 2D-LE based computer program, which can be applied to evaluate the stability for circular or non-circular failure surfaces (SLIDE 2003). In fact, SLIDE is found similar to the SLOPE/W though there are few additional features, for example groundwater analysis and back analysis for support forces. In addition, JCM has also been included in the software.

Modelling in SLIDE for the study was possible for external loading, groundwater and forces, like surcharge and from pseudo-static earthquakes. The circular CSS was located automatically and the corresponding FOS was computed by the software in the similar way as in SLOPE/W. The idealised slope presented in Chapter 3 and the case studies presented in Chapter 6 were analysed by SLIDE software. The groundwater module was used to simulate and compute groundwater analysis based on finite element mesh, and the pore pressure distributions from the seepage analysis were used for the stability analysis. The analytical results are compared with SLOPE/W and PLAXIS in Chapters 3, 6 and 7.

2.3.3 The PLAXIS software

PLAXIS is a finite element code for soil and rock analyses (PLAXIS 2004), developed by PLAXIS BV in cooperation with several universities including DUT in the Netherlands and NTNU in Norway. The computer program is applicable to many geotechnical problems, including stability analyses and steady-state groundwater flow calculations. This software contains several FE models and four main sub-routines. These routines are inputs, calculations, outputs and curve plots. The FOS versus displacement is plotted from the curve plots sub-routine.

The slope models analysed in Chapters 3 and 6 were created by the input sub-routine. Material properties including shear strength parameters were defined for each soil layer. A plain strain model of 15 noded triangular elements was used to generate the finite element mesh. Similarly, pore pressure distributions were generated based on phreatic level with and without corrections and the steady-state groundwater calculation. Moreover, a Mohr-Coulomb material model was selected for the stability analyses.

The selected M-C model is based on the elastic-perfectly plastic theory of soil mechanics. Accordingly, both elastic parameters (E, ν) and plastic parameters (c′, ϕ′, Ψ) are utilised in the model. Similarly, in addition to the yield function (*f*), the model has incorporated plastic potential function (*g*), where the dilatancy angle (Ψ) is associated with the plastic behaviour of soils. The formulation of the M-C model consists of six yield functions and six plastic functions. One of each function is given below for demonstration purposes (PLAXIS 2004) only:

$$f_1 = \frac{1}{2}(\sigma'_2 - \sigma'_3) + \frac{1}{2}(\sigma'_2 + \sigma'_3)\sin\phi - c\cos\phi \le 0 \qquad (2.21)$$

$$g_1 = \frac{1}{2}(\sigma'_2 - \sigma'_3) + \frac{1}{2}(\sigma'_2 + \sigma'_3)\sin\psi \quad (2.22)$$

The terms are defined under the list of symbols in the beginning of the thesis.

2.3.3.1 Computation of FOS

FOS was computed by using the 'c-ϕ reduction' procedure. According to PLAXIS (2004), this approach involves in successively reducing the soil strength parameters c′ and tanϕ' until the failure occurs. The strength parameters are automatically reduced until the final calculation step results in a fully developed failure mechanism. Further, Nordal and Glaamen (2004) say, "By lowering the strength incrementally, a soil body is identified to fail after a certain strength reduction". In this way, PLAXIS computes the FOS as the ratio of the available shear strength to the strength at failure by summing up the incremental multiplier (M_{sf}) as defined by:

$$FOS = \frac{available\ shear\ strength}{shear\ strength\ at\ failure} = value\ of\ \ \sum M_{sf}\ \ at\ failure \quad (2.23)$$

2.3.3.2 Pseudo-static analysis

The pseudo-static analysis was carried out in PLAXIS by introducing the earthquake forces in terms of the acceleration coefficient (α). In the general settings of the input program, full value of gravity (g) was used, and the selected value of α was applied as the multiplier (ΣMaccel) in the calculation routine. The gravity controls the total magnitude of the acceleration applied in the calculation phase. The pseudo-static forces can only be applied if the weight of the material, ΣM-weight = 1 is active in the model. Moreover, application of an acceleration component in a particular direction results in a pseudo-static force in the opposite direction. The application of α with negative sign was found resulting in the critical direction in the slope. Computation for the FOS was then followed by the 'c-ϕ reduction' procedure as explained above.

2.3.3.3 Dynamic analysis

The case slopes in Chapter 6 were studied for the dynamic response for the selected horizontal acceleration. The source of earthquake loading was created along the base of the model resulting to upwards propagating shear waves. Accordingly, the dynamic source was created in terms of the prescribed horizontal displacement at the base of the model aiming to study the response generated by the soil mass. The problem was simulated using a plane strain model with the standard material damping used in PLAXIS.

- **Dynamic loading**

The basic equation for the time–dependent movement under the influence of a dynamic load is given by (PLAXIS 2004, Kramer 1994):

$$F = M\ddot{u} + C\dot{u} + Ku \quad (2.24)$$

where,

F = dynamic load,

M = inertia matrix (or mass of soil body),

C = damping matrix (or damping coefficient) and

K = stiffness matrix (or stiffness as spring constant).

The displacement (u), the velocity (ů) and the acceleration (ü) are time dependent variables. The mass of the materials (soil + water + dead weight) is included in the inertia matrix, whereas the damping matrix represents the material damping, which causes dissipation of energy due to the friction, plasticity and viscosity of the soil. The last term (F = Ku) corresponds to the static deformation. In FE elastic models, damping is thus formulated under C as a function of inertia and stiffness matrices related to the Rayleigh coefficients, α and β as follows (PLAXIS, 2004):

$$C = \alpha M + \beta K \tag{2.25}$$

The low-frequency vibrations are generally damped in inertia dominant structures, which mean higher α–value. However, high frequency vibrations are damped in stiffness dominant structures; this means higher β–value. These α and β coefficients are used in PLAXIS for plane strain elastic models. However, the standard setting in PLAXIS (α = β = 0) are used in the dynamic analysis in Chapter 6, though the frequency damping can be expected in real case.

- **Determination of α and β coefficients**

According to the resonance column theory, the resonance (natural) frequency can be determined based on the shear wave velocity (Nordal and Kramer 2003). For the purpose, the following relationships are used to compute the Rayleigh coefficients, α and β:

$$\omega_n = n\pi \frac{V_s}{2H} \tag{2.26}$$

$$\alpha + \beta\omega_n^2 = 2\omega_n\xi \tag{2.27}$$

where,

ω_n = dominating resonance (natural) frequency at low frequency range,

n = 1, 3, 5….

V_s = shear wave velocity, and

H = height of the soil column or layer.

ζ = damping ratio of damping coefficient (C) to critical damping coefficient ($C_c = 2\sqrt{(KM)}$).

The energy dissipates in soils by several mechanisms, including friction, hysteresis generation and plastic yielding. The value of ζ can either be obtained experimentally by means of the resonance column test ((Das 1995, Kramer 1994), or an alternative damping ratio value might be

chosen based on diagrams of damping versus cyclic shear strain. According to Vucetic and Dobry (1991), the damping ratio (ζ) is dependent on the plasticity index and the cyclic shear strain. For a selected or experimentally obtained value of ζ , the Rayleigh α and β coefficients are determined from Eq. (2.27) using two dominating frequencies at low frequency range.

- **P- and S-wave velocities**

Earthquake produces p and s-waves in the ground. Once the material parameters (E, ν and ρ) are entered into the input model, the wave velocities are automatically generated. The compression wave velocity (V_p) in the confined one-dimensional soil is a function of the oedometer stiffness (E_{oed}) and the mass density (ρ).Similarly, the shear wave velocity (V_s) is a function of the shear modulus (G_{ref}) and the mass density (ρ), as expressed by:

$$V_p = \sqrt{\frac{E_{oed}}{\rho}} \quad , \quad V_s = \sqrt{\frac{G_{ref}}{\rho}} \tag{2.28}$$

where,

$$E_{oed} = \frac{(1-\nu)E_{ref}}{(1+\nu)(1-2\nu)} \tag{2.29}$$

E_{ref} = Young's modulus at reference stress (σ_v = 100 kPa),

ν = Poisson's ratio, and

ρ= density of soil (= γ/g).

- **Rayleigh and Love waves**

The encounter of body waves, i.e. V_p and V_s, into a solid boundary generate a new type of waves called Rayleigh waves. These waves (defined as $V_R = \omega/k_R$, where k_R is the wave number) propagate on the ground surface and cause the largest disturbances in the earthquake events. Similarly, Love waves are generated in a soil layer overlain by a material with lower body waves. These waves are actually horizontal shear waves (SH-waves) that are trapped by multiple reflections within the superficial layer (Kramer, 1994).

- **Absorbent boundaries and analysis results**

Absorbent boundaries, as the vibration dampers, are applied to stop the rebound of stresses caused by wave propagations during the dynamic simulations, in addition to the standard fixities. The model geometry is made so wide that the boundaries could be applied sufficiently far away from the studied area.

The displacement and acceleration - time series and excess pore pressure are the main output results from the dynamic analyses. Similarly, excess pore pressures are generated when undrained soil is subjected to dynamic loading. These results are discussed in Chapter 6.

Chapter 3

Comparison of Analysis Methods

3.1 Idealised slope

A simple example with an idealised slope model is analysed aiming to compare the most common limit equilibrium (LE) methods. In addition, the study compares the most accurate LE method with finite element (FE) analyses for three different load conditions. Finally, some parameters are studied to understand possible differences in computations of the factor of safety (FOS).

3.1.1 Geometry and input parameters

Fig. 3.1 shows the idealised slope of 10 m height with an inclination of 1:2 (V:H). Two soil layers with different strength parameters are assumed. Furthermore, the same effective stress parameters are used in dry and wet conditions. Similarly, two unit weights of soils, one above the GWT (γ_d), the other below the GWT (γ), are considered. Moreover, the same permeability coefficient (k) is assumed in both layers for the seepage analysis. The parameters used in the study are shown in Fig. 3.1, with the complete set of input parameters given in Table 3.1.

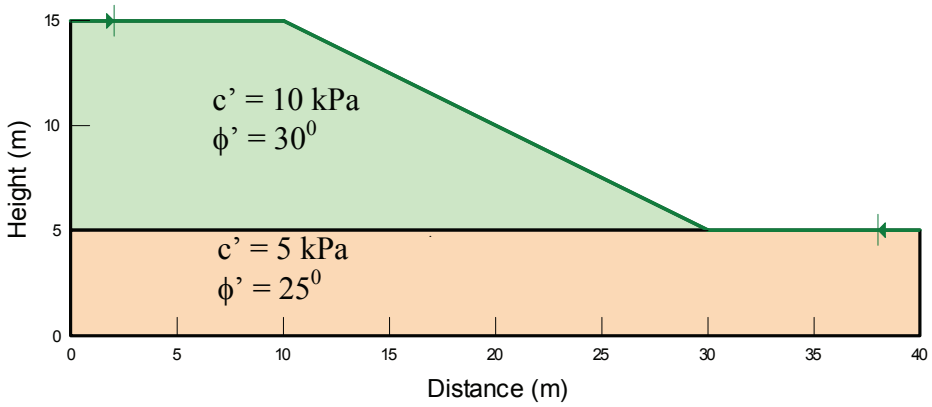

Fig. 3.1 Idealised slope geometry for "model" with two soil layers

Table 3.1 Input parameters for analyses

Soil layers	c′ (kPa)	ϕ′ (^{0})	ψ (^{0})	γ (kN/m^3)	γ_d (kN/m^3)	E_{ref} (kPa)	ν	k (m/s)
Upper	10	30	0	20	18	5000	0.3	1x 10^{-5}
Lower	5	25	0	20	18	5000	0.3	1x 10^{-5}

3.1.2 Load combination for analysis

Three different conditions; Dry slope, Wet slope and Dry slope with external loads are considered for the stability analyses. The load conditions analysed are defined as:

- Case 1: Completely dry slope, i.e. no GWT inside the model,
- Case 2a: Completely saturated slope, i.e. GWT on the surface (hydrostatic pore pressure),
- Case 2b: Completely saturated slope (pore pressure from seepage analysis), and
- Case 3: Dry slope with external forces, i.e. q = 50 kPa and earthquake coefficient, α_h = 0.25.

3.1.3 Selected methods for analysis

Stability chart methods, LE and FE based software are selected for analyses and comparison of the FOS. The basic theory and different assumptions made in the LE methods are given in Chapter 2. The selected methods and software are:

- LE methods: Stability charts from JDM, two software SLOPE/W and SLIDE, and the selected methods are BSM, JSM , JGM and M-PM or GLE.
- FE method: Software PLAXIS.

3.2 Stability analyses and results

3.2.1 Application of stability charts

Among the direct methods, which are based on the slope stability charts developed by several authors, Janbu's direct method was selected in this study. This method is well known for stability analysis. The method was selected to demonstrate its simplicity and user-friendliness. Moreover, it was also aimed to compare the results with other LE based methods for dry and saturated slope conditions. The analyses results are presented in Table 3.2. The method has been reviewed in Section 2.2.3.3 in Chapter 2, where the appropriate symbols are defined.

Table 3.2 Analyses results by JDM

Load Cases	$\lambda_{c\phi}$	$N_{\chi\phi}$	p_e (kPa)	p_d (kPa)	FOS
1: Dry slope	13	40	180	180	1.778
2a: Wet slope	7	25	100	200	1.000

The factors $\lambda_{c\phi}$ and $N_{c\phi}$ were obtained from the stability charts for the effective stress (c-ϕ) analysis. The circular CSS passes through both layers, and hence the distribution was assumed as 60% in the upper layer and 40% in the lower layer, based on the CSS located by M-PM in SLOPE/W (see Fig. 3.2). Accordingly, the factor $\lambda_{c\phi}$ was computed by weighted average:

$$\lambda_{c\phi} = \frac{p_e}{c}\tan\phi = \frac{p_e}{l}\left(l_1\frac{\tan\phi_1}{c_1} + l_2\frac{\tan\phi_2}{c_2}\right) \qquad (3.1)$$

The averaging of $\lambda_{c\phi}$ was used to make computation practically possible. However, the weighted average of the product of the effective normal stress (p_e) and $tan\phi$ would have been theoretically more correct. The FOS was compared with M-PM (dry slope: FOS = 1.737) and found moderate variation, which might in fact have resulted from the parameter readings from the charts. In addition, the assumption made for the failure surface in the two-soil layer slope may also have minor differences. However, the difference is minimal. The advantage over JGM is that the FOS can be computed more easily by hand calculations to check the stability in simple conditions.

3.2.2 Application of software programs

3.2.2.1 Load Case 1: Dry slope

- **SLOPE/W software**

The stability of the dry slope was first analysed in SLOPE/W. The minimum FOS and critical SS searched by entry and exit option (refer Section 2.3.1.1 in Chapter 2) are given in Fig. 3.2.

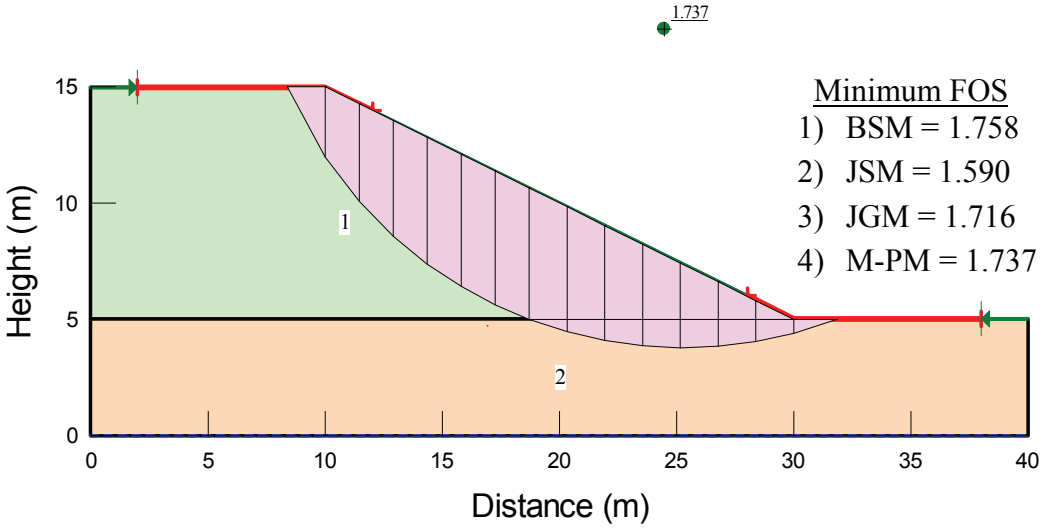

Fig. 3.2 CSS by M-PM and FOS from SLOPE/W for Case 1

The CSS was searched from thousands of possible SS by defining the input of 15 slices, 1500 iterations, and 15 increments for entry, 10 increments for exit and 5 increments for radius. These parameters are consecutively chosen until the further increments do not change the FOS.

Similarly, a Mohr-Coulomb soil model was chosen, without the feature of tension cracks. A half-sine function was selected to compute the interslice forces with tolerance error of 1%. Moreover, the selection of a half-sine function was based on the assumption that the interslice shear forces could be at maximum in the middle of the CSS and zero at the entry and exit points.

SLOPE/W computes the FOS in two ways. In the first approach, the rigorous GLE procedure identifies the CSS, whereas the rest of the methods compute the FOS based on the same CSS. In this way, the accuracy of the methods can be compared. In the second approach, each method identifies its own CSS and computes the corresponding FOS. In the latter approach (used in this study), SLOPE/W computes lower FOS for some methods, and thus the FOS is termed as "minimum" FOS.

- **SLIDE software**

As in SLOPE/W, the analysis was carried out in SLIDE for the same input parameters and model geometry. The results from the analyses are presented in Fig. 3.3.

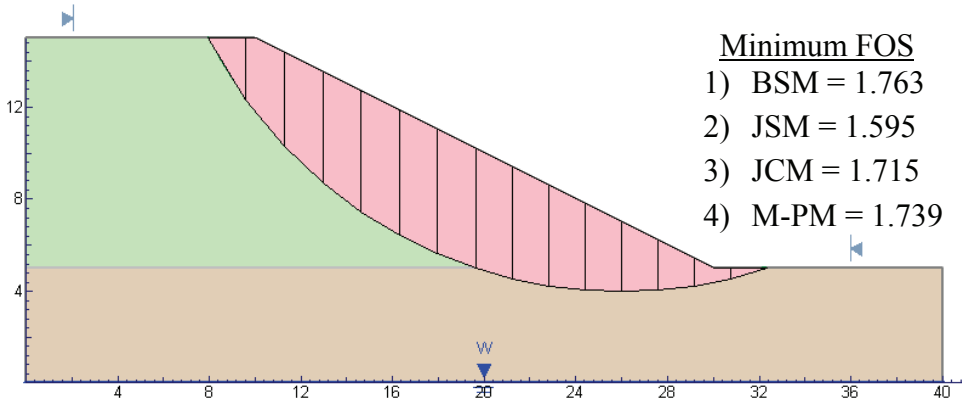

Fig. 3.3 CSS by M-PM and FOS from SLIDE for Case 1

In SLIDE, the CSS was selected from the auto-refined search option by defining as similar inputs as before in SLOPE/W. The input parameters were increased until further increments had no change in the FOS. In this way, the CSS and the minimum FOS were obtained.

The FOS from SLIDE was found very similar to SLOPE/W. In addition, the FOS from JCM in SLIDE and JGM in SLOPE/W was found to be the same. Moreover, the FOS from JGM was found only 1% lower than that from M-PM for the CSS identified by each method.

- **PLAXIS software**

The analysis also included use of PLAXIS with the same Mohr-Coulomb soil model and strength parameters as given in Table 3.1. A plain strain model was defined by using 15 noded elements and a well-refined mesh of about 3000 elements with 450 mm average size, no tension cracks and 1% tolerance. Further mesh refinement had no change in FOS. The FE based software

PLAXIS computes FOS by the c-ϕ reduction procedure, a detailed description of which can be found in Chapter 2. The CSS located by PLAXIS and the corresponding FOS are given in Fig. 3.4.

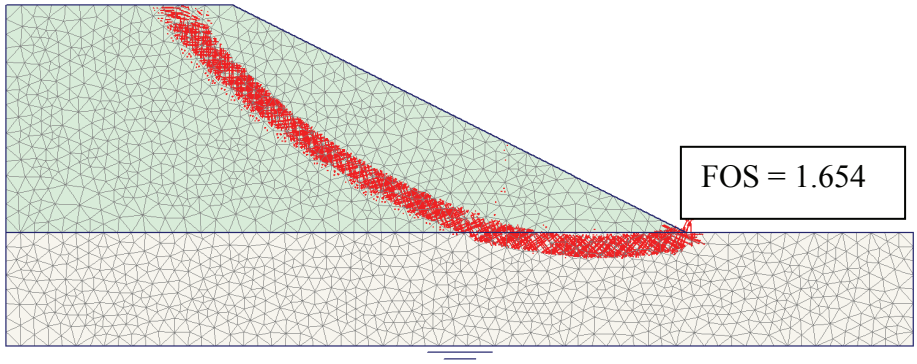

Fig. 3.4 CSS and FOS computed from PLAXIS for Case 1

PLAXIS identifies the CSS based on the strain localisation in the slope. The incremental strains are excessively concentrated inside the soil body (see Fig. 3.4) from which a failure may possibly initiate. Compared to the FOS obtained from PLAXIS, the LE method (M-PM) overestimates the FOS by 5% for dry slope conditions in this idealised slope analysis.

3.2.2.2 Load Case 2: Wet slope

The rise in GWT up to the surface and the effect on FOS was studied in the similar way as for the dry slope. In this case, the pore pressures were applied in two ways from hydrostatic (Case 2a) and from seepage analyses (Case 2b). The FOS in both cases has been compared accordingly.

- **SLOPE/W**

The CSS and minimum FOS are presented in Fig. 3.5, which represents the computations related to the hydrostatic pore pressure distributions.

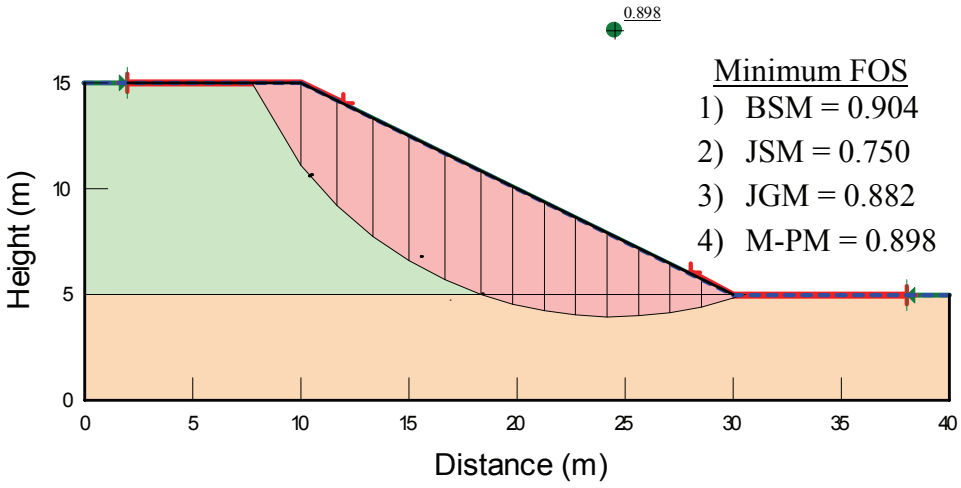

Fig. 3.5 CSS and FOS from SLOPE/W for Case 2a (hydrostatic pp)

For Case 2b, the pore pressure profile obtained from the seepage analyses was used. Accordingly, the pore pressure distributions were first analysed separately in SEEP/W, and then the analysed pore pressure was used in SLOPE/W for compilation of the corresponding FOS. The resulting CSS and the FOS obtained from the analysis are shown in Fig. 3.6. The SEEP/W software computes the pore pressure using finite element mesh, which can be seen in Fig. 3.6.

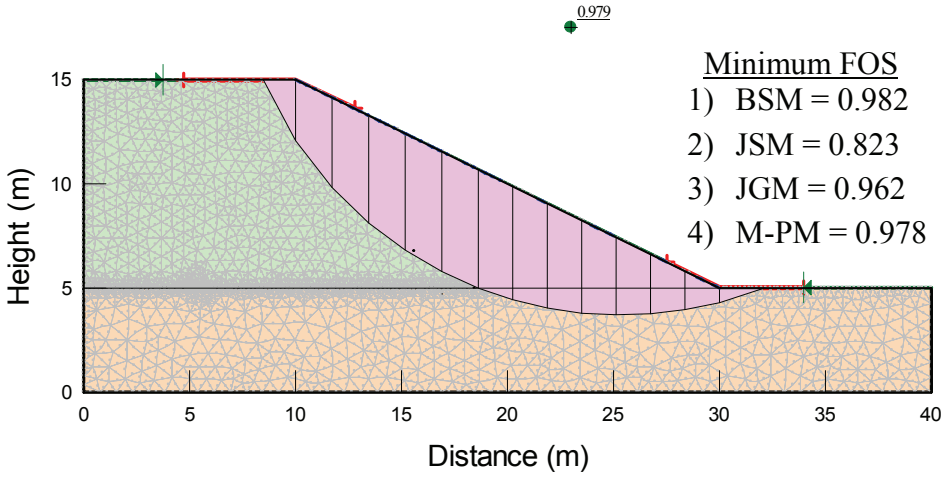

Fig. 3.6 CSS and FOS from SLOPE/W for Case 2b (pp from SEEP/W)

Taking the LE methods, the FOS was found 9% higher from seepage analyses than for hydrostatic distributions. SLIDE produced almost identical results, and they are hence not included here. The reason of higher FOS in Case 2b can be explained by the unchanged CSS even after the seepage analysis. This resulted in higher effective normal stress due to the lower average pore pressures along the CSS.

The flow field and equipotential lines generated by the seepage analysis in SEEP/W are shown in Fig. 3.7. The hydraulic boundaries, for example restriction of discharge along the base and the right side of the model, 15 m head on the left side boundary and zero pressure along the surface, were assumed. The hydraulic conductivity given in Table 3.1 was used in the seepage analysis. The steady-state flow condition was assumed in the seepage analysis. This means, the inflow of water in the slope will remain unchanged.

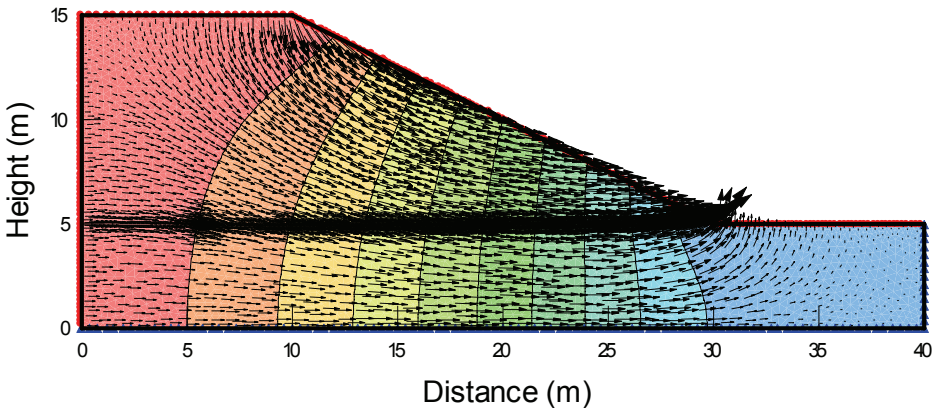

Fig. 3.7 Flow field and equipotent lines from SEEP/W

- **PLAXIS**

Similar pore pressure conditions were also studied in PLAXIS. The use of hydrostatic pore pressure distribution resulted in a lower FOS compared to steady-sate groundwater calculation. The resulted CSS and FOS are depicted in Fig. 3.8 and Fig. 3.9 for pore pressure from hydrostatic distributions and seepage analyses, respectively.

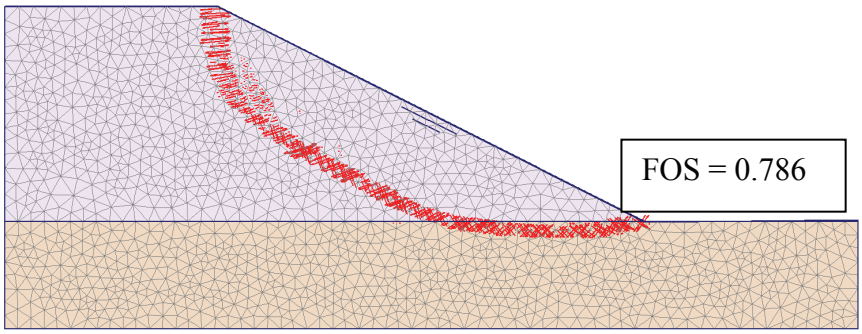

Fig. 3.8 CSS and FOS computed in PLAXIS for Case 2a (hydrostatic pore pressure)

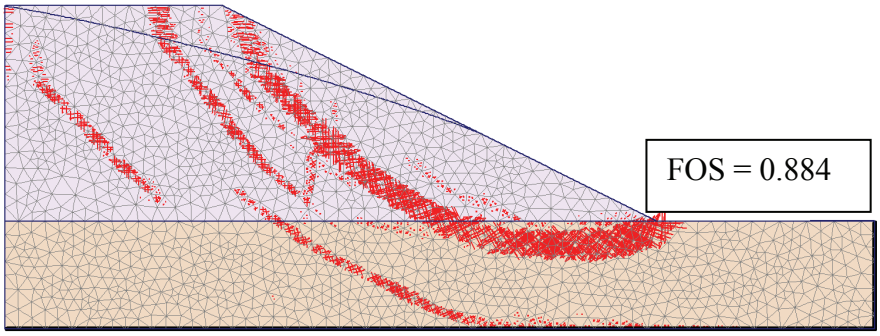

Fig. 3.9 CSS and FOS computed in PLAXIS for Case 2b (seepage analysis)

In PLAXIS, a FOS less than unity was computed using a manipulation in strength parameters to avoid numerical instability during the simulations. In this procedure, the real strength parameters were multiplied by a scaling factor and the computed FOS was divided by the same factor. Fig. 3.10 shows the flow field and phreatic surface obtained after the seepage analysis. The phreatic surface looks more realistic in PLAXIS compared to those obtained in SLEEP/W.

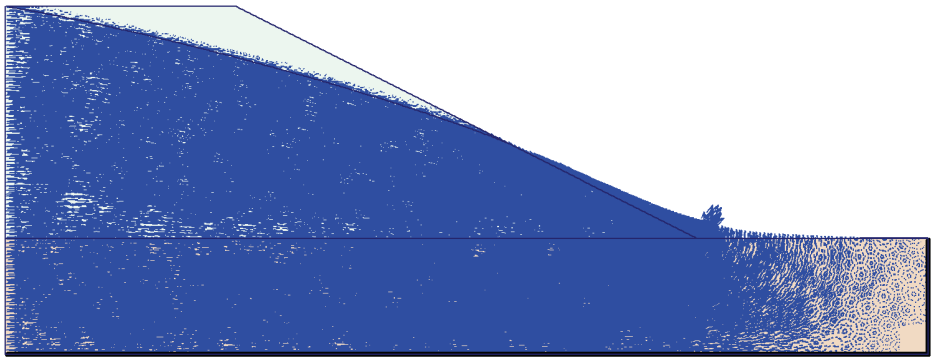

Fig. 3.10 Flow field generated by steady-state calculations in PLAXIS

The steady-state seepage analysis was conducted by locating the GWT on the surface and applying closed flow boundaries at the base and the right side of the model. Water flows solely into the soil from the left vertical boundary. In the slope, water may enter also through the horizontal terrain surface, which has not been considered in the model.

Compared with the two pore pressure conditions in PLAXIS, the FOS from seepage analysis was found 12.5% higher than that from hydrostatic distributions. Similar comparison was also made between LE and FE analyses for exactly the same condition. Accordingly, LE (M-PM) computed 10.6% higher FOS than in FE (PLAXIS) for the seepage analyses. Furthermore, the difference was found as large as 14.2% for hydrostatic pore pressure distribution, which may be unrealistic in real situations. However, the assumption of a hydrostatic pore pressure distribution increases the difference between LE and FE analyses.

3.2.2.3 Load Case 3: External forces

The last load case was analysed by the same software programs. Fig. 3.11 shows the CSS and the minimum FOS obtained from SLOPE/W. Similarly, the analyses results from SLIDE are given

Fig. 3.12. The FOS from both SLOPE/W and SLIDE is found almost identical (± 1%) compared to the method to method.

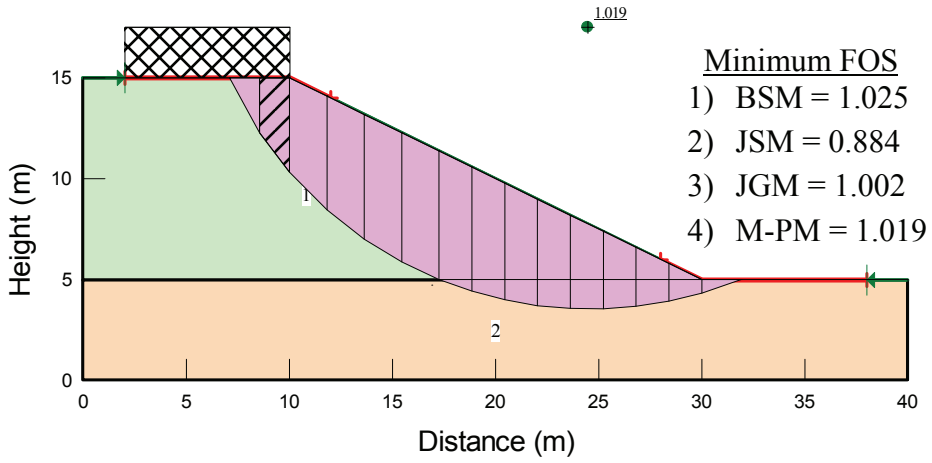

Fig. 3.11 CSS and FOS from LE analysis (SLOPE/W) for Case 3

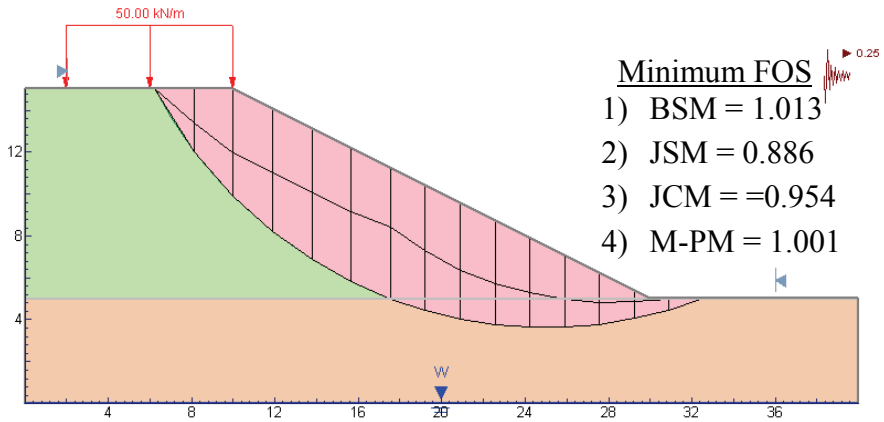

Fig. 3.12 CSS and FOS from LE analysis (SLIDE) for Case 3

In addition to the CSS in Fig. 3.12, the line of thrust, where the interslice normal force acts, can be seen. This line of thrust generated by SLIDE for M-PM was found at about 0.33h from the bottom of slices at the upper end (active side), nearly 0.6h in the middle and very high at the lower (passive side) where, h is the height of the slices. This broadly agrees with the Janbu (1973) assumption for the line of thrust in his GPS method.

The CSS and minimum FOS from PLAXIS are shown in Fig. 3.13. Due to the same external forces, the difference in FOS is found 9.6% between LE (M-PM) and FE (PLAXIS) analyses. Moreover, the CSS in FE analysis was found composite rather than circular as in LE analysis.

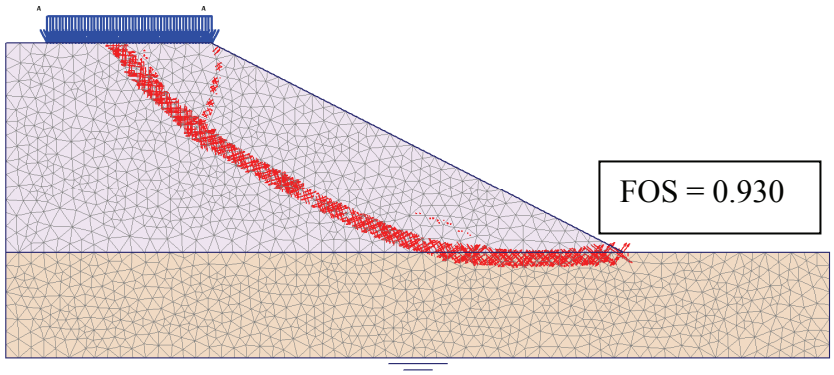

Fig. 3.13 CSS and FOS from FE analysis (PLAXIS) for Case 3

3.3 Comparison of methods

3.3.1 LE methods

The FOS has already been compared and discussed under each case analysis. Here, a more detailed study on the forces computed by SLOPE/W is presented for two identical LE methods (JG and M-P). The forces acting on slice #2 (see Fig. 3.11) have been indicated in Fig. 3.14.

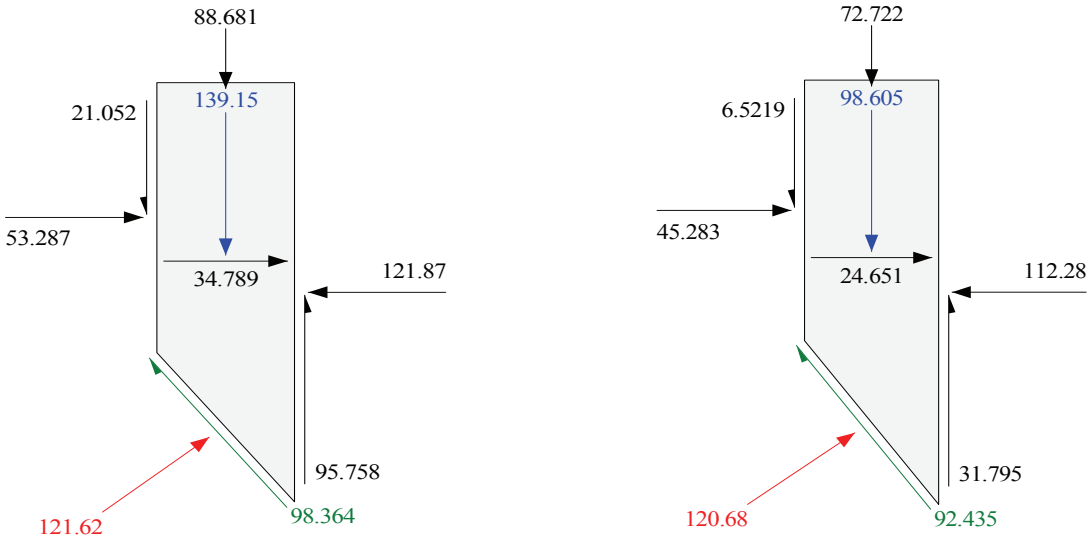

a) JGM (b = 1.77 m, h = 4.36 m) b) M-PM (b = 1.45 m, h = 3.77 m)

Fig. 3.14 Forces acting on slice #2 from LE analyses (SLOPE/W)

The CSS shown in Fig. 3.11 is from the M-P method and this surface is shallower than in JG method. This can be observed by comparing the slice height in Fig. 3.14. The forces (kN/m) cannot be compared directly since both widths and heights are different. However, the methods consider the similar forces acting on the slice in the same way. In addition, only the dead weight has been considered in both methods while computing the seismic force with α_h = 0.25. Hence, the effect of q = 50 kPa has not been considered to compute the horizontal seismic force.

Optimisation in SLOPE/W generates generally a non-circular CSS and lower FOS. The circular CSS (see Fig. 3.11) becomes non-circular, which can be seen in Fig. 3.15. Similarly, the optimised CSS in SLOPE/W looks almost identical to the CSS in PLAXIS (see Fig. 3.13). However, even after the optimisation, the FOS in LEM is higher than in FEM.

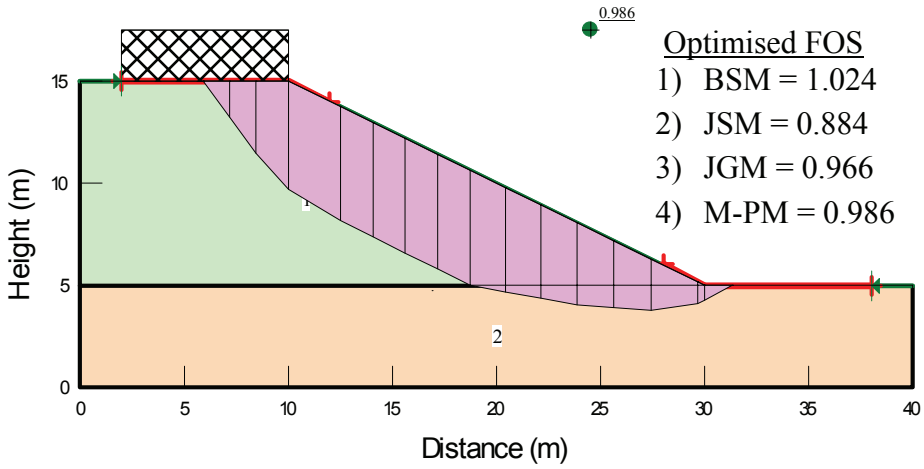

Fig. 3.15 Optimised FOS and CSS from LE analysis (SLOPE/W)

Table 3.3 shows the difference in FOS (Diff.) from non-optimised (No Opt.) CSS identified by M-P method to optimised (Opt.) CSS. The FOS from JG method relates to the same CSS. Here non-optimised and optimised refer to a circular CSS and non-circular CSS respectively. The study was carried out in more details for three load Cases.

Table 3.3 Effects of optimisation on FOS

Methods	FOS for Case 1			FOS for Case 2a			FOS for Case 3		
	No opt.	Opt.	Diff.	No opt.	Opt.	Diff.	No opt.	Opt.	Diff
JG	1.716	1.635	5.0 %	0.882	0.854	3.3 %	1.002	0.966	3.7 %
M-P	1.737	1.701	2.1 %	0.898	0.897	0 %	1.019	0.986	3.3 %

The study shows that the optimisation generally results in lower FOS for the most rigorous methods. The methods that satisfy either force (JS) or moment (BS) equilibrium show no changes, and hence these methods are not presented in Table 3.3. Also Case 2a (hydrostatic pore pressure) shows constant FOS, even after optimisation in the M-P method.

Fig. 3.16 shows the comparison among LE methods, which are indicated in the FOS versus λ diagram. According to GLE procedure, the FOS is computed for the common CSS for several λ values. In this way, the accuracy of the LE methods can be compared. The FOS for BS and JS methods can be found when λ is zero as indicated in Fig. 3.16. Similarly, a certain value of λ, which satisfies both force and moment equilibrium, gives the FOS for M-PM and SM.

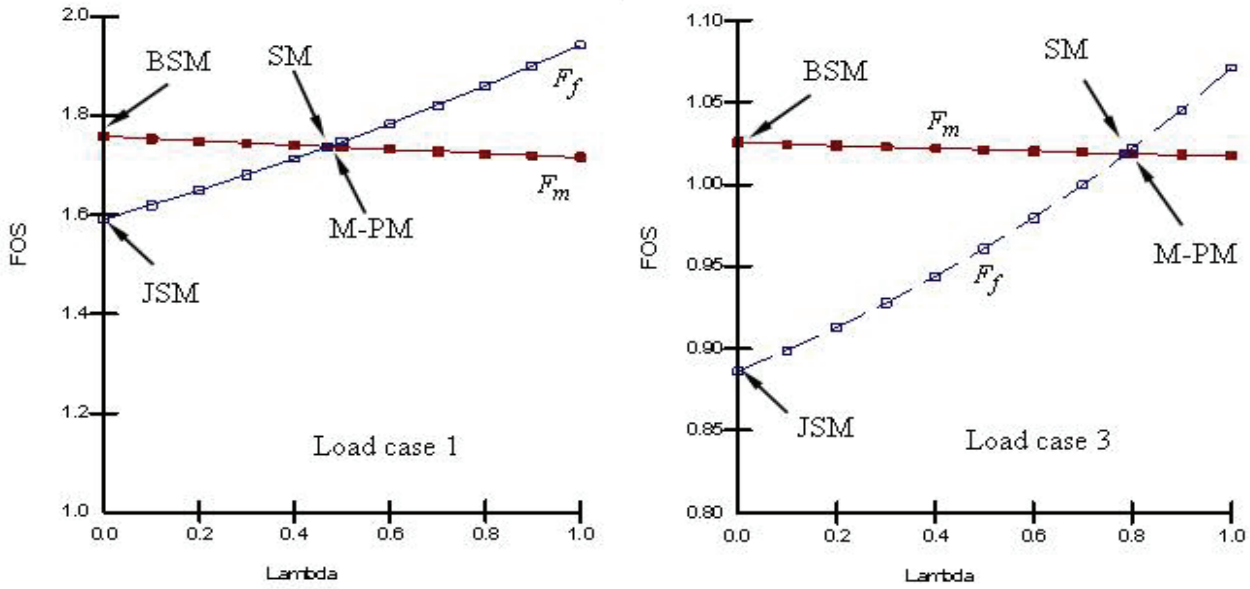

Fig. 3.16 FOS - λ plot (non-optimised) for Case 1 and Case 3

In circular CSS analyses, the force equilibrium FOS (F_f) is found more sensitive to the interslice shear force than the moment equilibrium FOS (F_m). This is the reason why the FOS from BSM does not vary much compared to JSM, as shown in Fig. 3.16.

3.3.2 FE and LE methods

Fig. 3.17 shows the computed FOS by PLAXIS for the load conditions presented before.

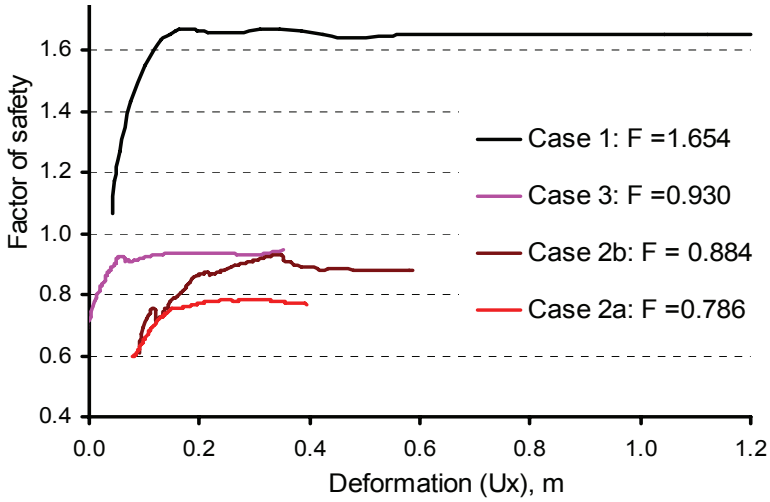

Fig. 3.17 FOS for the load conditions analysed from PLAXIS

Since the PLAXIS software is based on the constitutive law (stress-strain relationship), the CSS has been considered as the most critical one. Similarly, the FOS in the PLAXIS analysis should be close to the absolute minimum. Under these considerations, further comparison of LE (M-P) method has been carried out with respect to FE (PLAXIS) (0%).

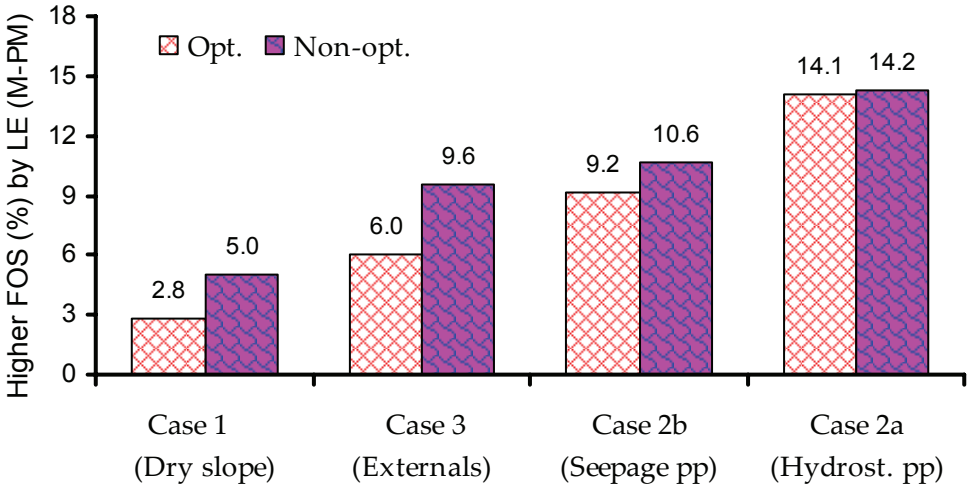

Fig. 3.18 Comparison of FOS between LE and FE analyses

The comparison of FOS computed by LE (M-PM) for optimised (Opt.) and non-optimised (Non-opt.) CSS is shown in Fig. 3.18. The FOS from LE (M-PM) analysis is found higher in all cases than that from FEM (PLAXIS) analysis, both for optimised and non-optimised CSS. In load Case 1, the LE analysis with optimisation reduces the difference between in FOS. In contrast to this, a large difference is found in the saturated slope for hydrostatic pore pressure distributions. As the external loads and GWT increase in a slope, the difference in FOS increases simultaneously. Moreover, the FOS is least affected by optimisation of the hydrostatic conditions. This indicates that LE analysis cannot adjust the changes in stresses with the change in strains during the simulation, which the FE method can handle more effectively.

3.3.3 Parameter studies

3.3.3.1 Dilatancy parameter

A positive contribution to the FOS was found by introduction of the dilatancy parameter in the FE analyses. This parameter describes the volume expansion of soils under plastic flow, particularly found in sand, silty sand and overconsolidated clays. The dilatancy angle (ψ) is related to the volumetric strain (ε_v^p) and axial strain (ε_a^p) in plastic conditions (Nordal 2002), and it is expressed by:

$$\frac{\varepsilon_v^p}{\varepsilon_a^p} = \frac{2\sin\psi}{\sin\psi - 1} \tag{3.2}$$

According to Nordal and Glaamen (2004), a modest improvement in FOS of about 6% can be found if the dilatancy angle is introduced in the FE analysis. In their study, the improvement was found for ψ about 10^0 less than the friction angle (ϕ). Also in this study, the use of ψ (= $\phi - 10^0$) in FE simulations gave significant increase in the FOS. Three load cases were simulated in PLAXIS and a range of the magnitude increase was found accordingly. The FOS from the PLAXIS analyses are compared in Fig. 3.19, where the FOS (legend) relates to the curves from top to bottom respectively. PLAXIS (2004) has incorporated ψ as a plastic potential function (g), which was discussed in Section 2.3.3.

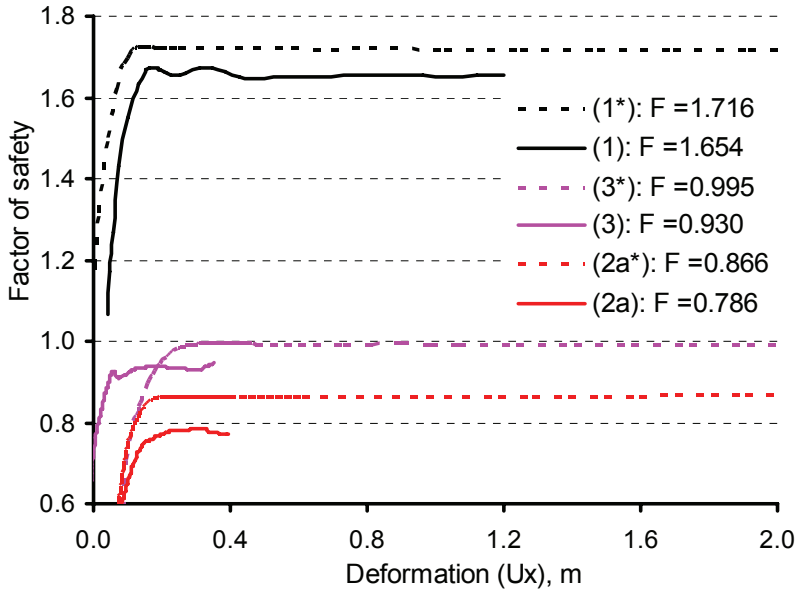

Fig. 3.19 Effect of the dilatancy parameter on FOS (* with $\psi = 20^0$, 15^0 for layers 1, 2)

Fig. 3.20 shows a range of improved FOS due to the application of ψ. As indicated, the improvement ranges from 4% in a dry slope to 10% in a saturated slope. It means, the difference between FOS from LE and FE analyses can be minimal if a dilatancy angle is introduced in the FE analyses, and an optimisation is carried out in the LE analyses.

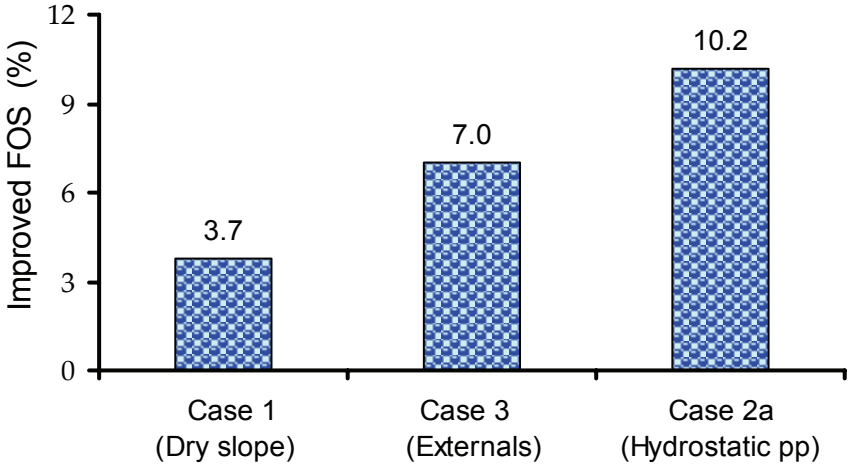

Fig. 3.20 Improvement in FOS by positive ψ ($\psi = 20^0$, 15^0 for layers 1, 2)

For Case 3, the use of a dilatancy angle in PLAXIS and the corresponding FOS (F = 0.995, see Fig. 3.19) is directly comparable to the FOS (F = 0.986, see Fig. 3.15) obtained from CSS optimisation in SLOPE/W (M-PM).

3.3.3.2 Interslice force function

The PLAXIS simulation was also used to compare the interslice force function, defined as T/E = λ.f(x). The interslice normal force (E) and shear force (T) were determined at 1 m intervals and plotted together with similar results obtained from SLOPE/W and SLIDE for the M-P method. Fig. 3.21 shows the comparison of the interslice force function for Case 3. The slope profile and the SS identified by PLAXIS are also plotted on the right axis, and indicated by the dotted lines.

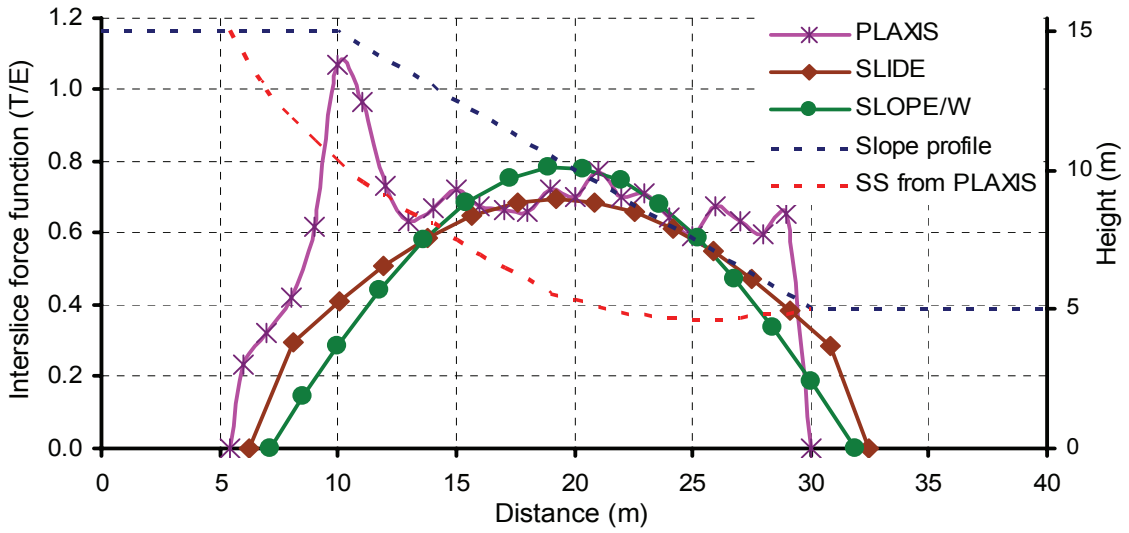

Fig. 3.21 Interslice force function for Load Case 3

The selected half-sine function in SLIDE and SLOPE/W results in almost identical shape. SLOPE/W finds exactly the same shape as half-sine function at λ = 0.8, whereas SLIDE shows a marginal difference in shape at a lower value of λ. In contrast, PLAXIS finds an irregular function with considerable difference at the crest and toe of the slope. The higher interslice shear force at the crest found in PLAXIS is the result of surcharge load. In the middle of the SS, the function is almost constant except few peaks. However, this may vary with the change in geometry and the load conditions, and thus cannot be generalised for all conditions. Nevertheless, the study shows that the interslice forces are not the same in LE and FE analyses, especially at the crest and toe of the slope.

3.3.3.3 Critical shear surface and line of thrust

The critical SS obtained from FE and LE analyses are compared in Fig. 3.22 again for Case 3. The FE analysis finds the SS at more shallow depths compared to the LE analysis. Both SLOPE/W and SLIDE (M-PM) have identified almost the same SS. In contrast, the PLAXIS analysis has

identified a slightly different shape Thus, it can be concluded that the CSS obtained from the LE and FE analyses are not the same. This results in further difference in normal and shear stresses, and subsequently in the FOS. Furthermore, the CSS from PLAXIS is found composite SS (plane in the middle and circular at ends), as first defined by the GPS method (Janbu 1973).

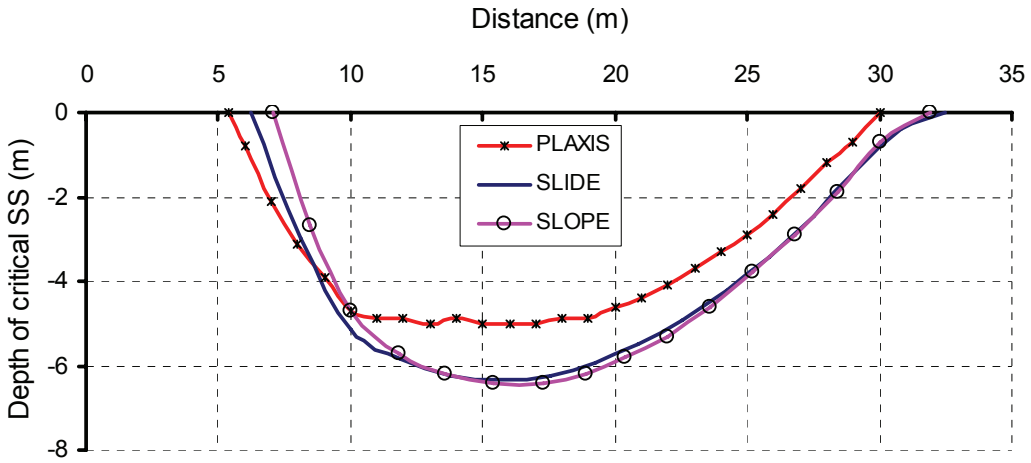

Fig. 3.22 Critical SS from FE and LE methods for Load Case 3

Likewise, the lines of thrust obtained from SLIDE (M-PM) and PLAXIS are compared in Fig. 3.23. The right side axis is again related to CSS and slope profile as in Fig. 3.21. The comparison shows that the application points of interslice normal force in FE and LE analyses are not the same. However, the location may vary with the change in geometry and the load conditions.

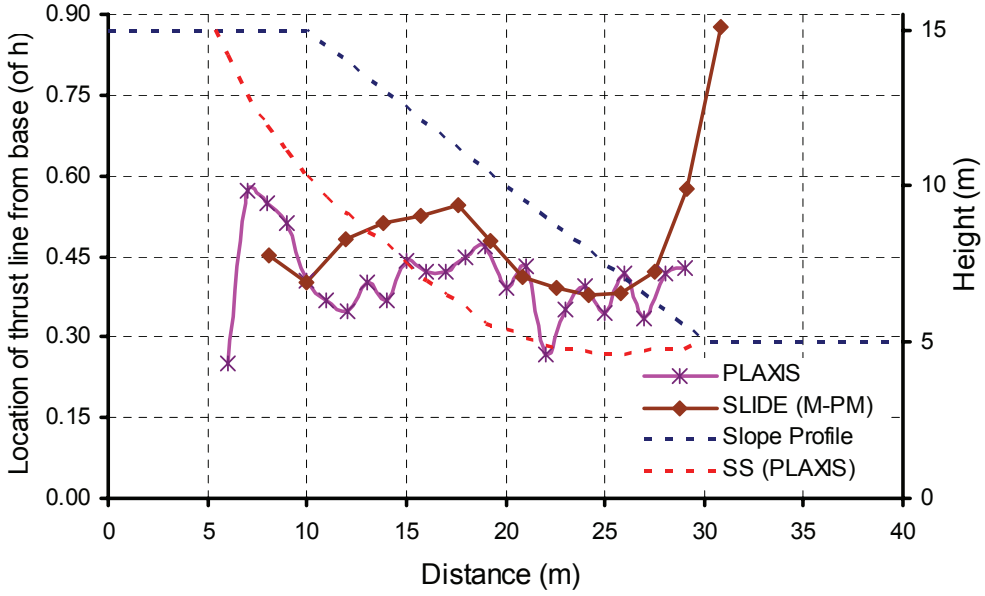

Fig. 3.23 Location of the line of thrust from FE and LE methods for Load Case 3

In this analysis, M-PM gives the line of thrust lower at the crest; slightly higher in the middle and unreasonably high at the toe (see Fig. 3.23 and Fig. 3.22). This finding indicates that the sine function does not represent the static situation very well particularly in the toe region. Ideally the thrust line, for example in Janbu's GPS method, should be located between 0.2h and 0.4h from the base of the SS, where h is the height of the slices (Abramson et al. 2002). Janbu (1973) also states, "the line of thrust should be located somewhat lower than h/3 from the SS in the active zone (crest) and higher than h/3 in the passive zone (toe) for cohesive soils". Thus, the unlike line of thrust and the interslice force function in the LE and FE analyses may further explain the differences in base normal force and hence the difference in FOS.

3.3.4 Summary of the comparative study

The LE and FE analysis methods are based on two different principles, and hence the analysis approaches result in difference in commutated FOS. The conducted study of the simple slope analyses with various load conditions shows that LE (M-P) analysis always computes higher FOS ranging from 5 – 14% compared to the FE (PLAXIS) analysis. However, the difference in FOS may be limited to within 5% even in the worse case, i.e. fully saturated conditions, if the FE analysis is performed with a positive dilatancy angle about 10^0 less than the angle of friction, and the LE analysis with optimisation of the circular CSS. More elaborated discussions on the comparisons between the LE and FE methods have been presented in Chapter 7.

Chapter 4

Data Collection for Case Study

4.1 Site visit for case study

Site visits were performed for the case study taken from Middle Marsyangdi Hydroelectric Project (MMHEP) in Nepal. The purpose of the visits was to collect necessary data, reports, and soil samples for subsequent laboratory investigations. However, the final aim was to use the investigated shear strength parameters in slope stability evaluations. In addition, the aim of the visits was to evaluate existing conditions in the slopes situated at dam site left bank (LB) (see Fig. 4.1) and powerhouse area (see Fig. 4.2). The project with 76 MW installed capacity aims to generate 470 GWh of annual energy from year 2007 (CES 2005).

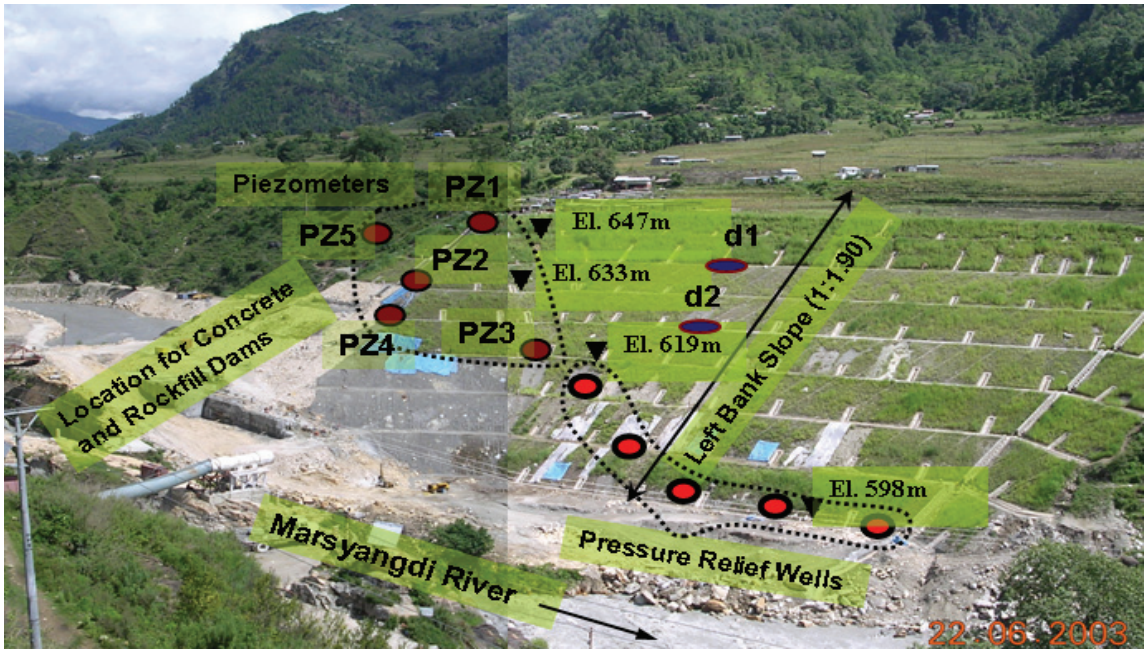

Fig. 4.1 Dam site LB slope (MMHEP) in Nepal (photo from 2003)

At the time of the first site visit in June 2003, the dam site LB slope was graded permanently, vegetations were planted and drainage systems were constructed as shown in Fig. 4.1.

Primarily, two types of soil origins were found in the dam site LB slope. The upper layer consists of alluvial material, whereas the lower layer originates from mudflow deposit from a sudden large-scale mudflow event (Yamanaka & Iwata 1982). Though there is not a very distinct layer boundary, the upper layer is assumed to reach up to El 633 masl in the present study. Likewise, the lower layer is assumed to reach El. 589 masl, from where a stiffer soil is expected.

Similarly, the powerhouse slope (see Fig. 4.2) was excavated temporarily, and covered partly by plastic to minimise surface erosion. Besides this, there were drainage systems in the slopes further right of the penstock alignment. The soil boundary is dominated by alluvial deposits on the upper terrace up to El. 540 masl. The lower terrace consists of glaciofluvial deposits approximately down to El. 520 masl (Fichtner 2003).

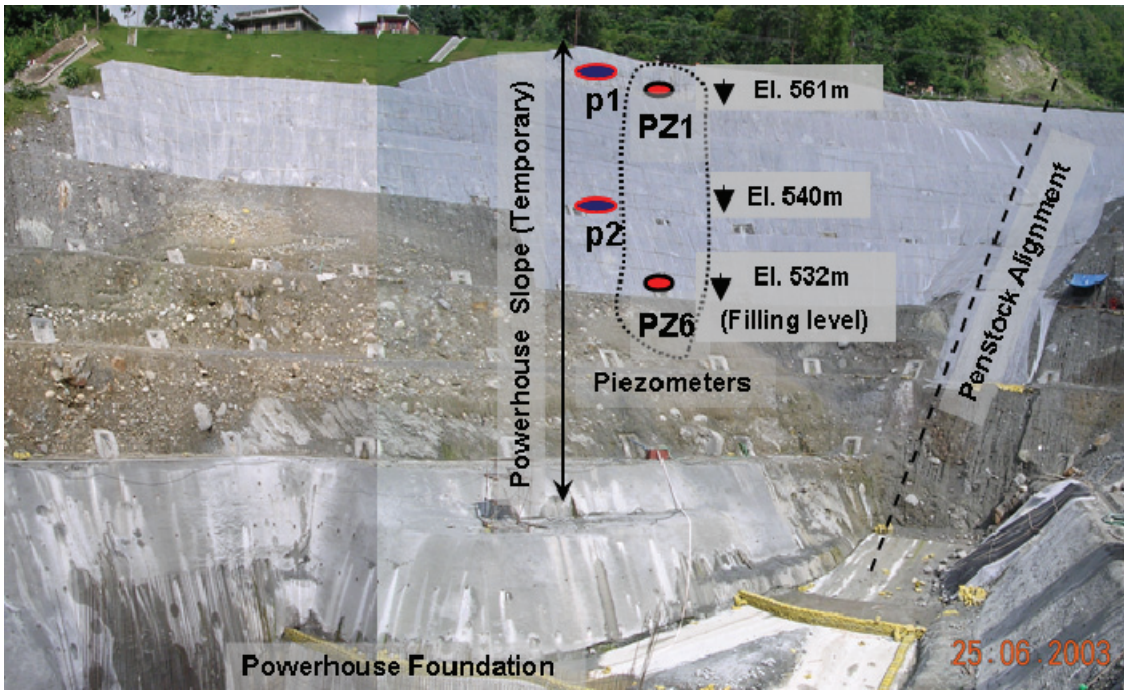

Fig. 4.2 Powerhouse slope (temporary) at MMHEP in Nepal (photo from 2003)

The visits were successful with respect to collection of the following data and information from the project site:

- relevant geological, geotechnical and hydrological data,
- previous test results, design parameters and calculations for slope stability analyses,
- information about groundwater and installed instrumentation in the slopes,
- collection of soil samples from the slopes for subsequent laboratory investigations, and
- in situ index tests, site photographs, drawings, standpipes and piezometer records, etc.

4.2 Instrumentation

The dam site LB slope has been instrumented with five open type standpipes piezometersclose to the dam axis (see Fig. 4.1). The purpose of these piezometers is to monitor the groundwater table (GWT), variations during construction period as well later during operation. In addition, five-pressure relief wells are planned for installation along the base of the slope as indicated in Fig. 4.1. Likewise, there will be inclinometers installed in the slope to monitor deformations and slope movement. The powerhouse slope is instrumented with two piezometers installed as shown in Fig. 4.2. Further piezometer and inclinometer installations are planned. The recorded GWT for both case studies are presented later sections in this Chapter.

4.3 Drainage systems

Both surface and sub-surface drainage systems have been constructed in the dam site LB slope. Accordingly, 15–25 m long perforated horizontal drainage pipes have been installed. In addition, surface run-off has been channelled along the berms that have been constructed at every 7 m height on the slope (refer Fig. 4.1). Moreover, vegetation has been planted on the slope to minimise surface erosion and reduce percolation during the monsoon period. As a result, a certain level of suction can be expected above the GWT.

Similarly, the permanent slopes in the powerhouse area will have the same provision as in the dam site LB slope. However, more seepage water was seen from the powerhouse slopes above the switchyard area and additional drainage pipes were being installed during the first visit.

4.4 Soil sampling

Four disturbed soil samples, but representative to the case slopes were collected from the locations marked in Fig. 4.1 (d1, d2) and Fig. 4.2 (p1, p2). As said above, the purpose of sampling was to obtain samples for subsequent laboratory investigations. These investigations were carried out to characterise the materials and determine relevant parameters for slope stability analyses. The sampling locations and symbols are summarised in Table 4.1. The laboratory investigations of the soil samples have been presented in Chapter 5.

Table 4.1 Sampling location and adopted symbols

Site	Sample	Location	Sampling method
Dam site LB slope	d1	Slope at El. 640 masl	Disturbed (bag) samples were collected from natural soil deposits about half a meter below the existing ground surface.
	d2	Slope at El. 626 masl	
Powerhouse slope	p1	Slope at El. 561 masl	
	p2	Slope at El. 540 masl	

4.5 Climatic conditions

The case study area with its tropical climate has strong monsoon rainfalls in the months of June, July and August. According to the altitude, the temperature varies from place to place and season to season. The dam site and powerhouse area is located between elevations 500 - 700 masl. The temperature can be experienced up to 40 ^{0}C in the summer, whereas it may drop down to 5 ^{0}C in the winter. Similarly, spatial variations in rainfall can be experienced. The eastern part of the country gets more rain compared to the western. The maximum annual rainfall (>4000 mm) has been recorded at a place called Lumle near Pokhora, which is not far from the MMHEP site. Table 4.2 shows average annual rainfall for both a 10-year period (1994-03) and year 2003 recorded at the nearest three rainfall stations in Lamjung district (DHM 2004).

Table 4.2 Rainfall records in nearby three stations (DHM 2004)

Station name	District	Index No	Elevation (masl)	10 yr avg (mm)	Yr 2003 (mm)
Kudi Bazar	Lamjung	0802	823	3526	3849
Kunchha	Lamjung	0807	855	2794	2620
Gharedhunga	Lamjung	0823	1120	3204	3665

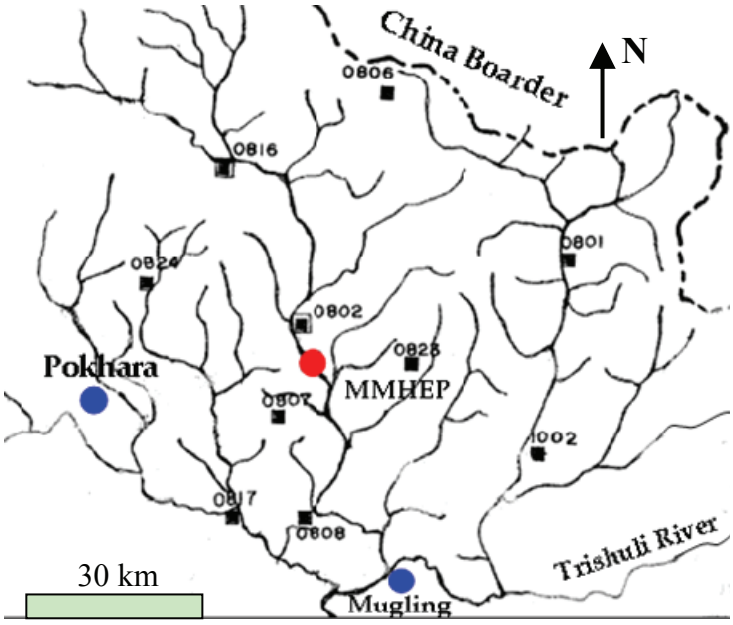

Fig. 4.3 Location of rain gauges around the MMHEP (DHM/N 2004)

The rainfalls stations located around the project site are shown in Fig. 4.3. The Marsyangdi River valley is close to the Annapurna Himalaya range along the China boarder and thus, a lot of rainfall occurs in the monsoon. The ten years average annual rainfall (3200 mm) indicates that the project area will have a substantial amount of rain every year (data source: DHM/N 2004). Out of this, nearly 70% rainfall occurs in the monsoon period. During this period, geohazards

due to the landslides and floods are experienced all over the country. Fig. 4.4 shows the average monthly rainfall variations with a peak of more than 1100 mm in the year 2003, whereas the 10 years average is slightly lower. This shows that not only the monthly rainfall variation is large, but the yearly variation in the monsoon period may also be higher around the project area.

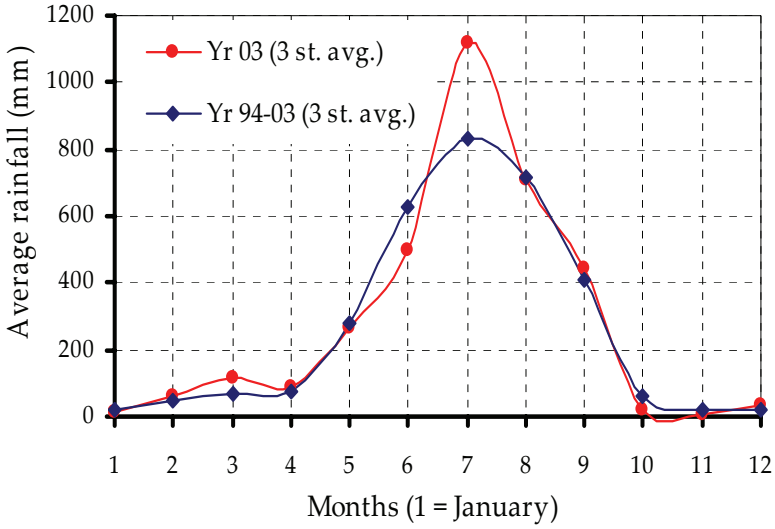

Fig. 4.4 Average monthly rainfall distribution from nearby stations

4.6 Groundwater records

The groundwater records for the slopes were obtained from the piezometer installations. Fig. 4.5 shows the GWT in the dam site LB slope. The elevation shown refers to the ground elevation where the piezometers are installed. The piezometer, DPZ3 has some missing records due to a fault. Even higher GWT especially at the toe of the slope can be expected when the reservoir level is increased to El. 626 masl during the power plant operational stage.

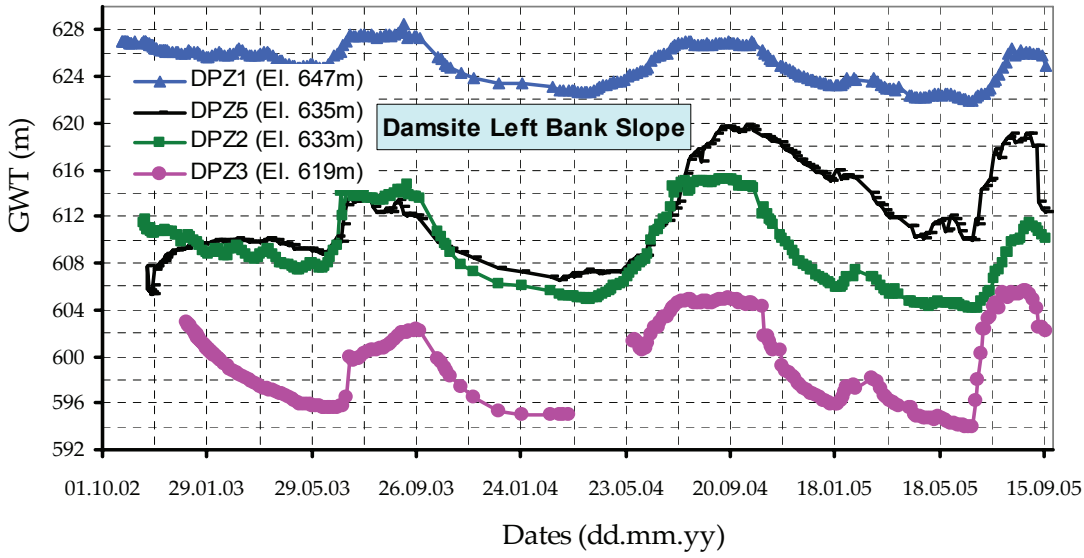

Fig. 4.5 Groundwater variations on the dam site LB slope (Fichtner 2005)

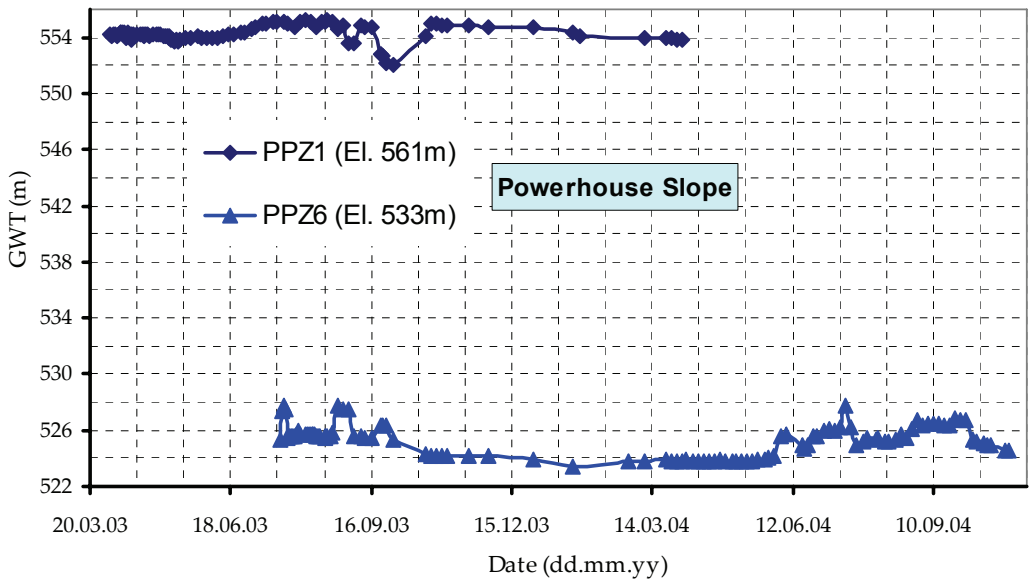

Fig. 4.6 Groundwater variations in powerhouse slope (Fichtner 2005)

Similarly, two piezometer readings from the powerhouse slope are shown in Fig. 4.6. The upper piezometer has no recordings after March 2004 due to some technical problems of the equipment. Compared to the dam site LB slope, there are very little fluctuations in GWT in this slope. This indicates that there is a continuous source of groundwater in the slope. Groundwater springs were also observed in the nearby areas during the site visit in June 2003.

The GWT, which has been included in the slope stability analyses, is summarised in Table 4.2. Among the five piezometers at the dam site (see Fig. 4.1), four are functional (see Fig. 4.5) and out of them, three (except DPZ5), are considered useful to define the GWT and pore pressure variations for stability analyses. DPZ5 is located further upstream and is not relevant for the considered slope profiles.

Table 4.3 Input parameters for the groundwater table (GWT) (Fichtner 2005)

Slope location	Piezometer	Ground El.	GWT (masl)	
	Reference	(masl)	Dry season	Wet season
Dam site LB	DPZ1	647	623	628
	DPZ2	633	605	615
	DPZ3	619	595	605
Powerhouse	PPZ1	561	553	555
	PPZ6	533	524	527

The highest GWT represents the wet season conditions, whereas the lowest GWT indicates the dry season, and defined accordingly in slope stability analyses in Chapter 6.

4.7 Seismic study

Nepal lies in a seismically active zone where the seismic events are results of tectonic settings in the Himalayas. The northward motion of the Indian plate underneath Tibet continues today at an estimated rate of about 30 mm per year (Dixit et al. 1999). This induces wide spread deformation, faulting and thrusting of rocks, giving rise to the mountains. Moreover, seismic activity in the Himalayan range is particularly related to the faulting and thrusting caused by the Main Central Thrust (MCT), the Main Boundary Thrust (MBT) and the Main Frontal Thrust (MFT) (NSCN 1994).

Historical earthquakes of higher magnitude have occurred due to the faults and thrusts. Recent studies indicate that devastating earthquakes are inevitable in the long-term (Dixit et al. 1999). The project site-specific seismic hazard study has reported major earthquakes with magnitudes between M 6.4 and M 8 occurred within 200 km distance (Nepal & Olsson 2001).

Seismic forces travel some distance from the origin before their effects can be seen on the ground. Site-specific hazards depend on the intensity of ground shaking, the frequency of the ground and the structure, duration of shaking and the magnitude of earthquakes. Moreover, earthquakes are considered as random events and thus the associated ground response, i.e. peak ground acceleration (PGA), is assumed to be lognormal distributed (SILT 2001). The level of continuous ground shaking is usually in the order of 60% of PGA, but the seismic design coefficients are suggested to scale down to 35% of PGA based on the risk analysis (ICOLD 1989).

According to the risk analysis, seismic design coefficients for the project were suggested for two levels of earthquakes. One is operating basis earthquakes (OBE) and the other maximum design earthquakes (MDE). Accordingly, horizontal seismic design coefficients (α_h) for bedrock were recommended for two levels; as 0.16 for OBE and 0.25 for MDE conditions. Moreover, the recommendation for OBE level was based on a return period of 200 years, whereas the MDE level was based on a return period of 1000 years (SILT 2001).

Based on the site-specific seismic study, a value of α_h = 0.15 was selected for pseudo-static slope stability analyses (Fichtner 2000). However, for the spillway foundation design, a higher value of the horizontal (α_h = 0.33) and vertical coefficients (α_v = 0.16) were recommended, based on the MDE level and the local ground conditions (Nepal & Olsson 2001).

4.8 Previous test results

Extensive geotechnical investigations were carried out during the detailed feasibility study for the project (Fichtner, NEA, NGI, SILIT 2000/2001). In the field investigations for the dam and powerhouse sites, several boreholes were drilled and test pits were excavated for subsequent laboratory investigations. The selected test results are summarised in the following sections.

4.8.1 Index tests

Two tests from dam site LB area (DPT-8, DPT-11) and two tests from powerhouse area (PTP-2, PTP-4b) were selected among many others. Their index properties are given in Table 4.4. These samples carried more fines compared to the others, and hence could be representative to silty sand similar to the soils found in the present study.

Table 4.4 Summary of previous index tests (Fichtner, NEA, NGI and SILT 2000/2001)

Test no.	Moisture content	Compaction test		Perme-ability	Grain density	Grain size distribution (%)		
		($\gamma_{d(max)}$)	(OMC)			Fines	Sand	Gravel
	w (%)	(kN/m^3)	w (%)	k (m/s)	ρ_s (g/cm^3)	<75 μm	< 2 mm	>2 mm
DTP-8	13.0	20.1	10.4	2 10^{-7}	-	31	49	20
DTP-11	9.0	20.7	8.5	8 10^{-7}	-	26	33	41
PTP-2	10.0	18.1	12.8	7 10^{-5}	-	19	39	42
PTP-4b	13.4	17.4	7.5	-	2.67	35	44	21

The test samples were collected from the excavated pits close to the ground surface. As a result, other tests (not included here) showed coarser fractions, and accordingly the soils were classified as either gravelly sand or sandy gravel (Fitchner 2001). Therefore, the index properties given in Table 4.4 can be regarded as indicators to describe the non-homogeneous properties of the soils. The permeability coefficients are similar to those obtained in the present tests (refer Chapter 5).

4.8.2 Direct shear box and triaxial tests

4.8.2.1 Direct shear box tests

Table 4.5 shows the shear strength parameters obtained from the direct shear box tests. The compaction details were not available. The strength parameters from direct shear box tests are generally higher compared to the triaxial tests, which is discussed in the following section.

Table 4.5 Summary of direct shear tests (Fichtner and NEA 2001)

Test no.	c (kPa)	ϕ (^{0})	Test no.	c (kPa)	ϕ (^{0})
DTP-8	20	40.5	PTP-2	0	41.7
DTP-11	20	40.5	PTP-4b	0	51.6

Fig. 4.7 also shows the results from direct shear box test on samples of the mudflow deposit from the dam site LB slope (Nepal & Olsson 2001). The cohesion ranges from 12 to 14 kPa and the friction angles from 32° to 42°, depending on the strain levels. The lower range parameter

values are very close to the results obtained from drained triaxial tests in this study; see the triaxial test results in Chapter 5. The direct box shear tests for alluvial materials (not presented herein) showed even higher variations in the strength parameters. Exceptionally high variations were found in the cohesion (0 to 50 kPa) and friction angles (27 to 46^0) (Fichtner, 2001).

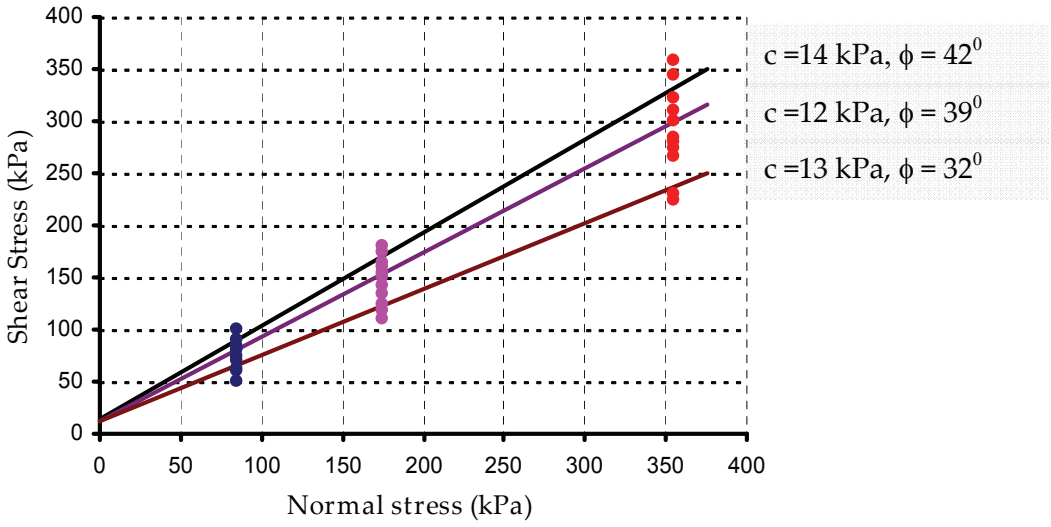

Fig. 4.7 Results from direct shear box test on "mudflow" material (Nepal & Olsson 2001)

4.8.2.2 Triaxial tests

Previous triaxial tests results with consolidation stresses are presented in Table 4.6. Two samples, DTP9 from the dam site LB ("mudflow" deposits) and PTP4 from the powerhouse (alluvial deposits), were tested in anisotropically consolidated ($K'_0 = 0.43$), undrained conditions for disturbed samples (NGI 2001). In addition, the tests were conducted at low axial strain rates (1- 1.5 %/hr) for larger size specimens (A = 40 cm^2, h = 14 cm). Based on the grain size distribution of PTP4 sample (34 % fines, 56 % sand and 10 % gravel), the material was accordingly classified as silty sand, the same as the material investigated in Chapter 5.

Table 4.6 Previous triaxial test results (NGI 2001)

Test no.	w_i (%)	γ (kN/m^3)	σ_1' (kPa)	σ_3' (kPa)	B (%)	c′ (kPa)	$\phi'(^0)$
DTP9.1	10.7	22.8	467	198	97.2		
DTP9.2	10.7	22.8	736	316	90.8	20	40
DTP9.3	10.9	22.8	939	404	95.2		
PTP4.1	14.7	22.1	170	72	98.5		
PTP4.2	16.0	22.0	290	122	98.5	4	34
PTP4.3	15.4	22.1	470	198	97.2		

The effective stress paths and the failure envelop for each test were drawn at ε = 2 % strain by NGI (2001). The summary plots were drawn from individual stress paths, and the test results for DTP sample and PTP sample are given in Fig. 4.8. The strength parameters obtained from these plots are given in Table 4.6.

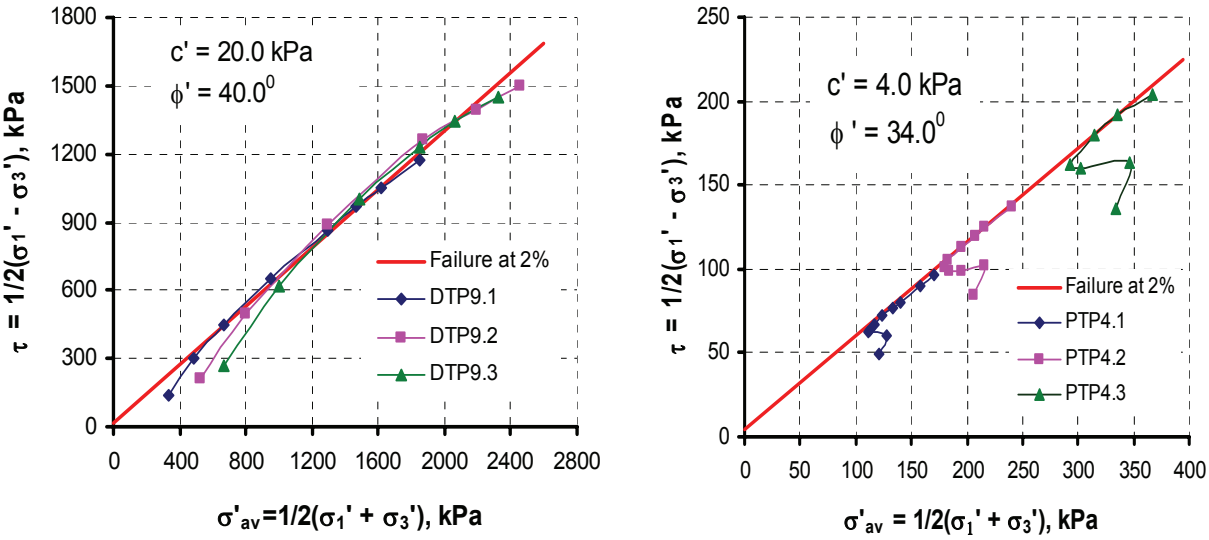

a) "Mudflow" deposits (dam site LB slope) b). Alluvial deposits (powerhouse slope)

Fig. 4.8 Previous triaxial test results for "mudflow" and alluvial deposits (NGI 2001)

Based on the triaxial test results, the shear strength parameters were selected for previous slope stability computations. Despite the saturated specimens (see Table 4.6), the high cohesion found in the mudflow material was neglected assuming that this might have appeared due to the suction presented in unsaturated condition (Fichtner 2001). The strength parameters from direct shear box tests (not effective) and previous triaxial tests (effective) are compared in Table 4.7. The selected strength parameters for the stability analyses are also given in Table 4.7.

Table 4.7 Strength parameters from previous tests (Fichtner 2001, Nepal & Olsson 2001)

Parameters	Mudflow deposits (dam site)			Alluvial deposits (powerhouse)		
	γ (kN/m^3)	c′ (kPa)	ϕ′ (°)	γ (kN/m^3)	c′ (kPa)	ϕ′ (°)
Direct shear box test	21.5	25	40	21.5	5	41
Triaxial test	23	20	40	22	4	34
Selected parameters	23	0	40	22	0	35

The strength parameters from the previous triaxial tests are on higher side for the mudflow deposits than the present triaxial tests (refer Chapter 5). The present undrained triaxial tests

show the cohesion in the range of 5-10 kPa and friction angle 30-33^0. However, these parameters are slightly higher (c = 10-14 kPa and ϕ = 32-34^0) in drained triaxial tests at higher strain levels.

4.9 Previous stability evaluations

4.9.1 Soil stratification

In the previous stability analyses, the top soil layer at the dam site LB was assumed about 10-15 m deep (see Fig. 4.1). Moreover, the layer had originated from alluvial deposits of silty sand, which contain sub-rounded to sub-angular pebbles of quartzite, gneiss and schist. The middle layer was identified as "mudflow" deposits, which was assumed to extend to the bedrock or stiffer soils. The mudflow had fractions of silty fine sand and gravel with calcareous cementation (Fichtner 2000). In such materials, it was difficult to get undisturbed samples. Nevertheless, the material seemed to be high cohesion, low porosity and low permeability from the visual inspection (Brauns 2000).

Similarly, the powerhouse slope (see Fig. 4.2) was found to consist of alluvial deposits about 15 m thick, reaching up to El. 554 masl. Below, grey-coloured glaciofluvial deposits of 25 m thick was assumed up to the El. 530 masl, where about 10 m thick sand layer was found. This layer was followed by the bedrock at approximately El. 520 masl. The slope area in general was found to consist of fine to medium-grained sand and silt with the presence of boulders, cobbles and pebbles with few clayey pockets (Fichtner 2000).

4.9.2 Groundwater conditions

In the dam site LB slope, the GWT was considered at the maximum daily poundage level (El. 626 masl) for the previous stability analyses. However, more details of the pore pressure distributions used in the previous analyses were not found. It has been found from the present analyses (refer Chapter 6) that the assumptions of porepressure distributions, for example horizontal GWT and hydrostatic distributions or inclined GWT and phreatic level correction or seepage analysis, have large variations in both location of CSS and FOS. Similarly, the GWT, which was found 8 m below the ground surface at the crest and 3 m below at the toe, was used to analyses the powerhouse slope (Fichtner, 2001). The present recordings of GWT have been found couple of meters higher than the previous GWT assumptions, referring to the standpipes readings (DPZ1 and PPZ1, see Table 4.3).

4.9.3 Shear strength parameters

The selected shear strength parameters given in Table 4.7 were used in the stability analyses. The parameters for both mudflow and alluvial deposits were considered for the dam site LB slope stability analyses. However, the powerhouse slope was assumed to consist of a single soil layer and analysed using the strength parameters applicable to alluvial deposits. The reason for

this simplification was the erratic distribution of silt and sand with some minor gravel and clayey pockets between the upper and lower terraces (Fichner 2001). This assumption proved to be representative, since the shear strength results for the samples p1 and p2, obtained from the present study, turned out to be the same (see Table 5.6 in Chapter 5).

4.9.4 Stability analyses and results

Previous static stability analyses were performed with three different computer programs: SLIDE, XSTABL and STABLE. Similarly, dynamic analysis was carried out in PLAXIS (Fichtner, NGI 2001). Bishop's simplified method and Mohr-Coulomb failure criterion for the shear strength were considered in the analyses. In addition, both deep and shallow circular CSS were analysed and accordingly, the minimum FOS was limited to 1.5 and 1.25, respectively. Similarly, the FOS of 1.05 was regarded as the absolute minimum for the pseudo-static analysis (Fichtner 2001).

Since the CSS is not circular in the frictional soils, the stability of the slopes was also evaluated by hand-calculation methods. Accordingly, an infinite slope was assumed and the following relationships were used in the computations (Abramson et al. 2002, Fichtner 2001).

- Without any external forces, i.e. self weight (static):

$$F = \frac{\tan\phi'}{\tan\beta} \tag{4.1}$$

- With earthquake in addition to self weight (pseudo-static analysis):

$$F = \frac{\tan\phi'}{\tan\beta}\frac{(1-\alpha_h\tan\beta-\alpha_v)}{(1+\alpha_h\cot\beta-\alpha_v)} \tag{4.2}$$

- Seepage parallel to the slope inclination:

$$F = \frac{\gamma'}{(\gamma'+\gamma_w)}\frac{\tan\phi'}{\tan\beta} \approx \frac{\tan\phi'}{2\tan\beta} \tag{4.3}$$

- Seepage in horizontal direction:

$$F = \frac{(\gamma'-\gamma_w\tan^2\beta)}{(\gamma'+\gamma_w)}\frac{\tan\phi'}{\tan\beta} \le \frac{\tan\phi'}{2\tan\beta} \tag{4.4}$$

where,

ϕ' = effective friction angle,

β = slope inclination angle,

α_h / α_v = seismic coefficients in horizontal/vertical directions,

$\gamma' = \gamma - \gamma_w$ = submerged or effective unit weight of soils, and

γ_w = unit weight of water.

The Eqs. (4.3) and (4.4) show that the stability of a slope in cohesionless soils is significantly reduced due to the presence of groundwater. However, the effect of pore pressure in the mudflow deposits will be negligible since deep-seated failures are not expected (Fichtner 2001). In addition, the failure surface above the GWT in the moist zone will involve apparent cohesion or suction due to pore water-air pressure, which increases the safety of the slope. However, this situation may not exit during the monsoon period, when the top few meters is saturated due to the rainwater. The results from previous stability analyses are presented in Table 4.8.

Table 4.8 Summary of previous stability analyses (Fichtner 2001)

Slope	Loads cases	SLIDE software	Hand-calculation methods	Recommended minimum FOS
Dam site LB slope	Static, local	1.33	1.22	1.25
	Static, global	1.63	1.59	1.50
	Pseudo-static	1.17	1.14	1.05
Powerhouse slope	Static, local	1.36	1.33	1.25
	Static, global	1.53	1.61	1.50
	Pseudo-static	1.08	1.12	1.05

The FOS obtained from hand-calculations was regarded as indicative value. The friction angle (40^0) for the mudflow materials was used for the dam site LB slope, whereas the powerhouse slope was analysed assuming alluvial soil conditions, which has lower friction angle (35^0). The analyses carried out by the proper use of soil layers, as explained in Section 4.9.1, and properties in SLIDE was also found similar to the hand-calculations, and hence, both the slopes at dam site LB and powerhouse were designed accordingly (Fichtner 2001).

Chapter 5

Laboratory Investigations

5.1 Soil phase diagram

Natural soils consist of three phases; solids, liquids and gas. A mixture of these phases has been shown in Fig. 5.1 by a schematic phase diagram, which shows a complex soil skeleton. Basic soil properties are important parameters not only to classify and identify the soils, but also to understand the soil behaviour. Moreover, the diagram is convenient for derivation of important phase relationships since the weight and volume of each phase cannot be directly measured.

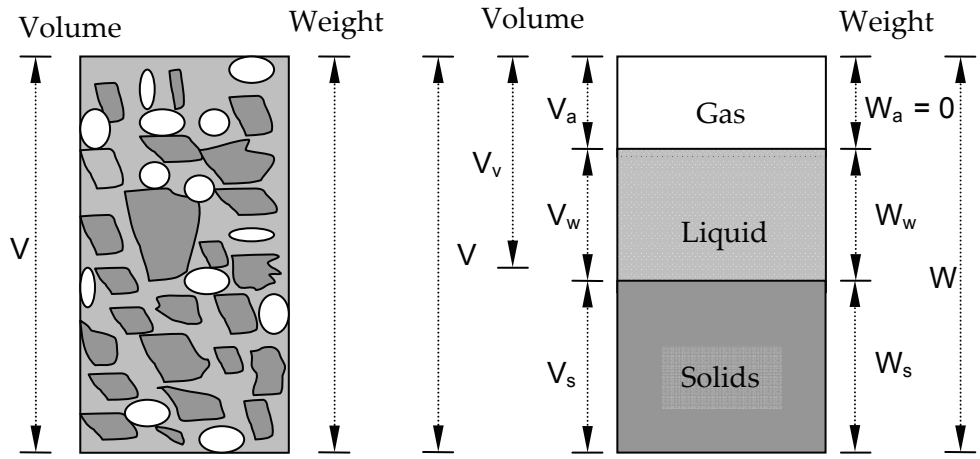

Fig. 5.1 Schematic phase diagram for natural soils

V = total volume, V_a = air volume, V_w = water volume, V_s = solid volume, W = total weight, W_a = air weight, W_w = water weight, and W_s = solid weight.

The relevant phase relationships are defined and presented under the corresponding in situ testing and laboratory investigations carried out for the case studies.

5.2 In situ testing

A few index tests were conducted by the author at the field laboratory. The purpose of conducting such tests was to identify the in situ index properties of soil samples and compare them with built-in specimens used for the permeability and triaxial tests. Moreover, the built-in specimens were based on the Standard Proctor test. Thus, the in situ index test results were directly compared with the results from those obtained in this test.

- **Density test**

A simple water-volume test was conducted to find indicative values of the in situ density of the soils. Accordingly, the loose soils on the ground surface were removed first, and the soil samples were collected from approximately 10 cm depth in a 10 cm diameter hole. Similarly, the volume of the hole was determined by filling water in a thin plastic bag. Thus, the bulk density of the soils (ρ) was determined by Eq. (5.1):

$$\rho = \frac{total\ mass\ of\ sample}{total\ volume\ of\ sampe} = \frac{m}{V} \tag{5.1}$$

- **Moisture content**

The in situ moisture content was determined by drying the sample for 24 hours, and the mass of water was thereafter determined. Thus, the moisture content (w) was computed by Eq. (5.2):

$$w = \frac{mass\ of\ water}{mass\ of\ solids} = \frac{m_w}{m_s}100\% \tag{5.2}$$

- **Dry density**

The in situ dry density (ρ_d) was obtained based on the in situ bulk density and the moisture content by Eq. (5.3):

$$\rho_d = \frac{dry\ mass\ of\ sample}{total\ volume\ of\ sample} = \frac{m_s}{V} = \frac{\rho}{1+w} \tag{5.3}$$

- **Porosity**

The in situ porosity was computed from density of soil grains (ρ_s) and the maximum in situ dry density by Eq. (5.4):

$$n = 1 - \frac{\rho_d}{\rho_s} \tag{5.4}$$

- **Unit weight**

The in situ unit weights of soils; both bulk (γ) and dry (γ_d), were computed as the product of respective density and the acceleration of gravity (g).

- **Summary of test results**

The in situ test results of the investigated four samples are presented in Table 5.1. These results are compared with the index test results obtained from the Standard Proctor test, which is presented later in this Chapter.

Table 5.1 Index test results from in situ measurements

Sample	w (%)	n (%)	γ (kN/m^3)	γ_d (kN/m^3)	S_r (%)
d1	9.5	25.5	22.0	20.0	76.0
d2	6.1	24.8	21.5	20.2	50.7
p1	6.0	32.7	19.2	18.1	33.7
p2	8.7	27.3	21.9	20.1	65.3

The in situ test results are found moderately lower than the Proctor test values. This indicates that the in situ soil is consolidated close to the Standard Proctor test at optimum moisture content level. Moreover, all the soil samples were found partially saturated in the dry season.

5.3 Laboratory testing

Four test samples (refer Table 4.1, Chapter 4) were investigated by the author at NTNU, Geotechnical Division. The main purpose of the investigations was to determine the relevant material parameters required for slope stability evaluations.

5.3.1 Index tests

The following index tests were carried out to identify and define the material characteristics. Moreover, the purpose was also to classify the soils based on their grain size distributions.

5.3.1.1 Grain size analysis

Since, all four soil samples obtained at the case study slopes contained both finer (d < 75μm) and coarser (d > 0.75μm) soil grains, both sieving and hydrometer analyses were carried out on the samples. The hydrometer analysis was imperative because the content of finer grains exceeded 5 % of the total soil sample (Kezdi 1980).

- **Sieve analysis**

According to the laboratory procedure, about 600g oven dried material was sieved through the standard sieve sizes (8 mm, 4 mm, 2 mm, 1 mm, 500 μm, 250 μm, 125 μm and 75 μm). Washing for wet sieving was carried out by using distilled water. The dry mass of the grains from individual sieving was used to find the percent passing and accordingly percent retained from the sieve size.

- **Hydrometer analysis**

A calibrated (ASTM 152H) hydrometer was used to analyse the finer grains (d < 75 μm) in the laboratory. According to the procedures, a dry soil sample was soaked in distilled water for 24 hours and mixed properly in a stirrer with a dispersive agent added to avoid flocculation of the grains. Then the suspension was poured into a 1 litre cylinder, and mixed before the soil grains were allowed to sediment in the suspension. The cylinder was placed in a constant temperature water bath during this procedure. Finally, the grain diameter was computed referring to the calibrated curves. The hydrometer analysis procedure is given in Appendix A.

- **Results of grain size analyses**

The results from both analyses were combined for all four samples as shown in Fig. 5.2. The given distribution however does not include the larger gravels and boulders present in the natural sample. These fractions were taken out from the samples at the time of transportation. However, these fractions only contributed a few percent of the total mass of the sample.

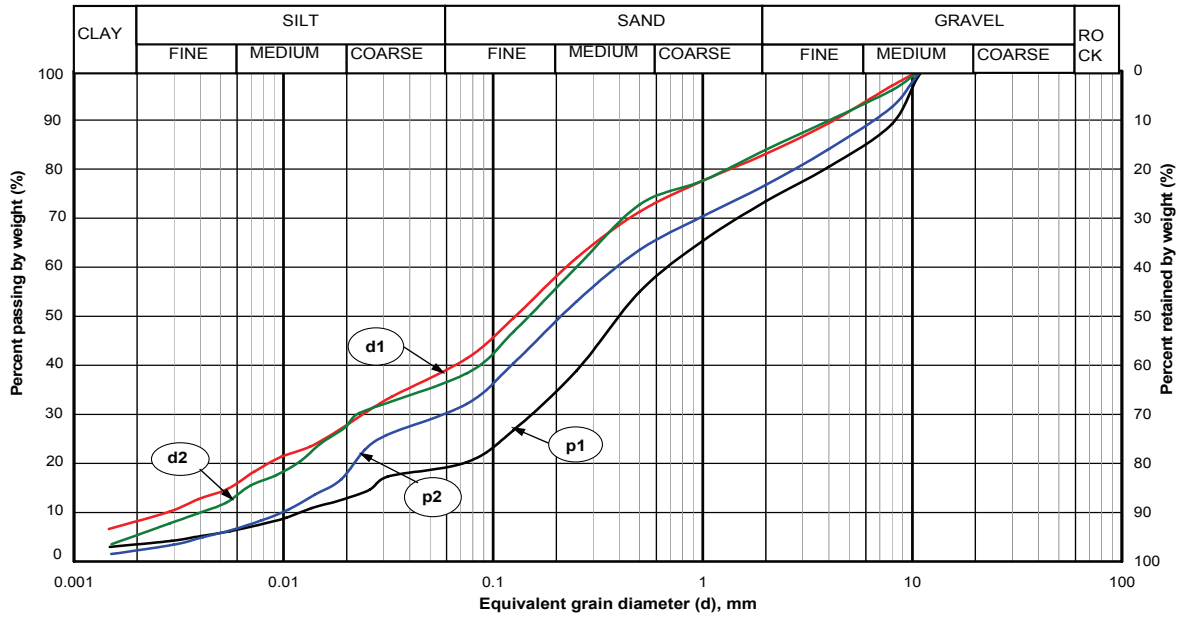

Fig. 5.2 Grain size distribution curves

- **Soil classification**

The grain size distribution curves show that the soil samples consist of all fractions ranging from medium gravel to clay. The clay content is found between 3 % and 8 % in all soil samples. However, the content of finer grains (<75 μm) are more up to 40 % in d1 and 20 % in p1. Moreover, the sand fraction, which dominates the distribution, contributes nearly 50 % of the total grains. The gravel content is the maximum in p1 (27 %) and the minimum in d1 (17 %). Similarly, the grading number ($Cu = d_{60}/d_{10}$) varies from 40 to 75 for the soil samples. Based on these parameters, all soil samples are classified as well-graded gravely, silty sand according to the Unified Soil Classification System (ASTM D2487-90 1992).

5.3.1.2 Grain density test

The density of the soil grains was determined by means of a calibrated pycnometer. The test was carried out according to the standard laboratory procedures in NTNU (NS 8012 1982). The grain density of soil sample (ρ_s) was then computed as the ratio of mass and the volume of solids as:

$$\rho_S = \frac{mass\ of\ soil\ solids}{volume\ of\ solids} = \frac{m_s}{V_s} = \frac{m_s}{(m_{pw} + m_s - m_{pt})/\rho_w} \tag{5.5}$$

where,

m_s = dry mass of the soil sample used in the pycnometer,

m_{pw} = mass of filled-up pycnometer by distilled water,

m_{pt} = mass of the pycnometer with test sample and distilled water, and

ρ_w = density of water.

5.3.1.3 Porosity limits

The purpose of investigating the porosity limits of the soil samples was to define the relative porosity of the built-in specimens for subsequent permeability and triaxial tests. The minimum and maximum porosities were determined in the laboratory by the Standard Proctor compaction tests and dry filling respectively. However, the minimum porosity was also attempted to investigate by submerged vibration procedure, which was found unsuitable for the well-graded soil samples with large fines content. The porosity (n) was obtained by:

$$n = \frac{Volume\ of\ voids}{Total\ volume} = \frac{V_v}{V} = \frac{e}{e+1} \tag{5.6}$$

Since the porosity and void ratio are related parameters, only the porosity determination is explained here. However, the procedure for laboratory investigations is the same for both parameters (Sandven 2003).

- **Minimum porosity**

The attempt made to determine the minimum porosity (n_{min}) by a wet vibration method was not suitable for the well-graded silty sand samples with fines of 20-40 %. Due to the fines, the water mixed with the soil samples was not able to drain out after the vibrations, which resulted in less compaction. However, knowing to the maximum dry density ($\rho_{d((max))}$) from the Standard Proctor tests and the density of soil grains (ρ_s) the minimum porosity limit was determined as:

$$n_{\min} = 1 - \frac{\rho_{d(\max)}}{\rho_S} \tag{5.7}$$

Nevertheless, for verification purposes, the wet vibration method was carried out for the d2 sample according to the utilised laboratory procedure. As a result, the minimum porosity of 39.1% was obtained. This value was found much higher than the minimum porosity of 23.4%

obtained from the Standard Proctor test. Therefore, the values from the Standard Proctor test were considered representative to the minimum porosity, which was found close to the in situ minimum porosity of the tested soils (see Table 5.2).

- **Maximum porosity**

As said above, the maximum porosity (n_{max}) was determined by dry filling method. Accordingly, dry grains of the soil were dropped gently through a funnel, avoiding free fall of the grains. The cylinder was completely filled and the dry soil mass (M_s) was obtained. Thus, the volume of voids ($V_v = V - V_s$) was computed from the known volume (V) of the cylinder and the computed volume of dry soil ($V_s = M_s/\rho_s$). Thus, the n_{max} for the materials was calculated as:

$$n_{\max} = \frac{V_v}{V} 100\% \tag{5.8}$$

5.3.1.4 Relative porosity

The relative porosity (P_r) was used to relate the porosity values of the built-in specimens to the obtained porosity limits. Instead of the relative density (D_r), mostly used for sands, the relative porosity was considered. The relative porosity was computed by:

$$P_r = \frac{n - n_{\min}}{n_{\max} - n_{\min}} * 100\% \tag{5.9}$$

The relative density is accordingly given by:

$$D_r = \frac{e_{\max} - e}{e_{\max} - e_{\min}} * 100\% \tag{5.10}$$

The built-in specimens for permeability and triaxial tests are classified according to the relative porosity. The classification of specimens based on the relative porosity is given in Appendix C.

5.3.1.5 Results of index tests

The index parameters obtained from the in situ and laboratory tests are summarised in Table 5.2 for the different soils. The in situ tests were carried out in during the second visit to the project.

Table 5.2 Soil index parameters

Sample	In situ test			Standard Proctor test				Grain	Porosity	
	w (%)	γ_d (kN/m^3)	n (%)	OMC (%)	γ_d (kN/m^3)	$n_{\min}$ (%)	S_r (%)	density ρ_s (g/cm^3)	$n_{\max}$ (%)	P_r (%)
d1	9.5	20.0	25.5	8.5	20.6	23.4	76.2	2.74	49.2	8.1
d2	6.1	20.2	24.8	8.5	20.6	23.4	76.2	2.74	47.6	5.8
p1	6.0	18.1	32.7	12.5	18.6	30.4	78.1	2.73	55.4	9.2
p2	8.7	20.1	27.3	7.5	21.3	23.1	70.4	2.82	42.8	21.3

The in situ index parameters were found quite close to the values obtained from the Standard Proctor test, although the in situ density test was carried out by an approximation method. The given P_r values are based the in situ porosity, which indicates the dense soils in the field.

5.3.2 Mineralogical identification

Minerals influence the physical and chemical properties of soil grains, including the size and shape. The purpose of the test was to identify the mineral contents present in the soil samples. As a result, identification was conducted for three soil samples (d1, p1 and p2) at NTNU, Rock and Mineral Testing Laboratory, using an X-ray diffraction method. The method is based on Bragg's law (Perkins 1998):

$$n\lambda = 2d\sin\theta \tag{5.11}$$

where,

n = number of wave length (counts),

λ = wave length,

d = distance between the refraction planes (A^0), and

θ = diffraction angle.

According to Perkins (1998), the intensity of the strongest peak was assigned to 100% and reference data sets were used to identify the presence of minerals. The tests were conducted by a mineralogist in the presence of the author. The recorded data were interpreted to identify the presence of various types of minerals. Fig. 5.3 shows the measured peaks as the relationship between the counts (0-100 %) and angle 2θ (0- 60^0) for the p2 sample. The counts represent the relative intensities compared to the strongest (reference) intensity.

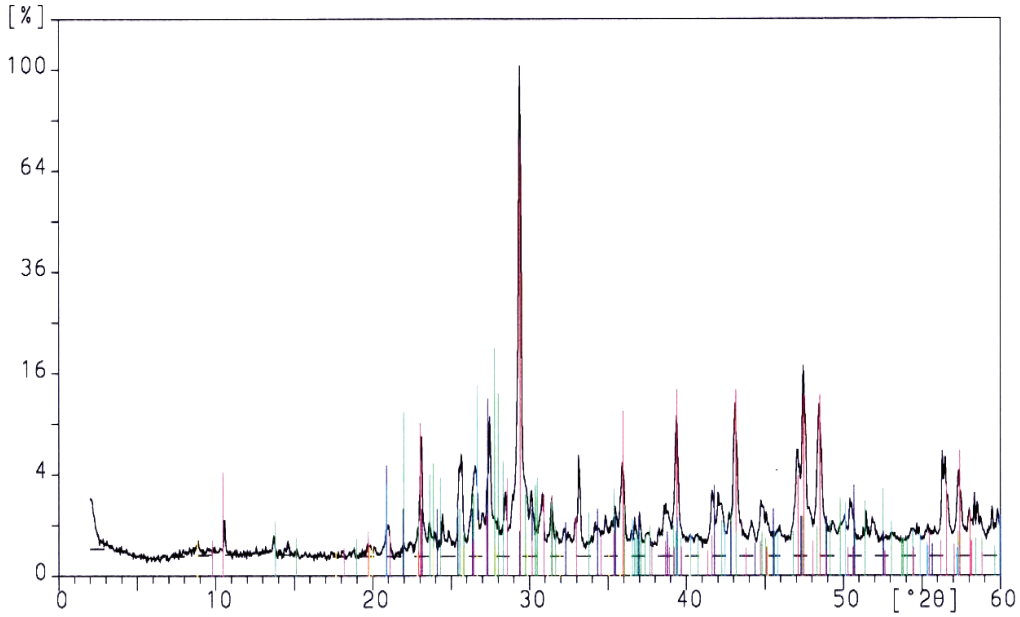

Fig. 5.3 Relative intensity, counts (%) and angle (2θ) for sample p2

For the test, powdered samples were prepared by hand grinding and were placed inside the diffraction apparatus, which measured the peak intensities and diffraction angles (2θ).

5.3.2.1 Test results

The minerals identified for three soil samples are presented in Table 5.3. Calcite, potassium-feldspar and plagioclase were found in dominant presence in the slope materials. Other minerals, for example quartz and mica were seen to a very small extent.

Table 5.3 Mineral compositions in %

Sample	Calcite	Plagioclase	K-feldspar	Quartz	Mica
d1	26	1	40	12	3
p1	2	56	28	12	1
p2	81	0	15	2	1

The dominating presence of calcite ($CaCO_3$) was found in the p2 sample, which was collected from the glacial deposit in the area of the powerhouse slope. The calcite must originate from various sources, for example limestone, chalk, dolostone and marble (Wenk & Bulakh 2003, Mitchell 1993). According to Hurlbut and Sharp (1998), calcite is found in nature more than any other mineral. It absorbs water and transmits faster than other minerals. Despite the similar grains and index properties, p2 sample was found more permeable than others (see Fig. 5.5).

5.3.2.2 Some properties of calcite

Calcite disintegrates and produces calcium hydroxide and carbon dioxide when it is exposed to rainwater. Moreover, the rainwater is also a part of acid water, which is very active in chemical reactions (Skinner & Porter 2000) as:

$$CaCO_3 + H_2O \Rightarrow Ca(OH)_2 + CO_2 \quad (5.12)$$

(calcite) (water) (calcium hydroxide) (carbon dioxide)

Rainwater and carbon dioxide again produce carbonic acid (H_2CO_3) which further reacts with calcite and dissolution process of calcite continues as:

$$H_2O + CO_2 \Rightarrow H_2CO_3 \quad (5.13)$$

(carbon dioxide) (carbonic acid)

$$CaCO_3 + H_2CO_3 \Rightarrow Ca^{2+} + 2(HCO_3)^- \quad (5.14)$$

(calcite) (carbonic acid) (calcium ion) (bicarbonate ion)

The above chemical reactions show that the dissolution of calcite mineral is proactive in the presence of water. Moreover, the soils containing calcite are susceptible to erosion. In the dissolution process, formation of piping, caverns, sinkholes and other features are consequently

developed as the major engineering challenges (Goodman 1993). Therefore, a calcite-dominated area should be protected against infiltration of water and any other forms of acid solutions.

The rest of the identified minerals (see Table 5.3) pose no significant problem in stability of slopes, and hence their properties are excluded from further discussions.

5.3.3 Compaction and permeability tests

5.3.3.1 Standard Proctor test

The Standard Proctor test was carried out to determine the maximum dry density, optimum moisture content (OMC) and minimum porosity of the materials. Since all soil samples were less than 4.0 kg, only grains passing the 8 mm sieve were used in one litre cylinder test according to the standard (Statens Vegvesen 1997). The bulk density (ρ) of the soil samples was computed from the known volume of the Proctor cylinder and the following relationship was used to compute the dry density (ρ_d):

$$\rho_d = \frac{\rho}{(1+w)} \tag{5.15}$$

Fig. 5.4 shows the test results plotted as the dry density versus the moisture content. The OMC refers to maximum dry density obtained at the peak of the smoothed curve. Two saturation lines (S_r = 80%): One for the d1, d2 and p1 samples (lower line) and another for the p2 sample (upper line) are also plotted in Fig. 5.4.

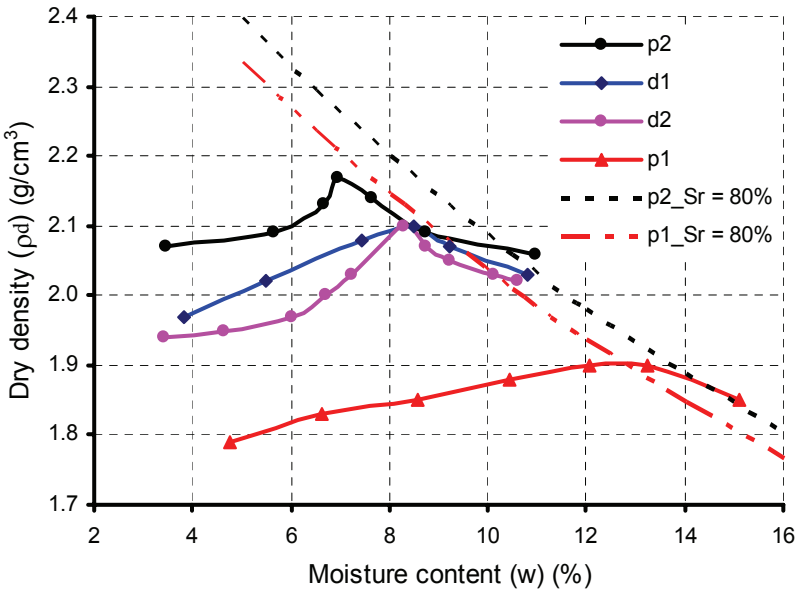

Fig. 5.4 Dry density and moisture content of samples

The saturation line depends on the grain density (ρ_s) and degree of saturation (S_r) as:

$$\rho_d = \frac{\rho_w G_s}{1+w(G_s/S_r)} \tag{5.16}$$

where,

$$G_s = \frac{\rho_s}{\rho_w}\ ,\ S_r = \frac{wG_s}{e} \quad and\ e = \frac{\rho_s}{\rho_d} - 1 \tag{5.17}$$

The maximum dry density ($\gamma_{d(max)}$), OMC and the n_{min} from the Standard Proctor test were taken as the recommended values for built-in permeability and triaxial test specimens in the laboratory. The results from the Standard Proctor test were selected because of the similar index properties found in the site laboratory tests (see Table 5.2) and consolidated soils.

5.3.3.2 Permeability test

Permeability tests were carried out based on the laboratory procedure established by NTNU, Geotechnical Division for fine-grained materials (Sandven & Svaan 1993). The purpose of the test was to determine the permeability coefficient as an input parameter in PLAXIS simulations for groundwater flow and subsequent slope stability analyses. The following relationship, based on Darcy's law and continuity equation, was used to find the permeability coefficient (k) as:

$$k = \frac{Ql}{Ath} \tag{5.18}$$

where,

Q = water volume (cm^3),

l = sample length (cm),

A = cross sectional area of the sample (cm^2),

t = time required for specific water flow (s), and

h = difference in potential head (cm).

An air pressure controlled apparatus was used to conduct the permeability tests. Details of the test procedures and test apparatus are given in Appendix A, Section A.2. Both the coefficient of permeability versus the relative porosity, and the corresponding dry density of the tested specimens, are presented in Fig. 5.5.

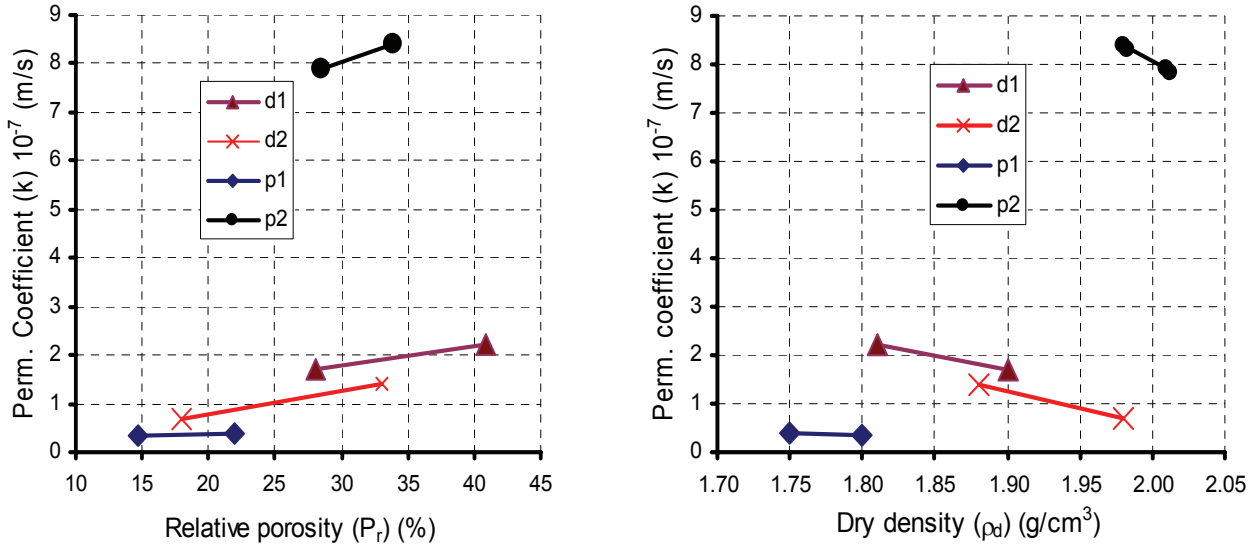

Fig. 5.5 Coefficient of permeability for tested specimens

The test samples were built-in in a controlled way in the laboratory to assure homogeneous conditions for the specimen. An under-compaction method, which is described in Appendix B, was adopted for the purpose. The index parameters of the built-in specimens are given in Appendix C.

The coefficient of permeability of the three samples was showing a gentle variation for an increased relative porosity. However, the permeability in general may be affected also by other parameters. As Sandven (2003) states, "The permeability coefficient mainly depends on the size and shape of the soil grains and the degree of compaction, i.e. density of the soil". Moreover, this study shows that the permeability may also be affected by the presence of calcite mineral.

The p2 soil sample with 81% calcite mineral (see Table 5.3) was found much more permeable than other soil samples, despite a similar relative porosity (P_r) and higher dry density (ρ_d). No significant variation in finer grains (see Fig. 5.2) was found in the soil. Repeated results were found in a verification study, performing additional permeability test on this particular material. Moreover, plastic flow behaviour was observed around a moisture content of 15 % for this material.

5.3.3.3 Compression test

The compression properties of the soils were investigated by the oedometer test. The purpose of the test was to observe the stress-strain properties of the silty sand and determine the oedometer modulus (E_{oed}) as an input to the FE analyses (PLAXIS). However, this is a useful parameter for settlement calculations. The oedometer test is based on one-dimensional consolidation theory, and is the most common way to determine the stiffness of soils in the laboratory (Janbu 1963, Sandven 1992). The testing apparatus has been presented in Appendix A, Fig. A.2. The test samples were built-in in the laboratory and assured to have homogeneous density throughout the specimen. The dimensions of the specimen were 3 cm height and 50 cm^2 cross sectional area. The detailed specimen built-in procedures are given in Appendix B.

- **Test procedure**

The built-in specimens were tested in a floating-ring oedometer with an incremental loading procedure. An incrementally increased vertical stress, starting at 78 kPa and ending at 706 kPa was applied and deformation with time was recorded. After completing the test, the eigendeformations of the system (filter, top cap, etc) was measured for the same equipment components and loading steps as applied for the soil test. Test data were recorded automatically and the test records used to deduce the deformation parameters of the soil.

- **Test results**

The recorded soil deformation data were analysed for oedometer modulus, and the test results for p2 and d2 materials are given in Fig. 5.6. Both materials were tested at two different build-in porosities.

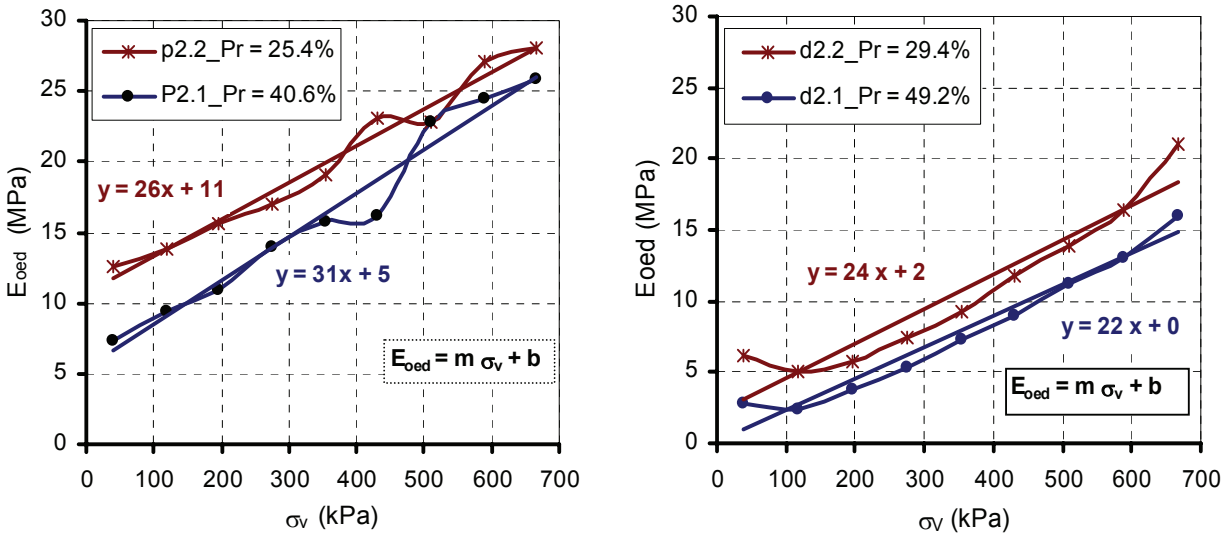

Fig. 5.6 Oedometer modulus for p2 and d2 materials

From the best-fit line, a relationship between the oedometer modulus (E_{oed}) and the modulus number (m) was established as a function of the vertical stress (σ_v). The modulus number was found higher than 20 (see Fig. 5.6). This represents similar property as stiff clayey soils (Janbu 1963, Sandven 2002). The E_{oed} depends on parameters like vertical stress, porosity and degree of saturation or moisture content (Emdal 1994, Janbu 1970, 1963). The relative porosity for each test has also been indicated in Fig. 5.6 and the specimens were built-in at the respective OMC level. The materials p1 and d1 showed almost identical results as obtained for the d2 material.

The E_{oed} obtained from these tests can be considered as a guideline for selection of input parameters for the PLAXIS calculations. Compared to the triaxial modulus (E_{50}), the E_{oed} was found to be low. For example, the E_{oed} at σ_v =100 kPa was found to be 13 MPa for the p2.2 specimen (P_r = 25.4 % in Fig. 5.6). However, for the p2.4 specimen in triaxial test, the value of E_{50} was obtained around 30 MPa, which could be found in the oedometer test at σ_v =700 kPa (see Fig. 5.6). Similar differences were also obtained for d2.2 specimen. The reason of almost double difference can be explained partly due to the differences in relative porosities (see Table 5.2) and moisture contents (refer Appendix C, Tables C.5 and C.7) and the completely different loading stress pattern. Therefore, the latter (E_{50}) was selected in PLAXIS simulations, considering the stiffer soils due to over consolidation and low relative porosity as in natural conditions.

5.3.4 Triaxial tests

The main purpose of conducting triaxial tests was to investigate shear strength parameters for the stability analyses. In the triaxial test, the natural effective stress conditions can be simulated to obtain relevant strength characteristics of the soil. The triaxial test specimen is surrounded by a waterproof membrane inside a pressurised chamber, which enables pore pressure inside the sample to be measured during the test. Moreover, a specimen can be consolidated for an anisotropic stress ($\sigma_1 > \sigma_2 > \sigma_3$), or in an isotropic stress ($\sigma_1 = \sigma_2 = \sigma_3$) conditions (Coduto 1999).

Total 24 specimens were investigated both consolidated undrained (CU) and consolidated drained (CD) conditions. These abbreviated terms are referred by U and D in the later expressions. Table 5.4 shows the conducted tests in this study. Three tests of one type of soil were conducted at three different stress levels to define precisely the Mohr-Coulomb failure envelope.

Table 5.4 Summary of conducted triaxial tests

Sample	p1		p2		d1		d2	
Test types	U	D	U	D	U	D	U	D
Symbols	p1.1	p1.4	p2.1	p2.4	d1.1	d1.4	d2.1	d2.4
	p1.2	p1.5	p2.2	p2.5	d1.2	d1.5	d2.2	d2.5
	p1.3	p1.6	p2.3	p2.6	d1.3	d1.6	d2.3	d2.6

The aim of carrying out both U and D tests was to investigate the difference in shear strength parameters, and use them accordingly for various situations in the stability analyses. For example, undrained conditions may be related to earthquakes events and the corresponding undrained strength parameters are hence more relevant in the analyses.

The principle difference between U and D test was related to the mode of shearing and the pore pressures developed. The dissipation of pore pressure during shearing was not allowed in U tests, whereas drainage was permitted in D tests. Moreover, higher strain rate in U tests (2 %/hr) and lower in D tests (0.5 %/hr) were applied. The slower strain rate in the D tests was selected to allow sufficient time to dissipate pore water from the specimen during shearing. The applied strain rates were checked according to the relationship stated by Kezdi (1980) and found in the recommended limit. The test procedures are otherwise the same for both tests. The built-in procedure of specimens, which is described in Appendix B, Section B.1 aimed at obtaining the targeted and consistent porosity. The obtained index parameters at three stages (building, consolidation and failure) of the specimens have been given in Tables C.4 - C.7 in Appendix C.

5.3.4.1 Triaxial test equipment

The triaxial test equipment used in this study is shown in Fig. 5.7. In this equipment, both isotropically and anisotropically consolidated U and D tests can be performed in static condition, where the test procedures can be controlled directly by a closed-loop computer program. Axial displacement, load cell and pressure transducers are used to record the test results. The pore pressure is recorded at bottom of the specimen. The load cell, which is attached to the load frame, records the vertical applied force (P) on the specimen.

Components of equipment:

1: Triaxial cell,

2: PC for data logging and test control,

3: Load frame controller,

4: Cell pressure supply,

5: Cell pressure and back pressure control units,

6: Burette for saturation and volume change measurements

7: Axial displacement, and

8: Load frame with load cell.

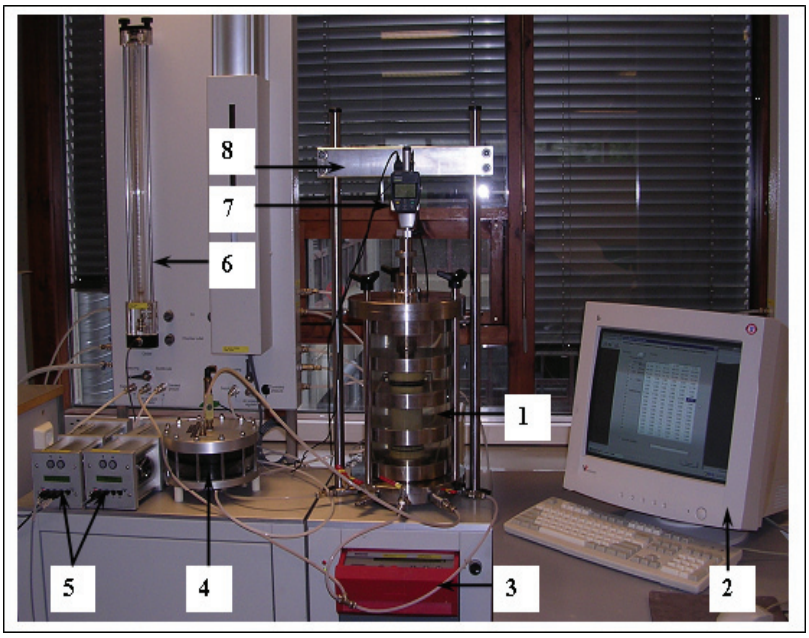

Fig. 5.7 Components of the utilised triaxial equipment

5.3.4.2 Test procedures

The testing procedure involves three main operations: Saturation, consolidation and shearing. The installation and saturation procedures are explained in details in Appendix A, Section A.4.

- **Saturation control**

The saturation of the specimen was carried out in two steps by using back-pressures up to 800 kPa. A further increase in back pressure was not possible due to the limiting capacity (1 MPa) of the equipment. However, the saturation condition was checked by conducting B-test based on the change in pore and cell pressures as:

$$B = \frac{\Delta u}{\Delta \sigma_c} = \frac{u - u_o}{\sigma_c - \sigma_{oc}} \tag{5.19}$$

where,

$\Delta u = u - u_o$ = change in pore pressure, and

$\Delta \sigma_c = \sigma_c - \sigma_{oc}$ = change in cell pressure.

The B-value depends on the porosity of the soil, the compressibility of the pore water and soil structure (Bishop & Henkel 1962, Head 1985), as is given by:

$$B = \frac{1}{(1 + n\frac{C_w}{C_s})} \tag{5.20}$$

where, n = porosity of soil, and

C_w , C_s = compressibility of porewater and soil structures respectively.

Chaney and Mulilis (1978) states: "The B-value will be close to unity for smaller values of C_w than C_s and less porous soils. For stiff soils, lower values could be obtained even in fully saturated condition". The recorded values during the tests with the applied back-pressure are given in Appendix C, Tables C.4 - C.7. The obtained values range between 0.80 and 0.97. A higher B-value was hard to achieve for the specimens of well-graded composition. In earlier studies (not by the author), the use of CO_2 was tried without satisfactory results. The minimum B-value for a classified saturated response should normally be 0.96, and a back-pressure as high as 1500 kPa may be required for a specimen with 70% initial degree of saturation (Head 1989). The degree of saturation at built-in of specimens ranges from 50 - 80% as given in Appendix C, Tables C.4 - C.7.

- **Consolidation and shearing**

The procedures used for consolidation and shearing of specimens are elaborated in Appendix A, Section A.4. The failure pattern of undrained and drained shearing for p2 specimen has been compared in Fig. 5.8. The failure in undrained shearing was found very brittle (see also Fig. 5.13). Moreover, significant strain softening at low axial strain level (<1%) was also observed beyond the peak strength compared to the specimens from the other soils.

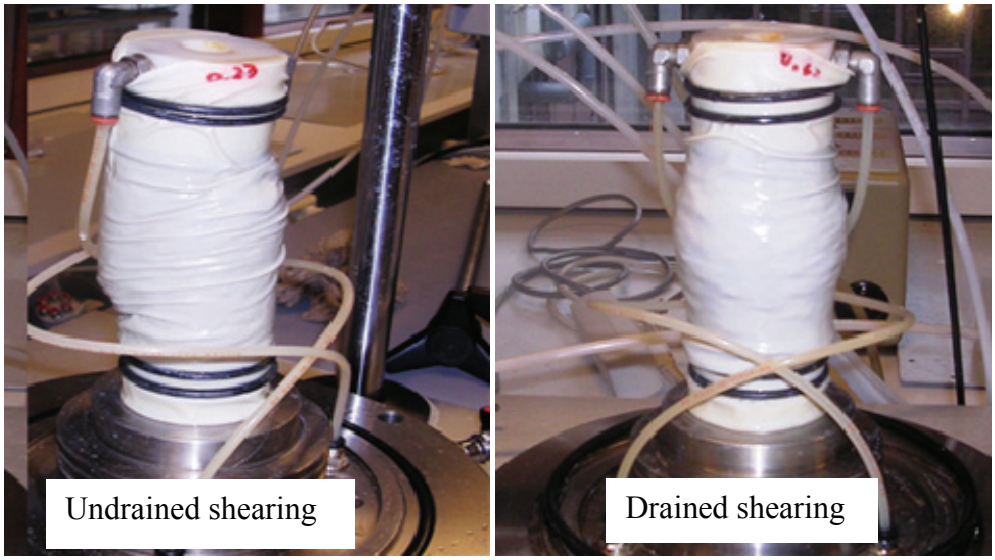

Fig. 5.8 Shape of the specimen after shearing in U and D tests

A strain control approach was used to shear the specimens. As mentioned before, two different strain rates were used in the U and D tests. The specimens were sheared at three different consolidation stress levels (100, 150 and 200 kPa) to define precisely the Mohr-Coulomb failure envelope over a larger, relevant stress range for determination of the shear strength parameters.

5.3.4.3 Axial and radial stresses

The automatically recorded data were analysed separately for axial and radial effective stresses. The computations have been given as an example in Appendix C, Table C.8. The effective axial stress (σ_a') and the radial stress (σ_r') were computed using the following relationship:

$$\sigma_a' = \frac{P}{A_d} + \sigma_c - u_b \quad \text{and} \quad \sigma_r' = \sigma_c - u_b \tag{5.21}$$

where,

P = vertical load recorded by load transducer,

A_d = corrected specimen area for drained test and A_u for undrained test,

σ_c = applied cell pressure measured by pressure transducer, and

u_b = applied back pressure measured by pressure transducer.

In order to compute actual stresses applied in the specimen, the initial reading of the vertical load (P) was first set to zero at the start of shearing. However, a small effective stress (<5 kPa), which was computed considering the weight above the middle of the specimen, was not recorded by the load cell. In fact, this unrecorded stress should have been added to the initial readings. However, a little friction in the piston cannot be ignored even after its lubrication, and thus the unrecorded small stress was neglected assuming that the friction can compensate it.

Moreover, the specimen area changes due to volume change during consolidation, and due to compression during shearing. Thus, the original (built-in) area was corrected manually for both the change in cross sectional area and the constraining effect of the rubber membrane. The correction procedures are presented in Appendix D. In this way, the corrected axial and radial stresses acting on the specimen were used to determine the shear strength parameters.

5.3.4.4 Shear strength parameters

The effective shear strength parameters (c′, ϕ′) are determined from the p′ - q relationship. However, these parameters can also be determined either by σ_3' - τ (NTNU) or σ_{av}' - τ (NGI, MIT) plot. The relationships of the symbols p′, q and σ_{av}' are given in Appendix D, Section D.3.

The latter plot was used in the previous triaxial tests given in Chapter 4, Section 4.8.2.2. The Mohr-Coulomb failure envelope in the plots is defined by a tangent line drawn at three extreme deviatoric or shear stress levels. The p′- q and σ_3' - τ plots are illustrated in Fig. 5.9 and the related expression for the slope is given in Table 5.5.

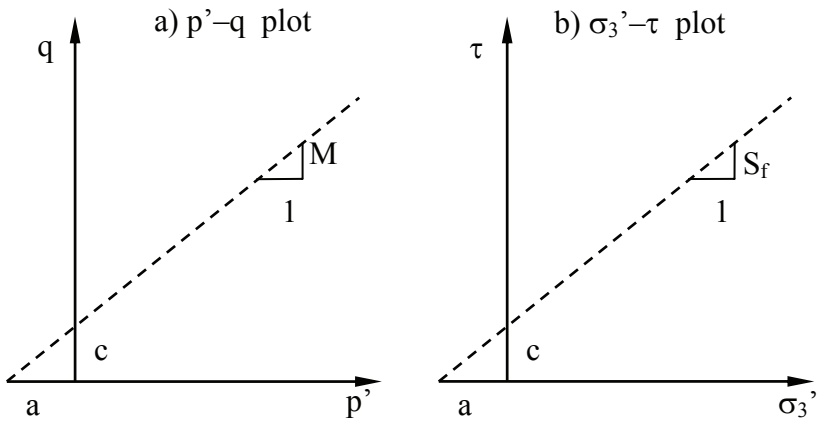

Fig. 5.9 Determination of shear strength parameters

Table 5.5 Friction angle related to different plots

Plots	p'- q	σ_3' - τ	σ_{av}' - τ
Slope	M = 6sinϕ/(3-sinϕ)	S_f= sinϕ/(1-sinϕ)	sinϕ

5.3.4.5 Triaxial test results

The triaxial test results are presented together with p' – q and ε_1 – q diagrams. Similarly, the results from both U and D tests for one sample are plotted in the same diagram. The shear strength parameters are found from the first diagram, where the stress paths are also shown. The second diagram in the same figure is used to compare the axial strains developed during the tests. To exemplify, the diagrams for the d1 sample are given in Fig. 5.10.

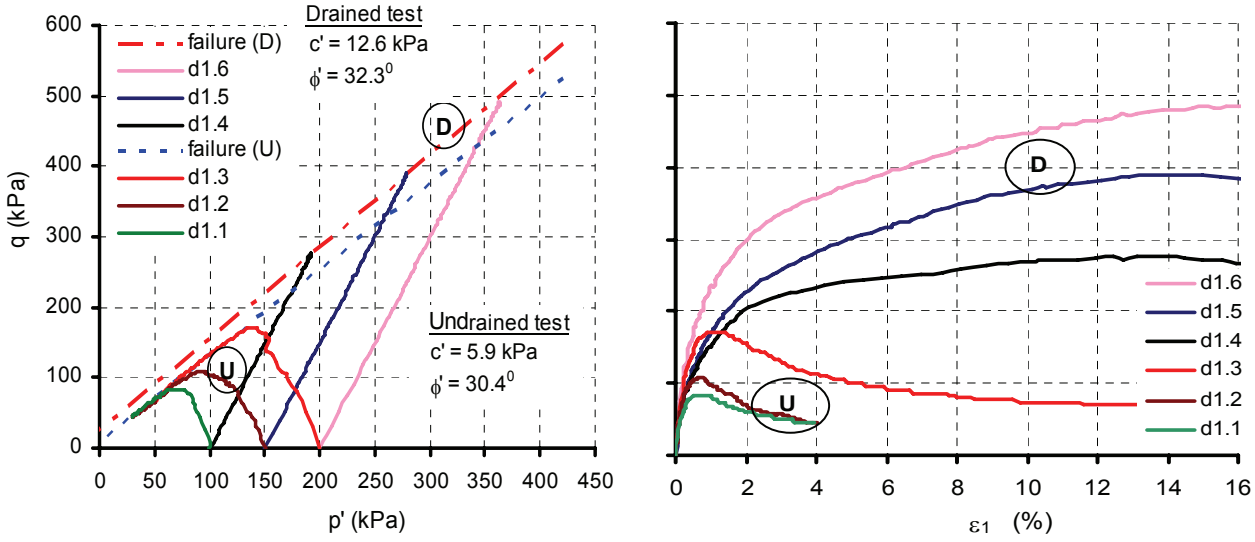

Fig. 5.10 Triaxial tests results for the d1 soil sample (p' – q and ε_1 – q diagrams)

Similar diagrams for the d2 samples are given in Fig. 5.11. The shear strength parameters in the U test are found slightly lower than in the D tests. Similarly, marginal differences in strength parameters were found in D tests for the d1 and d2 samples. The test results show that both samples have contractive behaviour. However, these soils can be expected to be overconsolidated in the natural conditions, referring to Chapter 6, Section 6.1.1.

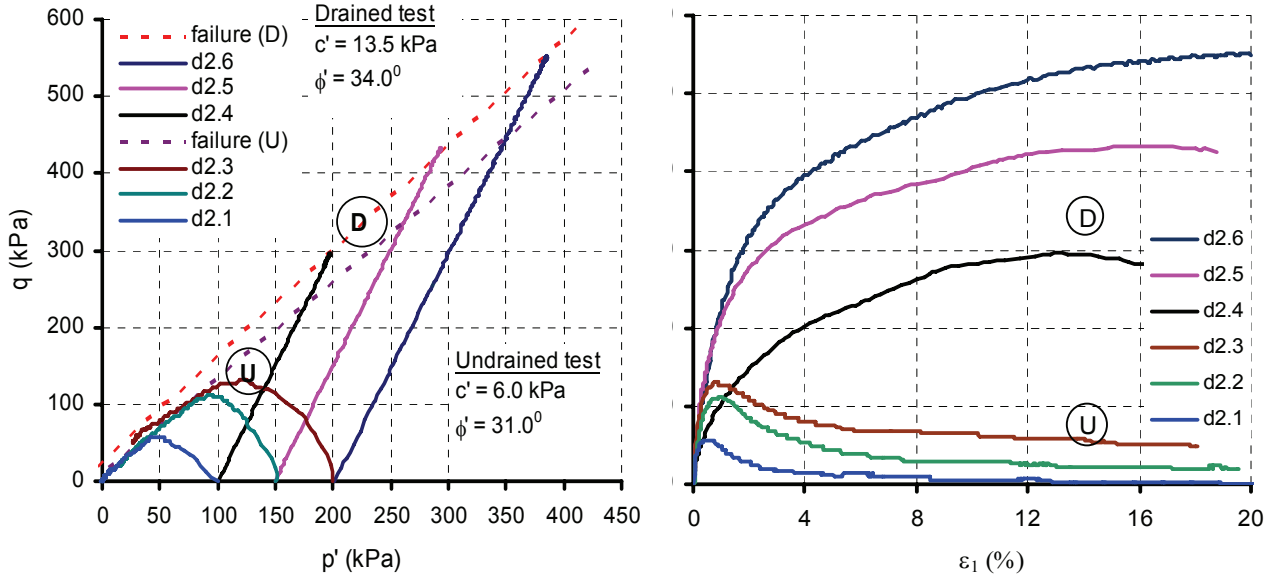

Fig. 5.11 Triaxial tests results for the d2 soil sample (p′ – q and ε_1 – q diagrams)

Fig. 5.12 shows the effective stress paths and strength parameters for the soil sample p1 taken from the powerhouse slope. This material originated from alluvial deposits. The previous triaxial test results (NGI 2001) are also plotted in Fig. 5.12 and shown by the thinner lines.

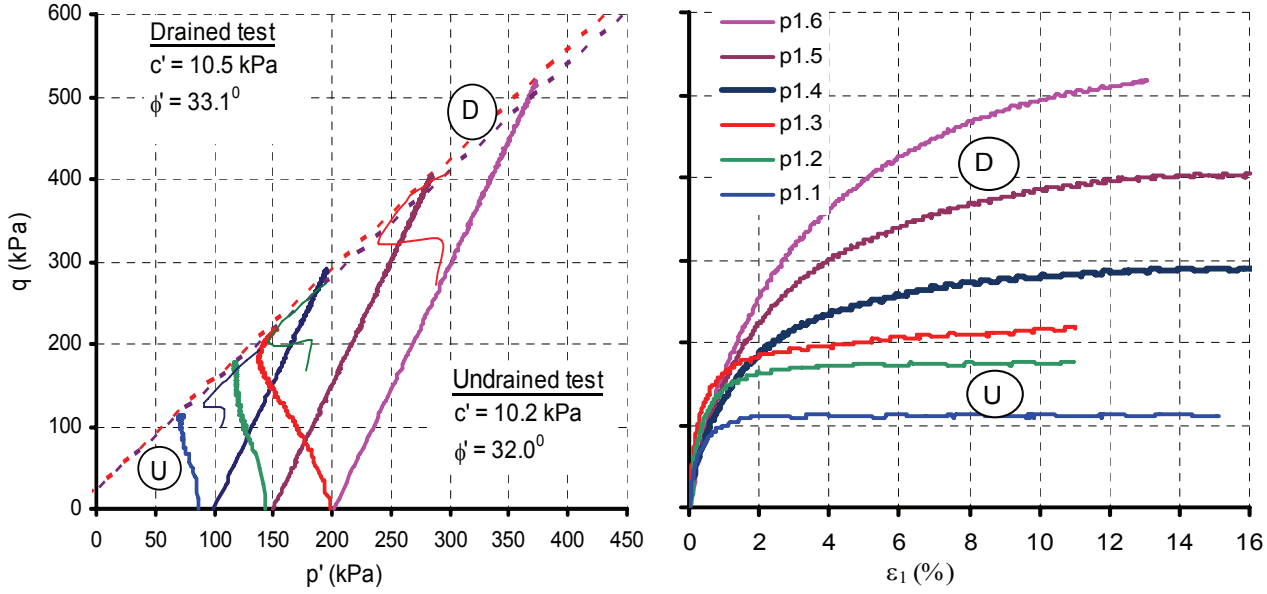

Fig. 5.12 Triaxial tests results for the p1 soil sample (p′ – q and ε_1 – q diagrams)

As seen from Fig. 5.12, the previous test results for the alluvially deposited soils show a good agreement with the present test results. However, the previous tests on the mudflow (see Fig. 4.8 in Chapter 4) show higher strength parameters compared to the results for d1 and d2 samples.

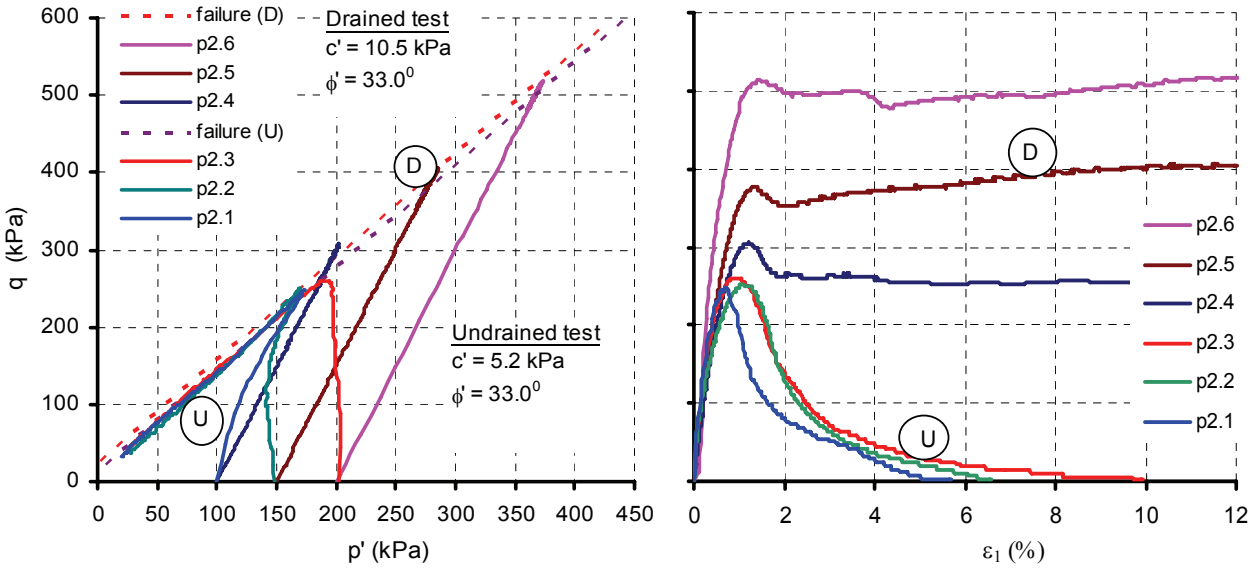

Fig. 5.13 Triaxial tests results for the p2 soil sample (p′ – q and ε_1 – q diagrams)

Finally, Fig. 5.13 represents the soil from the lower terrace of the powerhouse slope. This soil contains 81% calcite and shows different behaviour compared to the rest of the samples. The observed failure pattern was not only found brittle, but also the material showed shear strength unaffected by the increasing mean stress (p′) in U tests (see Fig. 5.13). Unlike the other materials, strain-softening behaviour at low strain levels (<1%) was found in U tests (see also Fig. 5.8). This indicates that the dominating presence of calcite has significant influence on the soil properties.

5.3.4.6 Summary of triaxial test results

The shear strength parameters obtained from the triaxial tests are summarised in Table 5.6. The c′ and ϕ′ are the curve fitting parameters and hence have found moderate variations in U and D tests except for the p1 soil sample.

Table 5.6 Shear strength parameters from triaxial tests

Samples	Test	c′ (kPa)	ϕ′ (^{0})	ε_f (%)	E_{50} (MPa)	Test	c′ (kPa)	ϕ′ (^{0})	E_{50} (MPa)	εf (%)
d1	U	5.9	30.4	0.7 - 1.0	30	D	12.6	32.3	15	15
d2		6.0	31.0	0.6 – 1.0	30		13.5	34.0	15	15
p1		10.2	32.0	3.0 - 4.5	25		10.5	33.1	15	15
p2		5.2	33.0	0.7 - 1.0	50		10.5	33.0	30	12

The triaxial test results showed that the peak strength occurs at around 1–2% axial strain in the U tests. However, in the D test, the peak strength occurs at much higher strains, more likely to 12-15%, where the M-line denoted by D has been drawn. In p2 soil sample, the failure was seen brittle and the soil became more plastic around 15% moisture content. Moreover, a strain softening behaviour was observed after 1% strain and the soil gradually looses the shear strength around 5% strains in the U tests (see Fig. 5.13). However, the D tests showed somewhat more stable behaviour, where the peak strength was retained with the increasing axial strain. As given in Table 5.6, the stiffness modulus (E_{50}) was found higher in U tests compared to D tests.

5.4 Selection of strength parameters

The effective stress parameters (c′, ϕ′) from U and D tests are not identical. The U test shows slightly lower values than in the D test, particularly with respect to the cohesion. The strength in the D tests has been taken at a higher axial strain level. However, if the maximum axial strain is limited to 5% in the D tests, nearly the same strength parameters as in U tests can be traced. The difference in applied strain rates in two different (U and D) tests does not explain the difference in strength parameters for the investigated silty sand materials. According to Leroueil and Hight (2003), the effect of strain rate is negligible for cohesionless materials. However, for natural clays, the undrained shear strength decreases by 10% for decreasing strain rates by unit log scale. The reason is that the pore pressure increases as the strain rate decreases in undrained test.

Head (1985) states, "the difference in the effective strength parameters is due to the two different nature of the test". He further explains, 'the sample volume changes in the D test during shearing, and if the material dilates at failure, it gives an increase in the measured strength as the contribution of the dilatancy. The opposite applies to a soil which contracts at failure. However, the two approaches can be treated as equal in many applications'. In this study, all tested specimens except the p1 sample (see Fig. 5.10 - 5.13) showed contacting behaviour, but contrarily to the expression above, the D tests show slightly higher strength. At the same time, a little dilating p1 sample (see Fig. 5.12) has almost the same parameters in both tests. Moreover, the p2 sample has same friction angle in both tests, but a lower cohesion is found in the U test.

Considering several factors, the strength parameters investigated from the D tests were selected for the stability evaluations. One of the reasons was the slightly higher relative porosity of the built-in specimens. Since the recommended saturation levels of the densely compacted specimens for well-graded silty sand were not possible to achieve, the specimens were built-in at slightly higher porosity level than the in situ porosity (refer Appendix C, Tables C.4 – C.7). It means, the built-in specimens were medium dense to dense, which may have resulted in the conservative parameters. However, over the shearing in D tests, the porosity was found close to the in situ level, which was considered as the basis for selection. Moreover, removal of several metres of top soils from the slopes has resulted in over consolidation, which is later discussed in Chapter 6. This was another reason for selecting the strength parameters from D test.

Chapter 6

Stability Evaluations of Case Study

6.1 Description of case study project

The Middle Marsyangdi Hydroelectric Project (MMHEP) in Nepal, located on the middle reach of the Marsyangdi River, was designed as a run-of-river plant with an upstream daily storage for 1.6 million m^3 of water. The project is under construction since 2001 and is expected to be completed in 2007. The power plant with 76 MW installed capacity aims to generate an average annual energy of 470 GWh (CES 2005). A concrete gravity dam with spillway facilities, underground desilting caverns, a concrete lined tunnel and a semi-underground powerhouse are some of the important structures in the project. The waterway facilities were designed for 120 m gross head and 80 m^3/s water flow for the power production (Fichtner 2001, CES 2005).

There are high natural slopes in the projects, mainly at the dam site left bank and in the powerhouse area. The previous analyses and design of the slopes were based on geotechnical investigations carried out during the detailed design stage of the project (Fichtner 2001).

The dam site left bank slope and the powerhouse permanent slope were selected as case studies for stability evaluations through parameter studies. These slopes were chosen not only due to the importance of the project structures, but the availability of groundwater measurements and other relevant parameters required for the academic research in the real cases. The collected data for the case studies are given in Chapter 4. Similarly, results from laboratory investigations conducted on four soil samples taken from the slopes, are presented in Chapter 5.

6.1.1 Dam site left bank slope

Fig. 6.1 shows the view of the dam site left bank slope, which was taken at the second visit in 2004. The designed, re-shaped and vegetated slope view from the first visit is shown in Chapter 4, indicating the locations of piezometers and pressure relief wells. In addition, surface and sub-surface drainage systems, which were installed in the slope, are also described in Chapter 4.

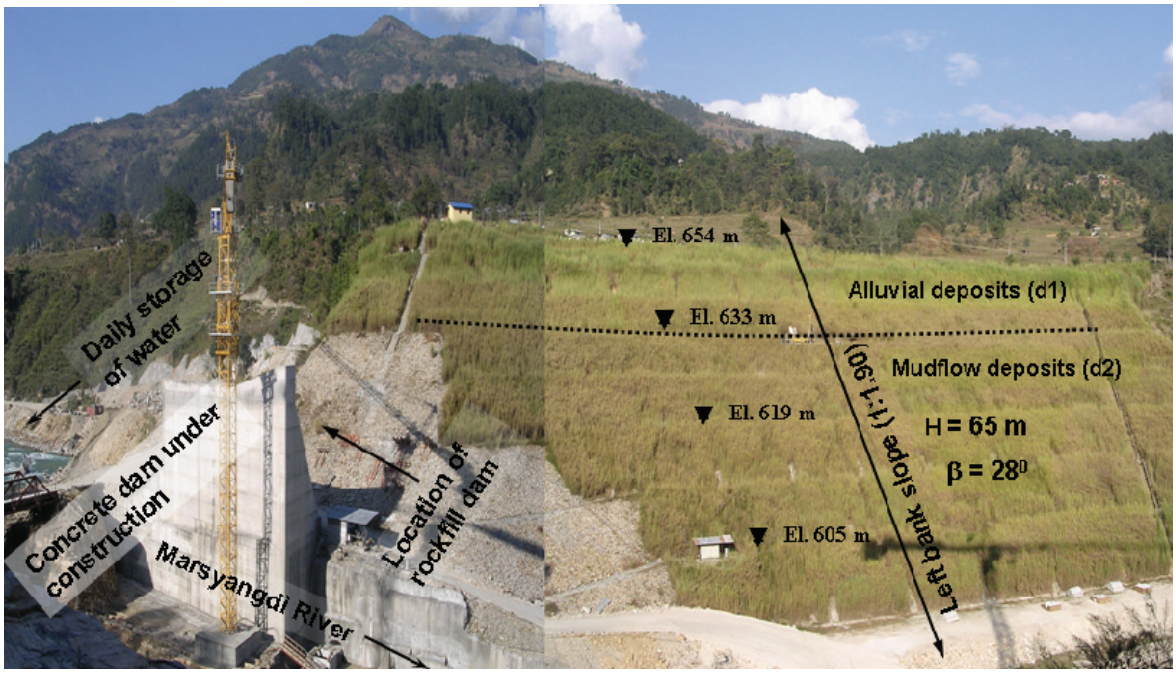

Fig. 6.1 View of the dam site LB slope (photo from November 2004)

The dotted line shown in Fig. 6.1 indicates the assumed boundary used for the slope modelling. The upper soil layer (d1) originated from alluvial river deposits, whereas the lower soil layer (d2) was formed from mudflow deposits as explained in Chapter 4. Based on the present laboratory investigations, both soils in the slopes are classified as silty sand mixed with fractions of gravel and boulders see Chapter 5, Section 5.3.1.1 for soil classification.

Beside the concrete dam, a rockfill dam has been planned at the base of the upper part of the slope, as indicated in Fig. 6.1. The toe of the slope is hence not only supposed to carry the load from the dam, but it should also function as a water retaining structure for daily impound. These important functions can only be guaranteed if the slope remains in a stable condition.

Before the excavation works, the natural slope was steeper (35^0) near the dam location than further downstream (28^0). The slope was excavated to a variable depth of about 15–25 m. The existing slope can hence be assumed overconsolidated with a preconsolidation pressure of about 300-400 kPa. At present, the designed slope remains with 3 m wide intermediate berms at intervals of 7 m height. The berm-to-berm inclination is 35^0 (1:1.45), whereas the overall slope is flatter (28^0, 1:1.90). According to the design, the slope will remain 65 m high as shown in Fig. 6.1.

The existing slope has been found stable over the period since 2003. Inclinometers are planned to be installed later to monitor the slope movements. The results from Limit equilibrium (LE) and finite elements (FE) stability analyses herein indicate accordingly that the slope will remain stable for normal design conditions. This conclusion is based on the investigated shear strength parameters for built-in triaxial specimens (Aryal et al. 2005). The LE and FE stability analyses and their results have been presented later in this Chapter.

6.1.2 Powerhouse slope

The powerhouse area is located on the right bank of the Marsyangdi River downstream of the dam site. From this location, the river flow will be diverted through an approximately 6 km long underground waterway, with tunnels and penstock pipes. The foundation of the powerhouse is located at elevation 508 masl, which is about 7 m below the existing riverbed. Fig. 6.2 shows the construction of the powerhouse in an excavated pit at the base of a 60 m high temporary slope.

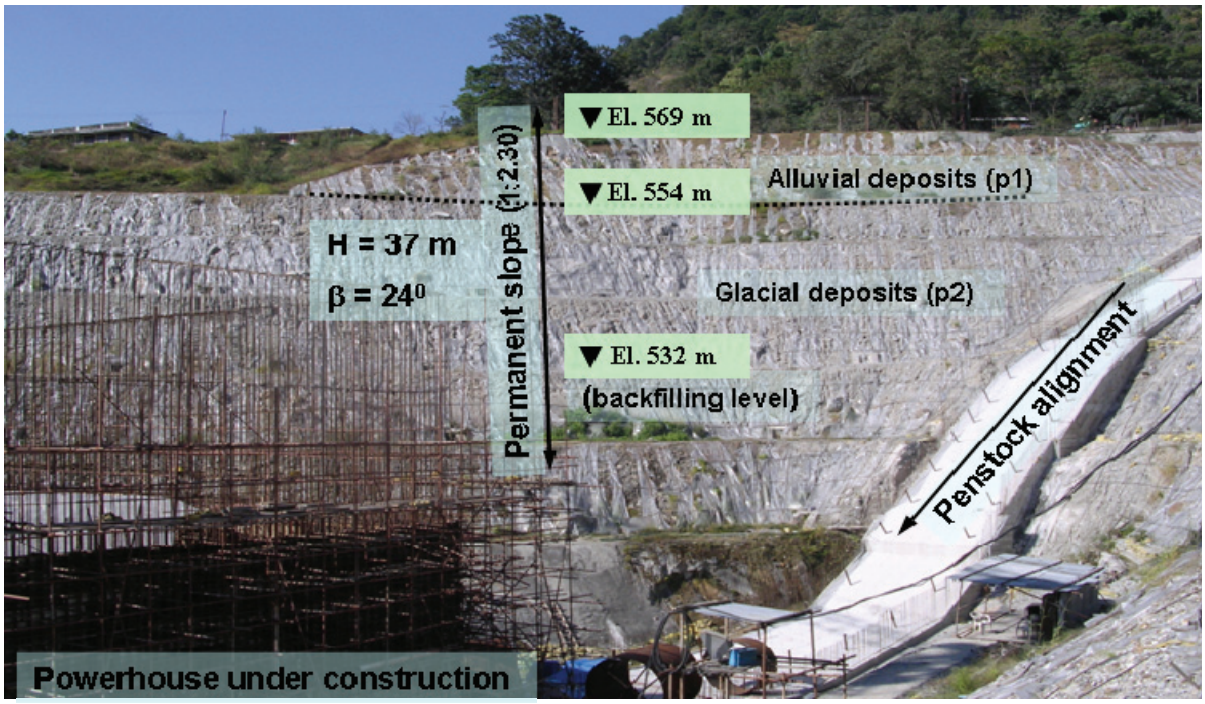

Fig. 6.2 View of the powerhouse slope (photo from November 2004)

According to the previous analysis (Fichtner 2003), the indicated temporary slope will be backfilled up to elevation (El.) 532 masl and re-graded at the end of the construction period. The permanent slope will be flatter (1:2.30) with an overall inclination of 24^0, which will be 7^0 flatter than the original slope. Similar to the dam site slope, there will be 3 m wide berms at every 7 m height, and the berm-to-berm inclination will be 28^0. Moreover, the topography flattens at the El. 569 masl, which means that the permanent slope will remain 37 m high as indicated in Fig. 6.2.

For this slope also, two types of soil were investigated. Accordingly, the soil boundary was assumed at El. 554 masl as shown in Fig. 6.2. The upper layer (p1) consists of alluvial deposits, whereas the lower layer (p2) originates from glacial deposits. The bedrock, which is poor to fair class phyllite, was identified around El. 520 masl by exploratory drilling and excavations (Fichtner 2003). Results from laboratory investigations of soil samples from p1 and p2 are given in Chapter 5. The groundwater table (GWT) and the associate pore pressure distribution in the slopes, representing wet and dry season conditions respectively, were recorded by standpipes (piezometers). The piezometer locations and GWT recordings are given in Chapter 4.

6.2 Slope stability evaluations

The case study slopes were evaluated by LE methods, the computer software SLOPE/W and SLIDE, and finally the FE method using the software PLAXIS. The basic principles of the utilised software and the review of the LE methods are described in Chapter 2.

The slope profiles indicated by the double arrows in Fig. 6.1 and 6.2 were considered for stability evaluations. The aim of the study was not only to evaluate the stability conditions, but also to evaluate the various combinations of loads and/or natural conditions that may influence the stability in the future. Moreover, the study aims to compare the selected LE and FE methods that are commonly used in practice. The study focuses on the effect of GWT variations in dry and wet seasons and the pseudo-static load from earthquakes. First, the pore pressure based on phreatic level and second, advanced groundwater seepage analyses were carried out.

6.2.1 Selected methods for analysis

The most vigorous LE methods, for example Janbu generalised (JG), Morgenstern-Price (M-P) and general limit equilibrium (GLE) procedure were selected for analyses. In addition, Bishop's simplified (BS) and Janbu's corrected (JC) methods were chosen due to their common use in practice. The BS method was also used in the previous analyses, and thus it was possible to compare the corresponding FOS obtained in the present study for similar conditions.

6.2.2 Selected input parameters

The shear strength parameters obtained from drained triaxial tests were selected as input for the stability analyses. The reasons for the selections are discussed in Chapter 5, Section 5.4. The selected input parameters used in the stability evaluations are summarised in Table 6.1.

Table 6.1 Input parameters for static analysis

Soil layers	c′ (kPa)	ϕ′ (^{0})	ψ (^{0})	E'_{ref} (MPa)	ν (–)	γ (kN/m^3)	γ_d (kN/m^3)	k (m/s)
d1	12.6	32.3	5	15	0.25	22	21	$2\ 10^{-7}$
d2	13.5	34.0	5	15	0.25	22	21	$1\ 10^{-7}$
p1	10.5	33.1	10	15	0.25	21	20	$4\ 10^{-8}$
p2	10.5	33.0	0	30	0.25	23	22	$8\ 10^{-7}$
bedrock	5	40	0	100	0.15	23	23	$1\ 10^{-6}$

The given reference stiffness values at 100 kPa vertical stress (E'_{ref}) were determined from the stress-strain relationship of drained triaxial tests. As given in Table 6.1, a small dilatancy angle (ψ), except for the p2 sample, was used in the PLAXIS simulations. Similarly, a realistic value for the Poisson ratio (ν) was assumed. The first five input parameters given in Table 6.1 were

essential for the chosen Mohr-Coulomb model in the FE analyses. Likewise, the permeability coefficient k was used for seepage analysis, for which the appropriate coefficient value for the bedrock was estimated.

Nearly double stiffness values than given in Table 6.1 were obtained from the undrained triaxial tests. Accordingly, different elastic parameters, as given in Table 6.2, were applied for dynamic simulations in PLAXIS, expecting a stiffer response in the undrained conditions during the earthquake shakings.

Table 6.2 Additional input parameters for dynamic analysis

Soil layers	E_{ref} (MPa)	ν (–)	G_{ref} (MPa)	V_p (m/s)	V_s (m/s)	α (–)	β (–)
d1	30	0.15	13	122	78	0	0
d2	30	0.15	13	122	78	0	0
p1	30	0.15	13	125	80	0	0
p2	60	0.15	26	168	108	0	0
bedrock	200	0.10	91	295	197	0	0

A theoretical background of the dynamic analysis in PLAXIS is given in Chapter 2, Section 2.3.3.3, where the last five parameters, given in Table 6.2, are also defined. A lower value of the Poisson's ratio was assumed in undrained conditions. After entering the first two elastic parameters in the input module of PLAXIS, the middle three parameters in Table 6.2 were obtained automatically. These parameters are included here for reference purposes only. Apart from the zero Rayleigh coefficients α and β, and the first two input parameters in Table 6.2, the dynamic analysis utilises the rest of the input parameters from Table 6.1.

6.2.3 Simplified slope models

Both the dam site and the permanent powerhouse slopes were modelled with two soil layers and bedrock or a stiffer layer at the base. The slope modelling was simplified based on the investigated soil stratification and geometrical parameters explained in Sections 6.1.1 and 6.1.2.

6.2.3.1 Modelling of the dam site slope

The boundaries between different soils in the slope were defined with a simplified approach, as said above. Accordingly, the entire slope was divided into three layers as shown in Fig. 6.3. The top and middle layers in this simplification relate to the soil properties of d1 and d2 samples, respectively. Similarly, the bottom layer was assumed a stiffer layer or the bedrock.

In addition, the GWT, as indicated by the dotted lines for dry and wet seasons, were located from the standpipe (piezometer) recordings given in Chapter 4. It was assumed that a similar phreatic surface appears in the chosen slope profile at the same elevation.

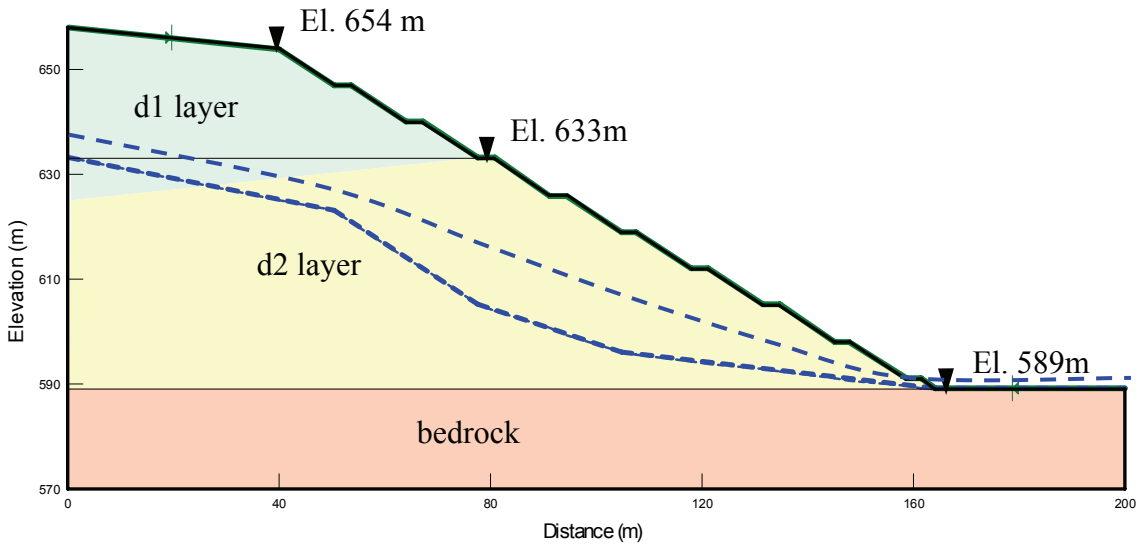

Fig. 6.3 Model for the dam site LB slope

6.2.3.2 Modelling of the powerhouse slope

For simplicity, this slope was also modelled with three soil layers as shown in Fig. 6.4. The approximate boundary between alluvial river deposits (p1 sample) and glaciofluvial deposits (p2 sample) was located at El. 554 masl. Similarly, the properties of the backfill materials were assumed the same as for the p1 sample.

Moreover, the middle layer was related to the properties of p2 sample, which had a mineralogy dominated by calcite. In addition, the model shows the seasonal variations of GWT as indicated by the dotted lines. The GWT close to the crest was defined by the upper piezometer recording, but the GWT close to the toe of the slope was estimated based on the lower piezometer recordings given in Chapter 4.

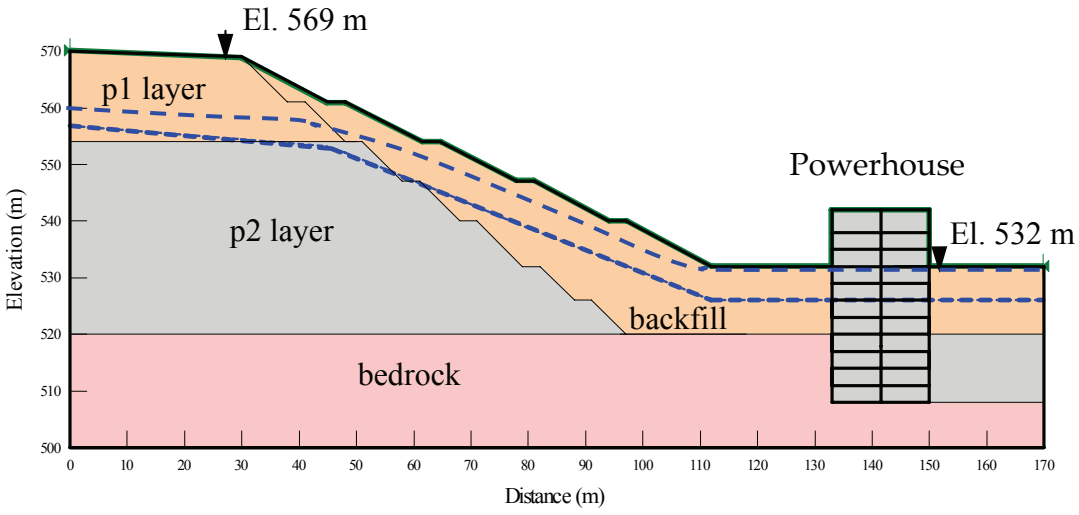

Fig. 6.4 Model for the powerhouse permanent slope

Two unusual characteristics, namely higher permeability and strain softening behaviour were found for the built-in specimens representing the middle layer. Referring to the triaxial tests in Chapter 5, the brittle failure of the soil in addition indicates a failure at low strain levels in the undrained conditions. The bottom layer is bedrock, located around El. 520 masl (Fichtner 2003).

6.2.4 Selected load cases for stability evaluation

Since the effect of groundwater variations is focused on in this study, the selected cases for analyses are related to the GWT for both dry and wet season conditions. In addition, pseudo-static and dynamic earthquakes are also considered in the analyses, as described in Table 6.3.

Table 6.3 Selected load cases for stability evaluation

Case 1:	Variations in GWT: Dry season and wet season pore pressure distribution modelled by a phreatic level, corrected for inclined GWT (corrected as: u = $\gamma_w h_w \cos^2\alpha$, where α is the inclination of GWT) and seepage analyses
Case 2:	Pseudo-static earthquakes analyses, combined with dry season GWT, using a horizontal acceleration coefficient, α_h = 0.15
Case 3:	Dynamic earthquake analyses combined with dry season GWT, using PLAXIS to study the permanent displacements, accelerations, etc in the slopes.

6.2.5 General input parameters

6.2.5.1 The SLOPE/W software

The general input parameters, as used for the idealised slope in Chapter 3, were used to search and refine the circular CSS in SLOPE/W. The entry and exit search option was used to identify the CSS, and this was verified by the auto-locate option. The Mohr-Coulomb soil model and failure criterion, together with a half-sine function for interslice forces were selected. Moreover, the minimum FOS was computed based an assumption of 20 numbers of slices, no tension cracks and no optimisation of the circular CSS. The reader is referred to the description of the SLOPE/W software in Chapter 2 for more information about the CSS search options.

6.2.5.2 The SLIDE software

Computations of FOS in SLIDE were also based on the Mohr-Coulomb failure criterion. Similarly, a half-sine function was used to compute the interslice forces. Exactly the same number of slices as in SLOPE/W was used, together with the assumptions of no tension cracks. An auto-refine search option for a circular CSS was defined as the general input parameters in the model. The CSS was searched among thousands of shear surfaces in SLIDE.

6.2.5.3 The PLAXIS software

The slopes were modelled in the input module of PLAXIS, based on 15 noded elements in a plane strain model. A sufficient, well-refined mesh for the upper two layers was generated to

obtain the least possible FOS. Similarly, the soil properties in each layer were defined using a Mohr-Coulomb soil model. Moreover, the initial stresses due to soil and GWT conditions were computed in the calculation module of PLAXIS. In addition, the computation for steady-state groundwater seepage analyses and the external loads from earthquakes were carried out. Finally, the FOS was computed for separate and combination of loads, based on the c-ϕ reduction procedure. The simulation procedures for pseudo-static analyses and dynamic earthquake analyses are described in Chapter 2, Sections 2.3.3.2 and 2.3.3.3 respectively.

6.2.6 Analyses of the dam site slope

6.2.6.1 Dry season GWT

The dry season GWT recorded from three piezometer stations was defined the same for all three models. Fig. 6.5 shows the CSS and FOS computed by SLOPE/W, where similar results were obtained from the analyses by SLIDE. These results are summarized in Appendix F. The simulation results from PLAXIS are shown in Fig. 6.6.

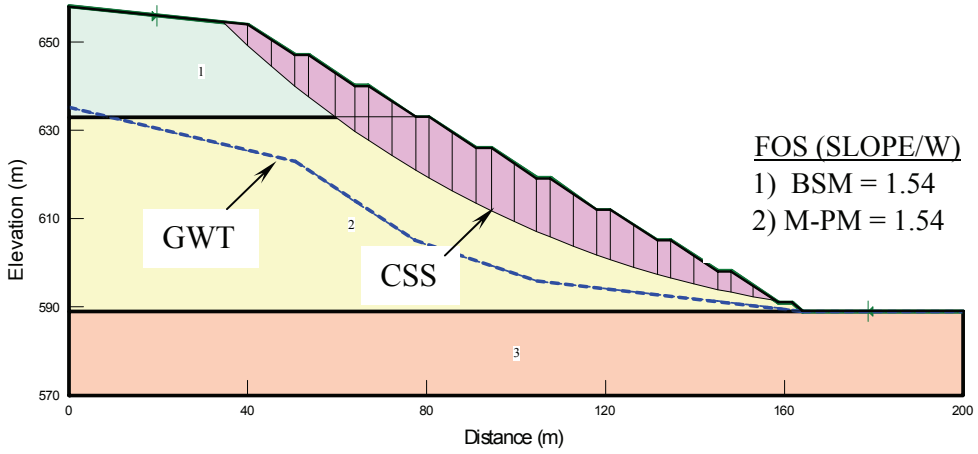

Fig. 6.5 Dry season GWT: FOS and CSS from SLOPE/W

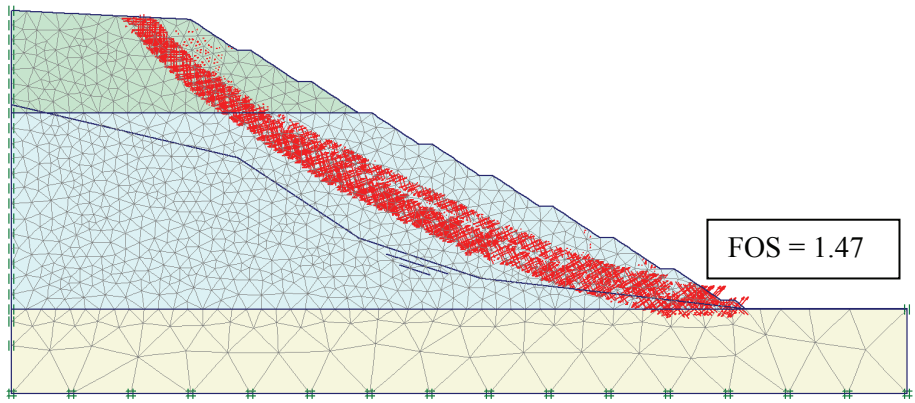

Fig. 6.6 Dry season GWT: FOS and CSS from PLAXIS

Since the CSS is found above the GWT and suction has not been considered in the analysis, the located GWT has no effect on the FOS. LE methods computed the values of FOS higher than 1.5

whereas, slightly lower FOS, mainly because of the composite CSS deepened at the toe was computed in LE analysis. The pore pressure at the toe causes reduction in the effective normal stresses, and hence the shear strength. The CSS in PLAXIS simulations is defined by the concentration of incremental or total strains in the slope profile as indicated in Fig. 6.6.

6.2.6.2 Analyses for wet season GWT

The GWT was raised in the model to represent wet season conditions. The phreatic level was corrected in SLOPE/W and SLIDE. In SLOPE/W, the option for the phreatic level correction was activated to compute the corrected pore pressure distribution. In SLIDE, the automatic H_u ($u = \gamma_w h_w H_u$) option was chosen. Using this option, the software computes the H_u factor between 1 and 0 according to the water surface inclination in the slope (SLIDE 2003). This is related to the equipotential lines, being perpendicular to the flow lines in the inclined GWT.

The results obtained from SLOPE/W are depicted in Fig. 6.7, whereas the FOS from SLIDE is given in Appendix F. Moreover, the PLAXIS results are shown in Fig. 6.8. As before, the FOS in LE analyses is higher than the FOS in FE analyses comparing both figures.

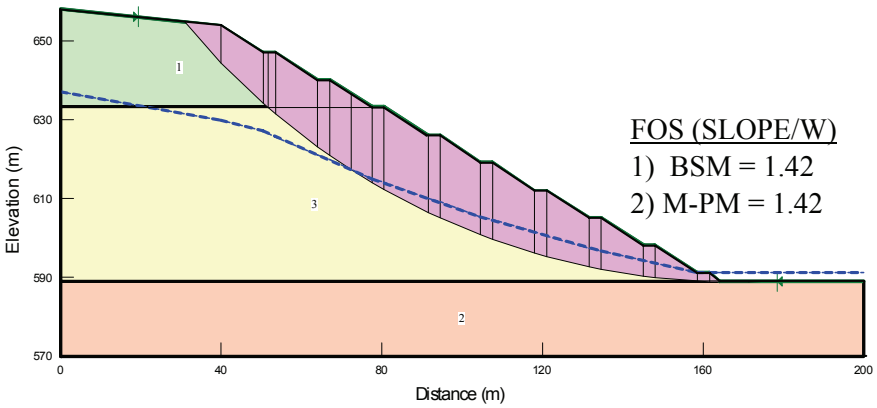

Fig. 6.7 Wet season GWT: FOS and CSS from SLOPE/W

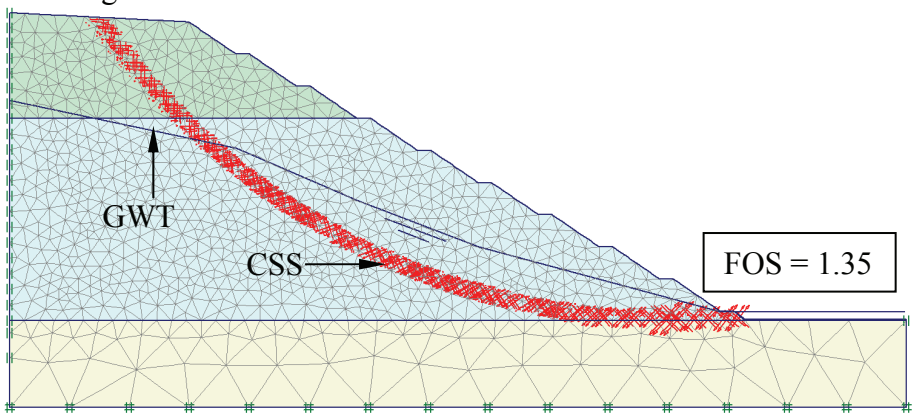

Fig. 6.8 Wet season GWT: FOS and CSS from PLAXIS

PLAXIS utilises either phreatic level pore pressure, which means hydrostatic distribution, or pore pressures obtained from a steady-state seepage analysis. However, the same option, as applied in the LE analyses for phreatic level correction, was tried to simulate in PLAXIS by some

adjustments. Accordingly, the pore pressure distribution was generated using the phreatic level with slightly reduced unit weight of water (γ_w) depending on the inclination of the GWT. The water surface inclination (α) was computed around 20^0, and an equivalent reduction factor was obtained by $\gamma_w \cos^2\alpha$. In this way, the correct pore pressure distribution was correctly applied in the PLAXIS analyses, as suggested by Grande and Waterman (2005) by personal communications. It was decided to use the option for inclined GWT in slope stability analyses.

6.2.6.3 Groundwater seepage analyses

The effects of groundwater flow and seepage were studied further to evaluate the stability conditions. Accordingly, seepage analyses were carried out in SEEP/W, SLIDE (groundwater module) and PLAXIS (steady-state groundwater calculation scheme). The results of the seepage analyses from the computations are presented in Appendix E for comparison and visualisation of the flow patterns.

In the SEEP/W software, the hydraulic functions were estimated based on the grain size distribution of the upper two soil layers. In addition, the saturated permeability obtained from the laboratory tests, a suggested coefficient of compressibility (m_v = 0.1), which is the value of slope of the water content function (SEEP/W 2005), and an assumed volumetric water content (θ_w = 0.45) were used as input parameters for the seepage analyses. Moreover, the boundary conditions for water flow were defined according to the water head and GWT. Similarly, the same hydraulic functions and boundary conditions were defined in SLIDE. In PLAXIS, closed flow boundaries were defined at the base, whereas water heads were located at the sides of the model. Likewise, dense meshes were used in all analyses to obtain precise pore pressure distribution.

The pore pressure distribution obtained was then used in the slope stability analyses, and accordingly the FOS was computed. Fig. 6.9 shows the results obtained from the computation in SLOPE/W. The breaks on the phreatic surface indicate the applied zero pressure points as GWT.

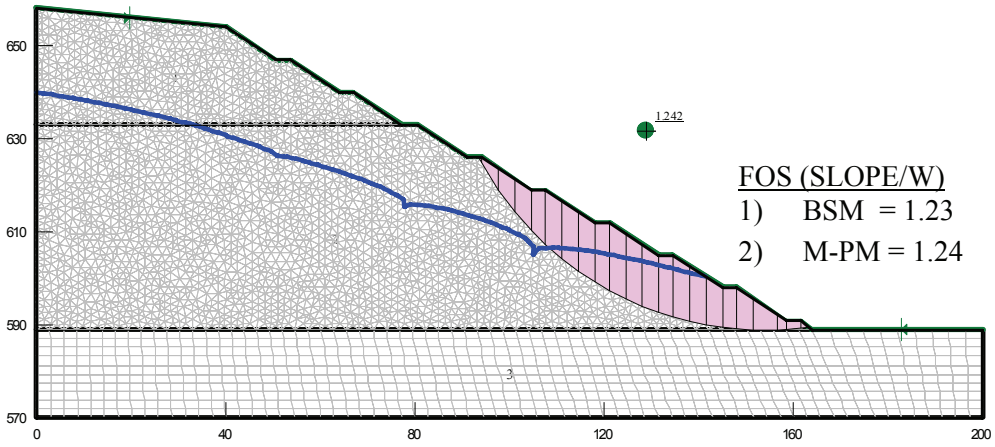

Fig. 6.9 FOS and CSS after the seepage analysis in SEEP/W

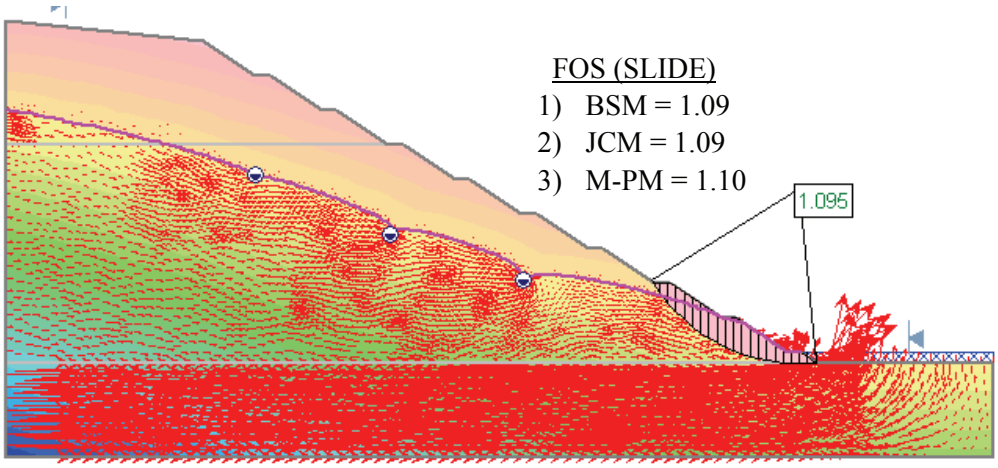

Fig. 6.10 FOS and CSS after the seepage analysis in SLIDE

Fig. 6.10 shows the results from SLIDE analyses. The failure was localised at the toe of the slope in the completely saturated zone. The seepage analyses show much lower FOS, and indicate that failure may initiate from the toe of the slope for the given conditions. The low FOS is related to a reduction in normal stresses and frictional resistance over submerged parts of the slip surface.

Similarly, the FOS computed by PLAXIS is given in Fig. 6.11, which shows a limiting equilibrium condition. In addition, the CSS was found to be located at the toe, somewhere in between those obtained by SLOPE/W and SLIDE. Both the LE and FE analyses show that the toe remains the critical part of the slope, from where failure may initiate in saturated conditions. Any remedial measures applied to lower the groundwater at the toe will have substantial improvement in FOS.

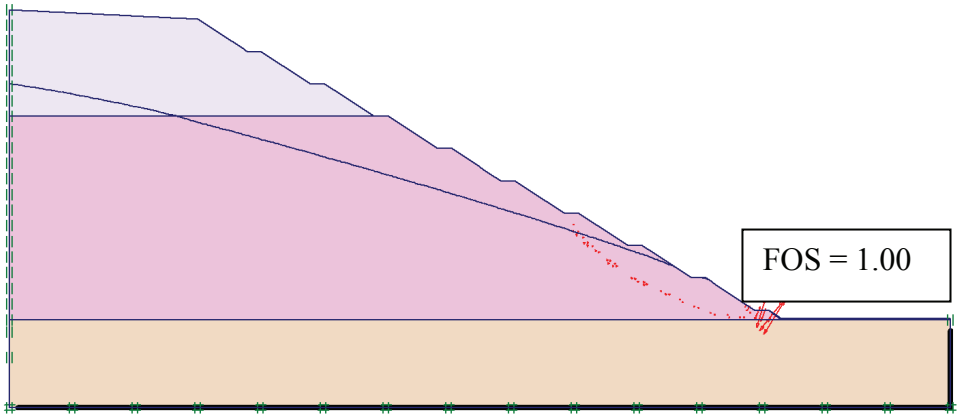

Fig. 6.11 FOS and CSS after seepage analysis in PLAXIS

Fig. 6.12 demonstrates the effect of groundwater on the slope stability. This further indicates that the seepage flow is a critical factor, particularly for permeable materials. The seepage analysis with the wet season GWT as input to PLAXIS shows that the slope reaches a critical equilibrium state. However, the FOS was improved from 1.0 to 1.2 by introducing a horizontal drainage

system in the model, as indicated by the analysis results given in Appendix E, Fig. E.4. Moreover, the drainage pipes in the real slope may have contributed to lower the GWT, and may already have influenced the piezometer levels.

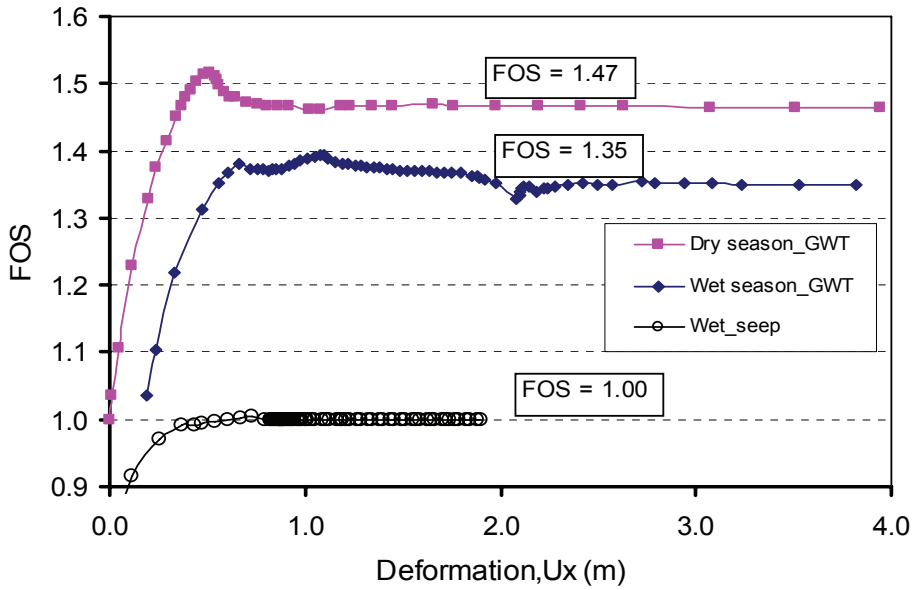

Fig. 6.12 Groundwater effects on FOS from PLAXIS computations

In addition, some pressure relief wells are planned to install at the bottom of the slope (see Chapter 4, Fig. 4.1). The improvement in FOS due to such arrangements was also studied in the SEEP/W and SLIDE analyses. It was also attempted to simulate the option with wells in PLAXIS, but due to non-convergence of the steady-state groundwater calculations, further computation for the FOS was not possible to carry out.

Fig. 6.13 reveals a significant improvement in FOS after the introduction of the pressure relief wells, which are assumed to lower the pressure at the toe of the slope. To represent the planned conditions, two points around the toe, as indicated in Fig. 6.14, were given zero pore pressure to simulate full drainage conditions. The stability analyses were then carried out in SLIDE.

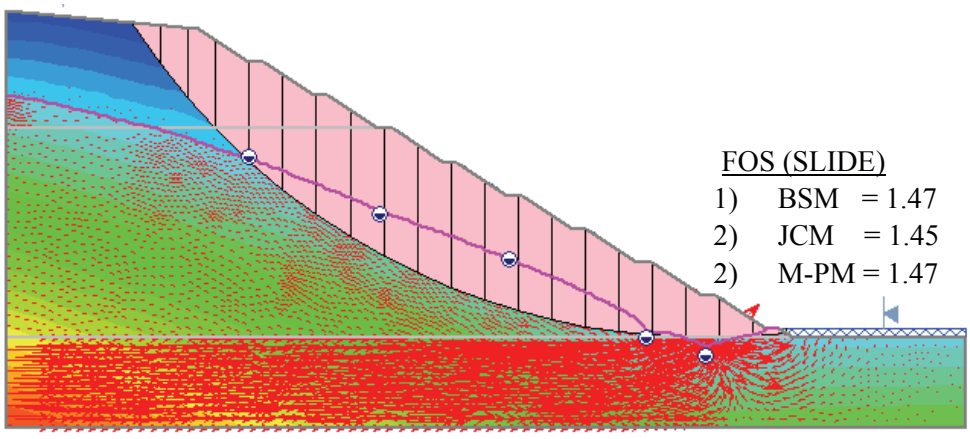

Fig. 6.13 FOS and CSS after introduction of two wells in SLIDE

Exactly the same boundary conditions were applied in SEEP/W, and the stability analyses were carried out accordingly. Also in this analysis, the FOS was found significantly improved, as was the case with SLIDE. The CSS and the corresponding FOS are shown in Fig. 6.14.

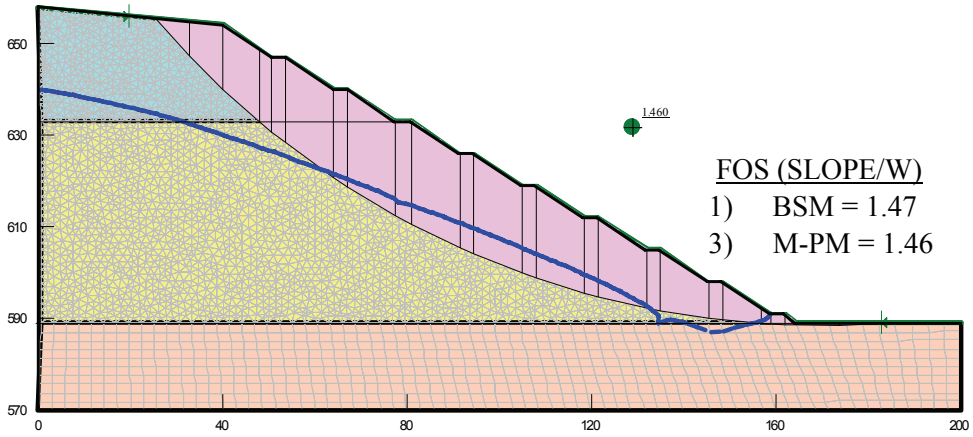

Fig. 6.14 FOS and CSS after seepage analysis in SEEP/W and stability in SLOPE/W

Compared to the situations with and without wells, the phreatic surface was found much lower at the toe after application of the wells. This shows that the pressure relief wells will have significant improvement in FOS as long as the drainage wells function satisfactory.

6.2.6.4 Pseudo-static analyses

Load Case 2 was analysed combined with dry season GWT and a horizontal earthquake coefficient $\alpha_h = 0.15$. The results from the SLOPE/W analysis are given in Fig. 6.15. Furthermore, similar FOS was obtained from the analysed in SLIDE, and the results are presented in Appendix F, Fig. F.3.

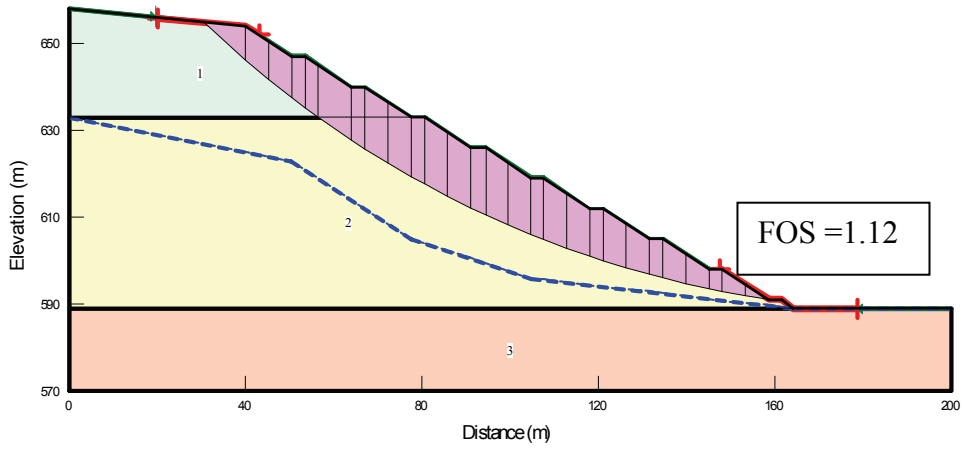

Fig. 6.15 CSS and FOS from pseudo-static analyses (SLOPE/W)

The pseudo-static analyses show that the FOS is higher than the minimum value (FOS >1.05), referring to the design limit applied in the previous stability analyses, (see Chapter 4, Section 4.9.4). However, the wet season GWT resulted in limiting equilibrium conditions.

6.2.6.5 Dynamic earthquakes simulations

Load Case 3, defined in Table 6.3, was simulated in PLAXIS in order to study the effects of dynamic earthquake vibrations. For this purpose, the extended model was used as shown in Fig. 6.16. The reason for extending the model horizontally was to minimise the effects of return waves from the boundaries. In the dynamic analysis, the outgoing seismic waves were supposed to be absorbed by the applied boundaries at both sides of the model.

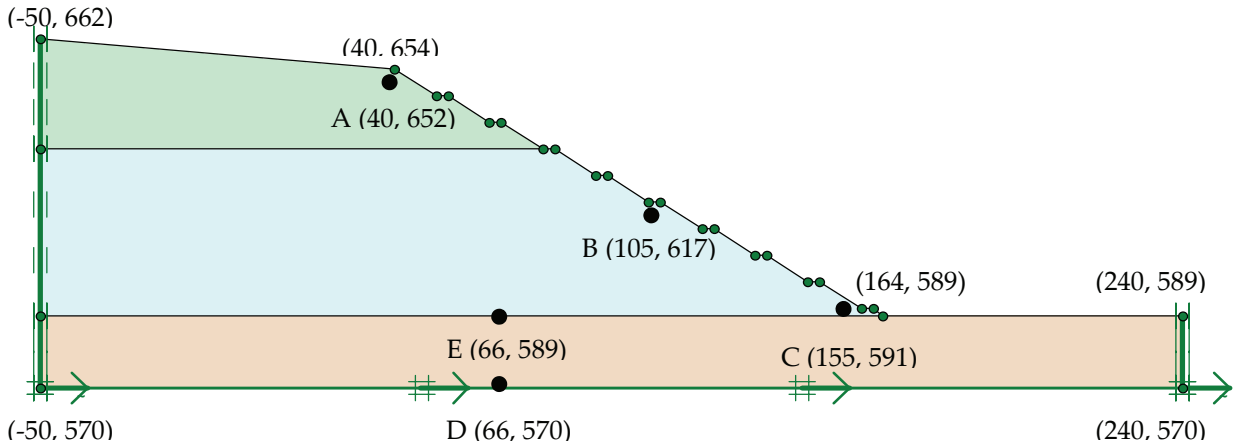

Fig. 6.16 Extended dam site LB slope model used for dynamic analyses in PLAXIS

The study aimed to investigate the influence of dynamic effects, particularly permanent displacement, acceleration and excess pore pressure at the selected points A, B and C in Fig. 6.16. In addition, a base point D and an intermediate point E were also selected to verify the input accelerations and compare the pore pressures. The analyses were performed using the first two soil parameters from Table 6.2 and the rest of the parameters from Table 6.1. In addition, the acceleration-time series, given in Fig. 6.17, was applied as the input parameter for simulations.

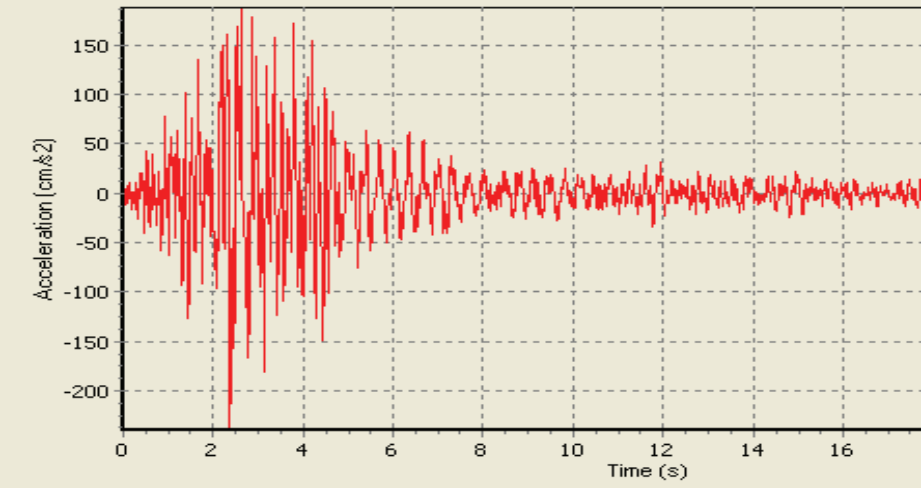

Fig. 6.17 Input accelerogram for dynamic analyses (PLAXIS 2004)

The input acceleration-time series was taken from the PLAXIS manual (2004). The accelerogram was recorded at 5 km distance from the epicentre for an earthquake of magnitude M 5.4, which produced 2.40 m/s^2 PGA with 200 Hz frequency (see Fig. 6.17). Some theoretical discussions of the dynamic simulations in PLAXIS have also been presented in Chapter 2, Section 2.3.3.3.

Referring to Chapter 4, Section 4.7, the design horizontal acceleration during an earthquake (α_h) should be 0.15g for the case slopes. According to the seismic studies carried out for the project area, the design acceleration was considered to 35% of PGA. This means, the PGA should have to be as high as 4.20 m/s^2 to generate 0.15g horizontal acceleration as the recommended value for simulations. This information was utilised to determine the prescribed displacements, which was applied at the base of the model.

In the initial stages of simulations (not presented here), a prescribed displacement of 1 cm (U_x = 0.01 m) was imposed at the base of the model and the PGA at point D was verified by outputs and found 1.75 m/s^2. In fact, it should have produced the same PGA as the input, i.e. 2.40 m/s^2 (see Fig. 6.17). Further use of U_x =0.02 m, a double PGA at point D was found, i.e. 3.50 m/s^2. In this way, the prescribed displacement (U_x = 0.024 m) was selected to apply at the base of the model. This prescribed displacement produced the same PGA (4.2 m/s^2) as for the design value.

Table 6.4 Calculation stages in the dynamic earthquake simulations

Identification	Phase no	Start from	Calculation	Loading input
M-weight	1	0	Plastic	Total multipliers
Dry season GWT	2	1	Plastic	Staged construction
Undrained materials	3	2	Plastic	Staged construction
Pres. displ. (0.024 m)	4	3	Plastic	Staged construction
Dynamic analyses	5	4	Dynamic analyses	Total Multiplier

The stages involved in dynamic analyses are given in Table 6.4. First, the initial stresses were computed by gravity loading (m-weight) in the calculation routine. Next, the dry season GWT was defined in the model and the pore pressures from the phreatic level were generated. In the following stage, the input model was defined by undrained materials to simulate earthquake events. Moreover, the prescribed displacement (Ux = 0.024 m) was applied by staged construction in the input module. Finally, the given accelerogram was defined for dynamic analysis as a total multiplier to perform the simulation for a period of 10 sec.

Fig. 6.18 shows the output of the simulations, which indicate the shading of total shear strains concentrated in the slope. Two light coloured sections can be seen in Fig. 6.18: One on the top layer, the other in the deep strata. This is the likely situation during earthquakes of similar magnitude. Moreover, plastic points were observed all over the slope during the simulations. It indicates that the materials will reach to the plastic stage on the right side of the yield surface.

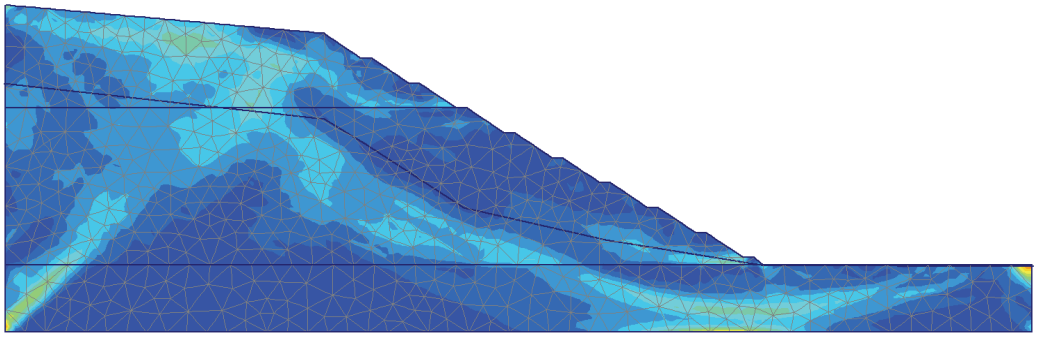

Fig. 6.18 Shear shading after the phase # 5 simulations (dam site LB slope)

Fig. 6.19 shows the permanent displacements for the selected points. The points close to the surface (i.e. A, B, C) have experienced large permanent displacement compared to the points inside the model. Similarly, the base point D was found the least displaced, which was logical.

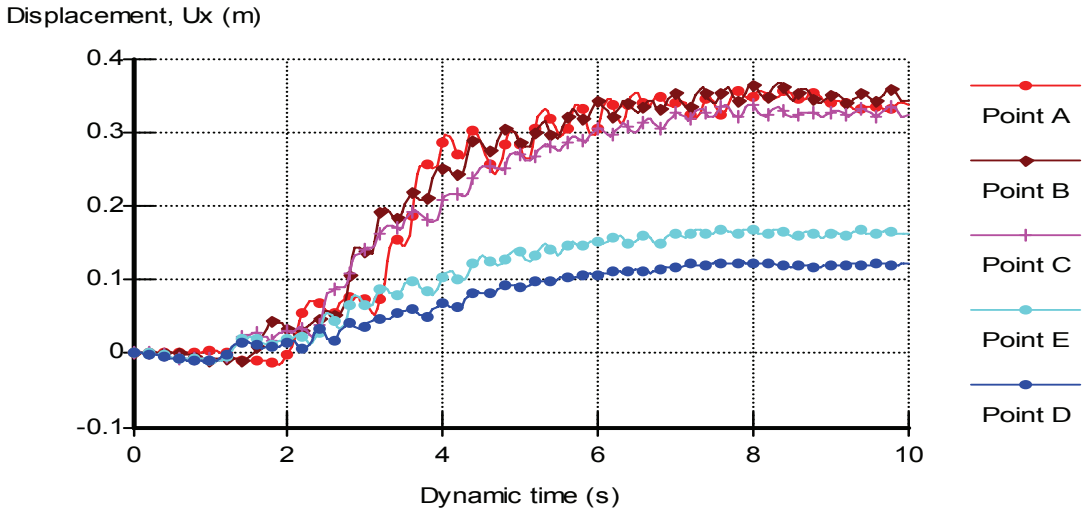

Fig. 6.19 Permanent displacement in the slope at selected points

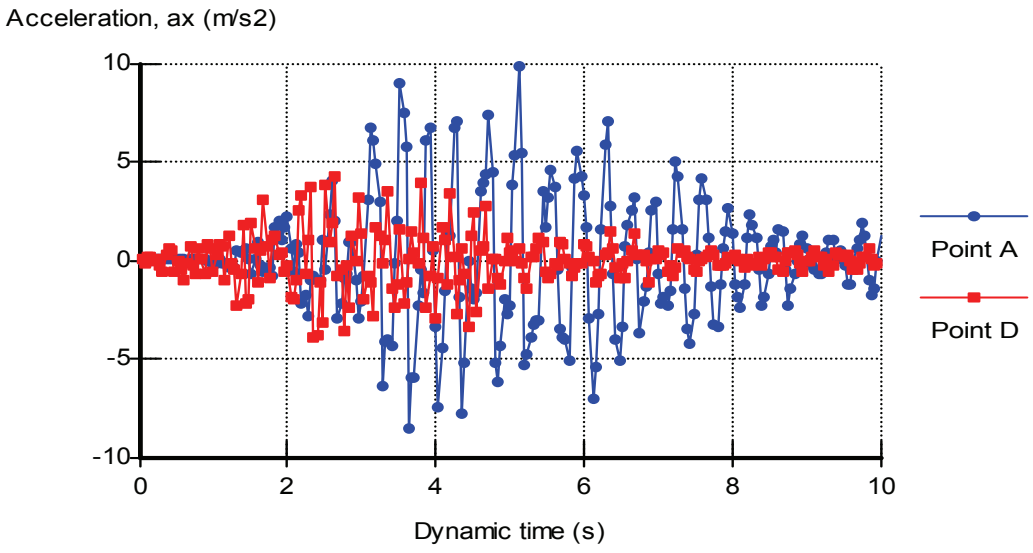

Fig. 6.20 Output of acceleration - time series at points A and D

Furthermore, the output results (see Fig. 6.20) were studied in terms of acceleration - time series at two selected points A and D. Point D was selected to verify the input acceleration produced by the applied prescribed displacements. Similarly, point A was chosen to observe the horizontal acceleration close to the surface. As indicated in Fig. 6.20, the base acceleration at point D was found the same as for the input accelerogram with U_x = 0.024 m. However, point A was found to have higher peak acceleration. Similar values were found for points B and C. This indicates that both the crest and toe of the slope may become critical during earthquakes events.

Fig. 6.21 shows the excess pore pressure (total minus hydrostatic) at the five selected points. The positive side of the excess pore pressure for points D and E indicates additional (excess) pore pressure generated due to the dynamic undrained loading. Similarly, the negative side shows the suction developed in the slope. The legends are given in chronological order indicating the point B with the highest suction.

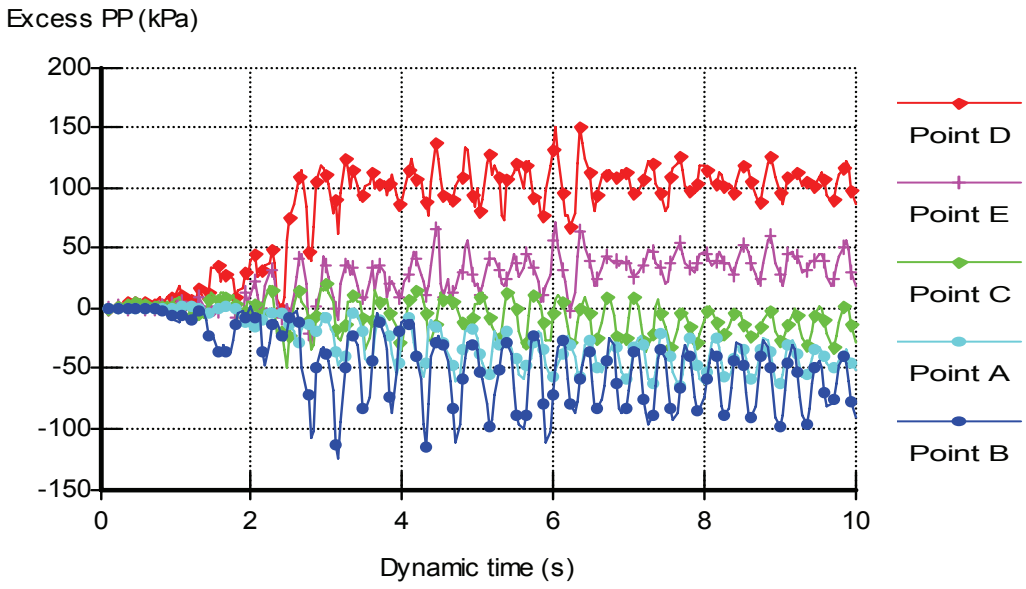

Fig. 6.21 Excess pore pressure (negative side indicates suction)

Point B indicates the highest suction, whereas point C, which is located close to the GWT at the toe, shows the lowest among the three selected points above the GWT. The simulation indicates that suction is likely to generate above the GWT, whereas the slope below the GWT is likely to experience excess pore pressure. This is a logical response for undrained loading conditions. The materials with 40% fines can easily sustain the developed suction in the slope.

The suction will have a positive contribution to the slope stability. A small suction at point C means that the toe areas may experience critical conditions during earthquakes. Moreover, the shear shading in Fig. 6.18 indicates that a failure, if it occurs, is likely to initiate either from the crest or from the toe. Liquefaction ($\sigma_v' < 0$) could be another problem in earthquake events at the toe area. However, with the suction at point C, which is located very close to the toe, the risk of liquefaction is very uncommon for the analysed slope at the dam site LB.

6.2.7 Analyses of the powerhouse slope

The analyses were performed in exactly the same way as in the previous case study, using the soil parameters from Table 6.2. Similarly, all simulations follow the defined load cases in Table 6.3. The general input parameters in SLOPE, SLIDE and PLAXIS simulations remain the same as explained in Section 6.2.5. Therefore, only the analyses results for various load cases are presented and discussed herewith.

6.2.7.1 Analyses for dry season conditions

The dry season GWT was defined in the models by locating the two available piezometric readings. Since the permanent slope will be graded at the end of the construction, the GWT in the slope may change from what is recorded today. However, the aim here is to find the FOS with the applied GWT in the slope.

Similar to the dam site slope analyses, the pore pressure distribution was computed from the corrected phreatic level in SLOPE/W and SLIDE. The CSS and corresponding FOS from SLOPE/W are presented in Fig. 6.22.

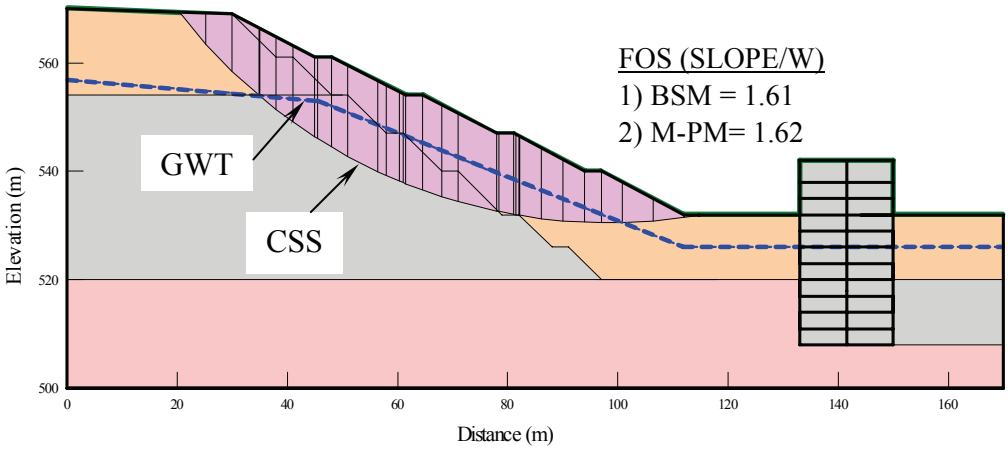

Fig. 6.22 Dry season GWT: CSS and FOS from SLOPE/W

Application of exactly the same GWT and selection for automatic H_u ($u = \gamma_w h_w H_u$) in the pore pressure computations, the SLIDE analyses had almost the same FOS as presented in Appendix F, Fig. F.4. As explained before, the software computes the value of H_u automatically based on the inclination of the water surface. This option is the same as the phreatic level correction in SLOPE/W for an inclined GWT. Both LE analyses produced identical CSS and the same FOS.

The reduced unit weight of water was used in PLAXIS for the pore pressure computations, and the pore pressure distribution was generated using the phreatic level. Based on the inclination of the GWT for the inclined section, the unit weight of water (γ_w) was lowered by the $\cos^2\alpha$ term, with α being around 20^0 for both dry and wet GWT. The reduction was applied only for the inclined GWT in the static analyses. Similarly, the dilatancy angle, as given in Table 6.1, was introduced in the material properties for the p1 soil layer.

The CSS and the FOS from the PLAXIS analyses are given Fig. 6.23. The FOS is slightly lower than that obtained in the LE analyses, but greater than 1.5, which was used as a limiting value for the slope design.

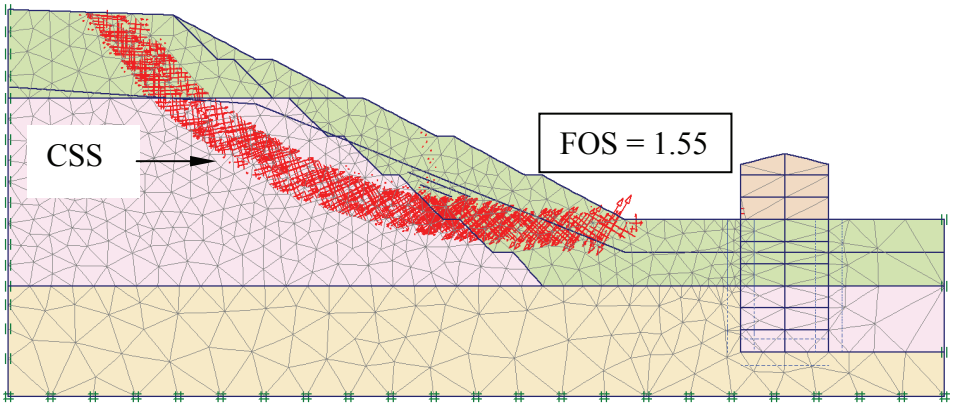

Fig. 6.23 Dry season GWT: CSS and FOS from PLAXIS

6.2.7.2 Analyses for wet season conditions

All simulations were carried out for similar conditions as for dry season conditions, the only difference being the GWT representative for wet season conditions. The CSS and the FOS from SLOPE/W analyses are shown in Fig. 6.24, which is comparable to the SLIDE analyses given in Appendix F, Fig. F.5.

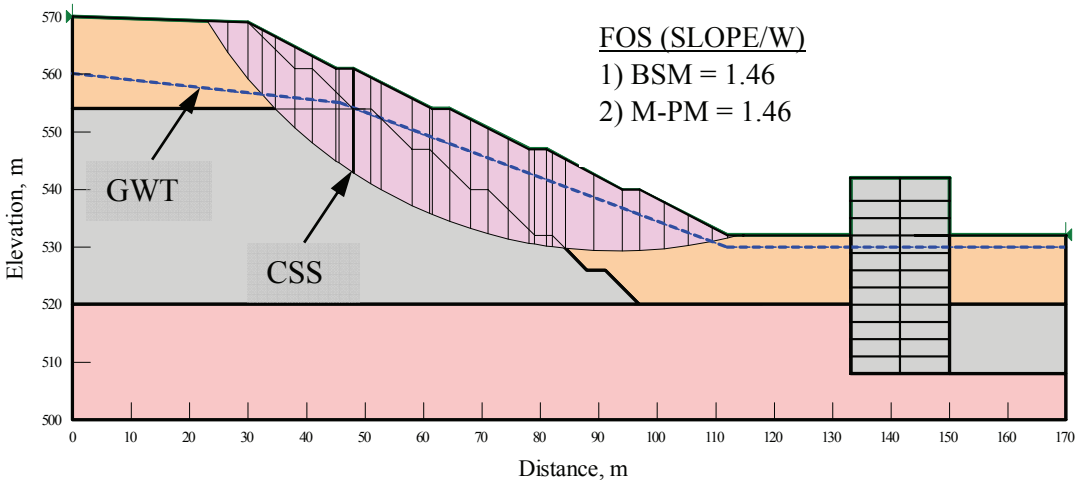

Fig. 6.24 Wet season GWT: Failure surface and FOS from SLOPE/W

The rise in GWT from dry to wet season conditions was also analysed by PLAXIS, which produced slightly lower FOS, as shown in Fig. 6.25. Comparisons between the dry and wet season conditions show that the FOS may be reduced by 10% in LE and 13% in the FE analyses, with the FOS for dry season conditions being the reference conditions. The analyses actually show that stable conditions prevail in the slope for both dry and wet season conditions.

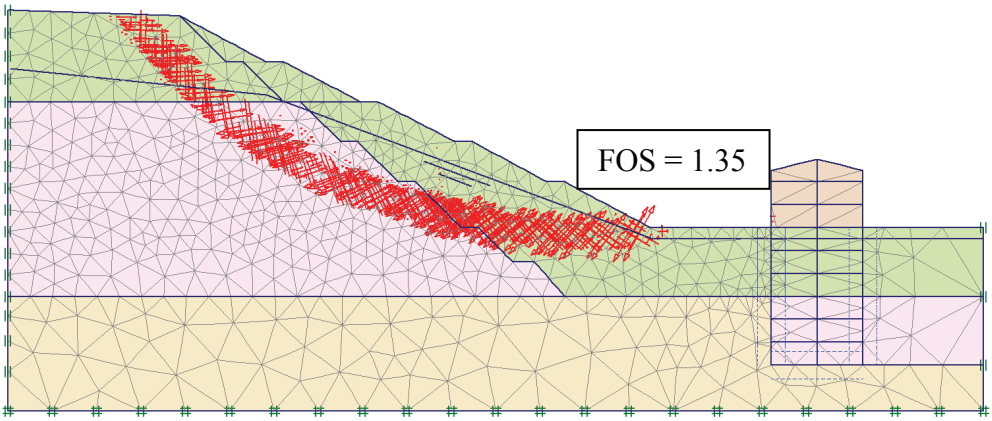

Fig. 6.25 Wet season GWT: Failure surface and FOS from PLAXIS

6.2.7.3 Groundwater seepage analyses

The seepage analyses for the powerhouse slope were carried out using the wet season GWT. First, the analyses were performed without any drainage measures, which implied too low FOS-values (see Fig. E.7 in Appendix E). Next, a situation representing the application of 20 m long horizontal drainage pipes was analysed. The, FOS was then improved, approaching the equilibrium level (see Fig. E.8). Finally, the analyses with the two pressure relief wells at elevation 520 masl were carried out, showing that the FOS improved to an acceptable limit, as shown in Fig. 6.26.

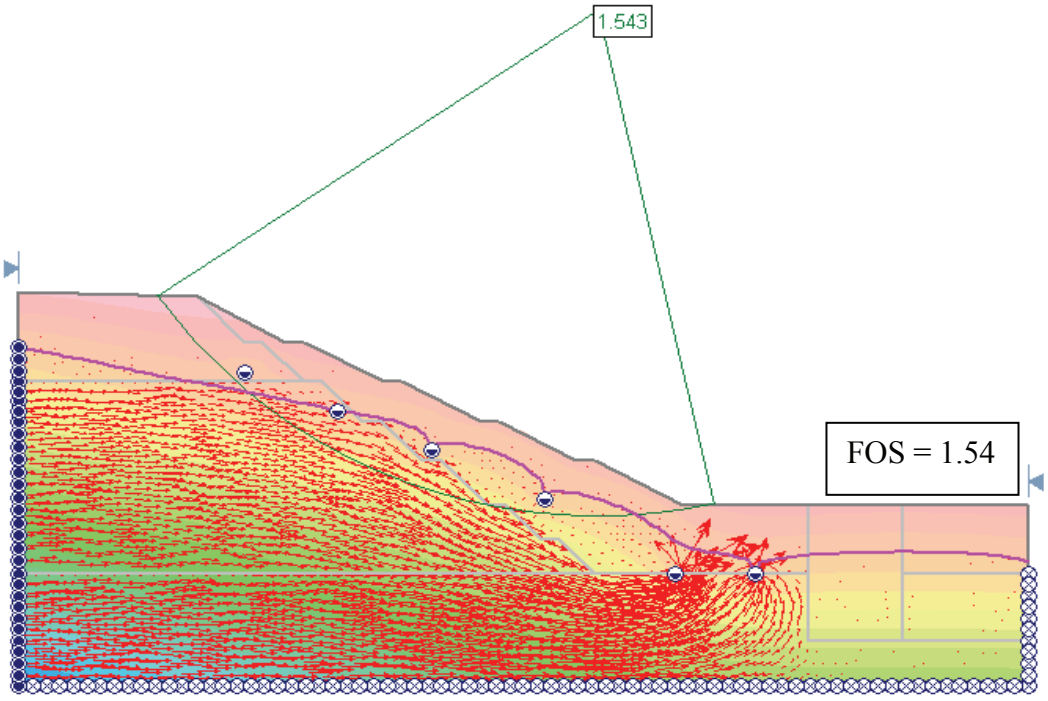

Fig. 6.26 FOS and CSS after seepage analysis in SLIDE

The points indicated in Fig. 6.26 are the combinations of 20 m long horizontal drainage pipes and two pressure relief wells. Seepage analysis reveals an unstable slope in wet season

conditions, and hence the drainage systems as indicated in the analysis are highly recommendable.

6.2.7.4 Pseudo-static analyses

The pseudo-static analyses were carried out for the load combinations given in Table 6.3. Since the CSS was found below the GWT, the pore pressure was computed by phreatic level correction as explained earlier. The results from the analyses are given in Fig. 6.27.

The theoretical background of the pseudo-static analysis has been described in Chapter 2 under the PLAXIS section. The direction of the ground motion was assumed towards the river valley, being the most critical condition.

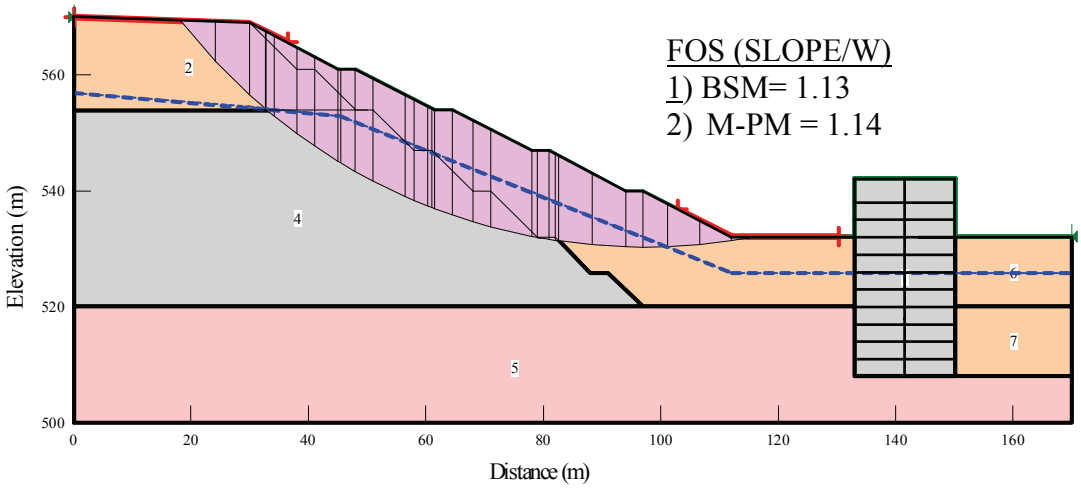

Fig. 6.27 FOS from pseudo-static analyses in SLOPE/W

The results obtained by SLIDE are given in Appendix F, Fig. F.6. As before, both the LE software SLOPE/W and SLIDE were found to produce similar FOS-values. The pseudo-static analyses show that the FOS may be reduced by as much as 30% by similar intensity of earthquakes (4.2 m/s^2 PGA). Moreover, the analyses carried out by FEM show that a critical condition may appear in the slope for the given PGA.

6.2.7.5 Dynamic earthquake simulations

Dynamic analysis were performed in exactly the same way as in the previous case, using the first two elastic soil parameters from Table 6.2 and the rest of the parameters from Table 6.1. Likewise, the calculation steps defined in Table 6.4 were followed, using undrained conditions to simulate the earthquake events. In addition, the dry season GWT was introduced in the model. As for the dynamic input parameters, the acceleration-time series given in Fig. 6.17, and a prescribed displacement of 2.4 cm were used for simulations. The reason of selecting 2.4 cm displacement has been explained in the previous case study. The displacement was applied at the base of the model to produce an equivalent PGA of 4.2 m/s^2.

Fig. 6.28 shows the extended model, which was used for the analyses. As in the previous case study, the study was aimed to find the influence of dynamic effects in terms of permanent displacement, acceleration and excess pore pressure at selected locations. Accordingly, three points closer to the surface (A, B and C) and three points (D, E and F) inside the model were chosen.

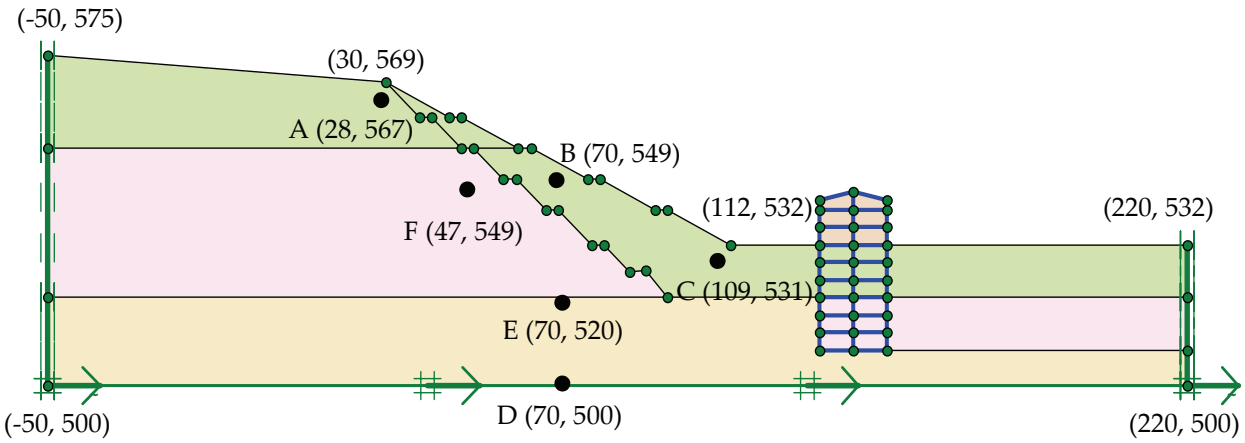

Fig. 6.28 Extended powerhouse slope model used for dynamic analysis

As one of the simulation outputs, Fig. 6.29 shows the shear shading (concentration of shear strains) of the total strains. There are two light coloured sections, which indicate possible failure in both soil layers. Moreover, the base of the powerhouse is also seen strained compared to the sides. Further increase in GWT during rainy season may have instability problem at the toe.

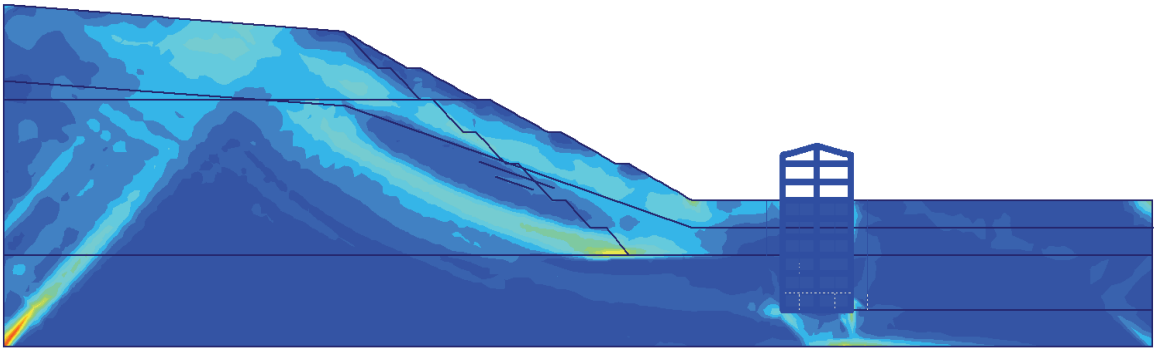

Fig. 6.29 Shear shading after the dynamic analysis of powerhouse slope

The acceleration outputs at point A and D are compared in Fig. 6.30. Similar to the previous case study, the acceleration at point D was found identical, which indicates the response of the applied prescribed displacement and acceleration-time series. However, the surface point A shows the highest acceleration amplitude, peaking up to nearly full gravity acceleration. Two surface points B and C also showed similar acceleration values as of point A.

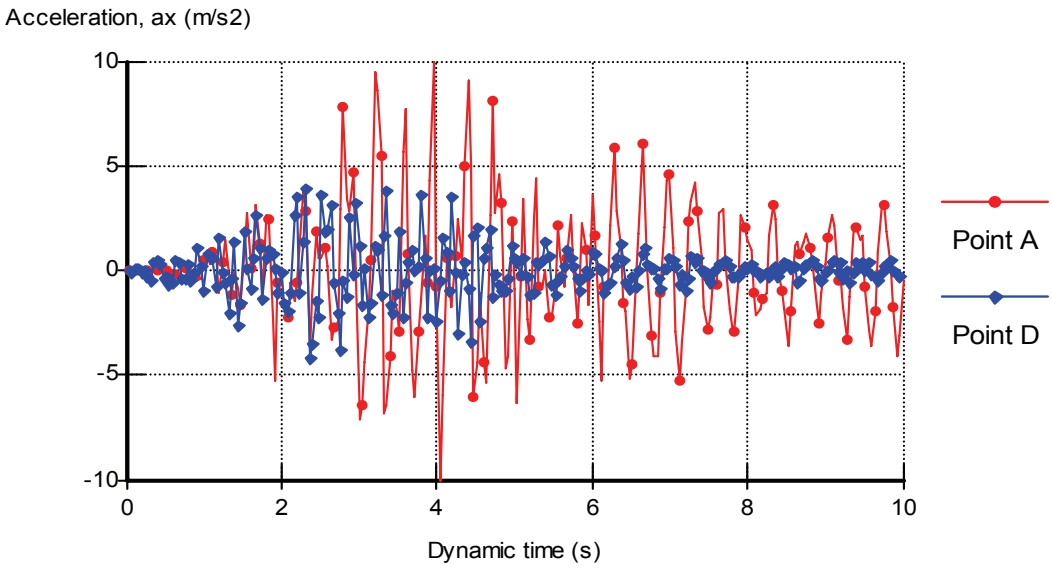

Fig. 6.30 Output of acceleration-time series at points A and D

Moreover, the permanently accumulated displacements at the selected points are compared in Fig. 6.31. The legends show displacements in chronological order indicating the surface point B as the most displaced. Moreover, the points A, C, D and E in Fig. 6.31 show the similar trend of displacement compared to the corresponding points in the previous case study (see Fig. 6.19).

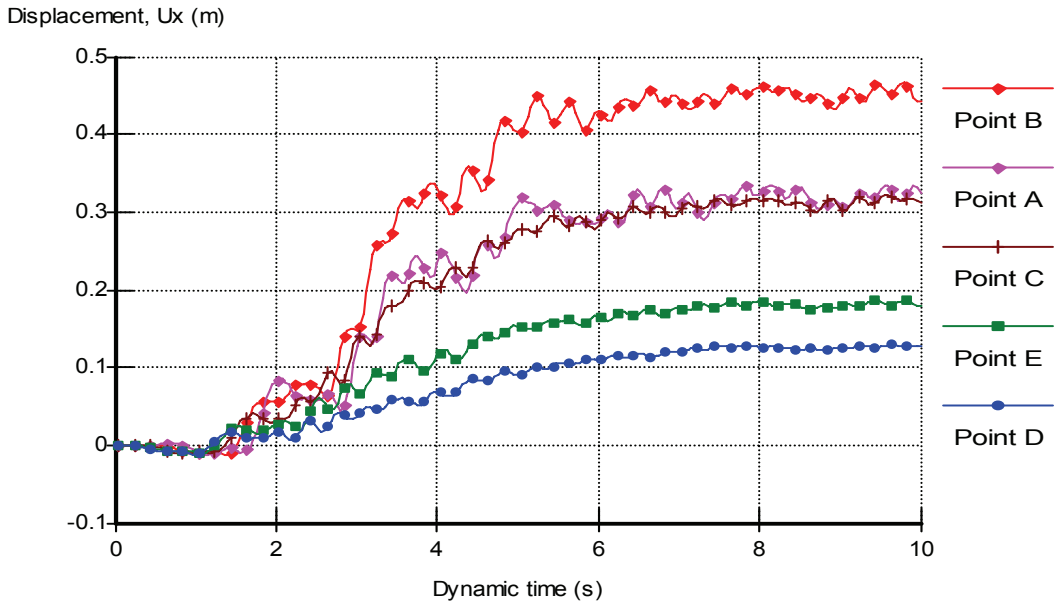

Fig. 6.31 Permanent displacement-time series at selected points (undamped system)

The dynamic analyses assume undamped system, in which the Rayleigh damping coefficients α and β are assigned to zero values. However, the real conditions may have some damping, and thus the results may be on conservative side. The damping ratio (ζ) can be obtained experimentally by means of the resonance column test (Das 1995). Similarly, with the value of

ζ and resonance frequencies, the values of the damping coefficients α and β can obtained (PLAXIS 2004, Bathe 1996).

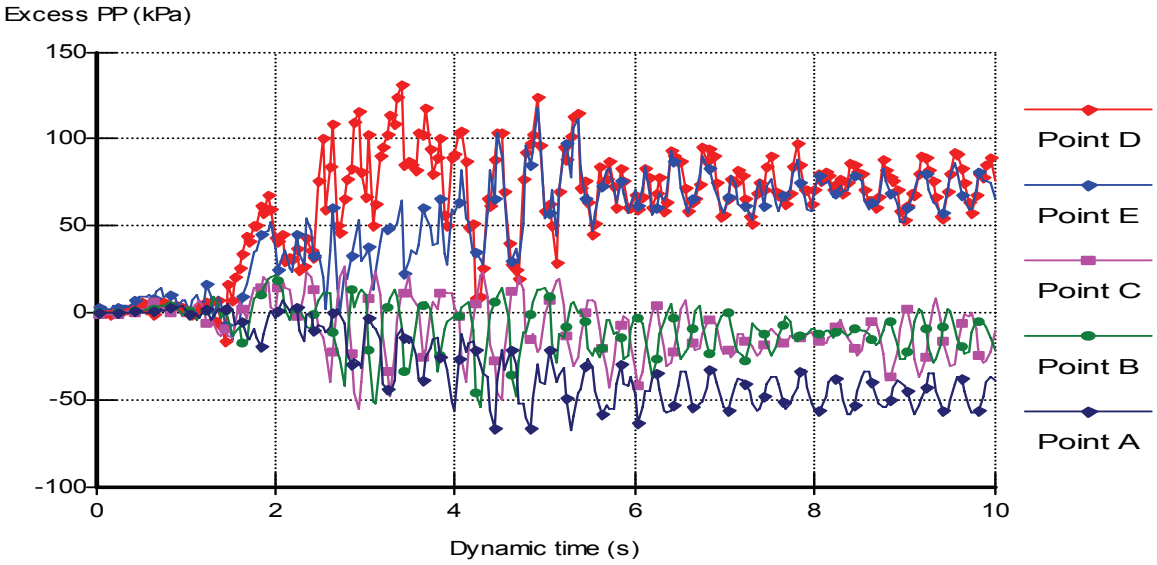

Fig. 6.32 Excess pore pressure (negative side indicates suction)

Finally, the excess pore pressures are compared in Fig. 6.32 to the selected points. Again, the legends are given in chronological order indicating the base point D with the maximum excess pore pressure. All three surface points indicate suction (negative excess pore pressure) being the highest about 50 kPa at point A, which is further away from the GWT compared to others.

- **Effect of damping in dynamic analyses**

Further, dynamic analyses of the last case study was conducted for an assumed 5% damping ratio (ζ) for the upper two soil layers. The purpose of the additional study was to observe the effect of the Rayleigh damping coefficients, which are the input parameters in the dynamic simulations. The computed damping coefficients are given Table 6.5. The computations are based on Eqs. (2.26) and (2.27) given in Chapter 2, where the terms are also defined.

Table 6.5 The computed Rayleigh damping coefficients for dynamic analyses

Layer	H (m)	V_s (m/s)	ω_1(rad/s)	ω_3(rad/s)	ζ (%)	α (–)	β (–)
p1	15	80	8.4	25.1	5	0.628	0.002
p2	35	108	4.8	14.5	5	0.360	0.005
rock	20	197	15.5	46.4	0	0	0

Few simulation results from the material damped system are verified and reviewed herewith. The shear shading was found more or less the same as in the undamped system (see Fig. 6.29). However, the displacement in the damped system (see Fig. 6.33) was found 10 -15 cm less than in the undamped system (see Fig. 6.31). Similarly, the acceleration at point A was found less.

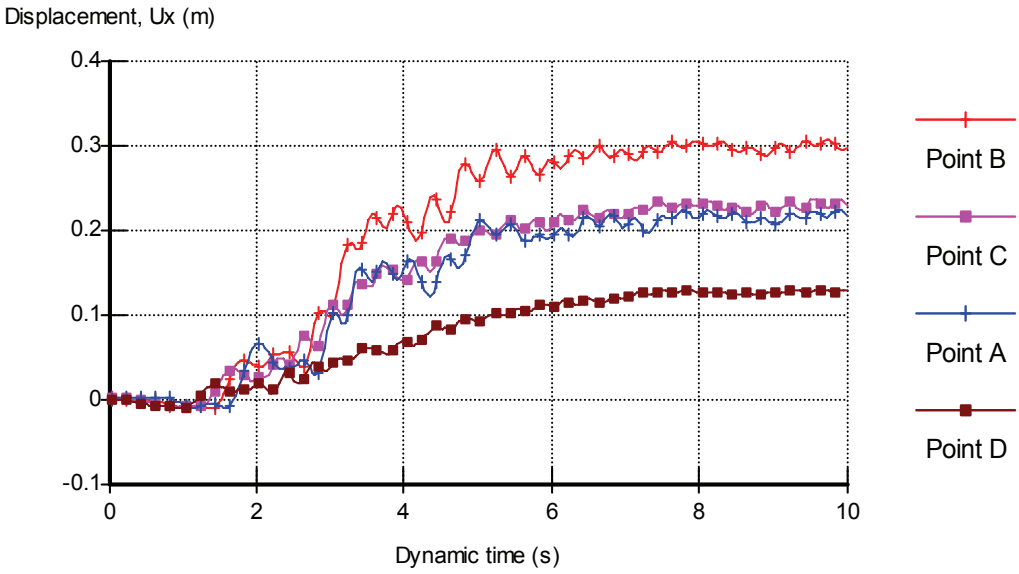

Fig. 6.33 Accumulated displacement-time series at selected points in a damped system

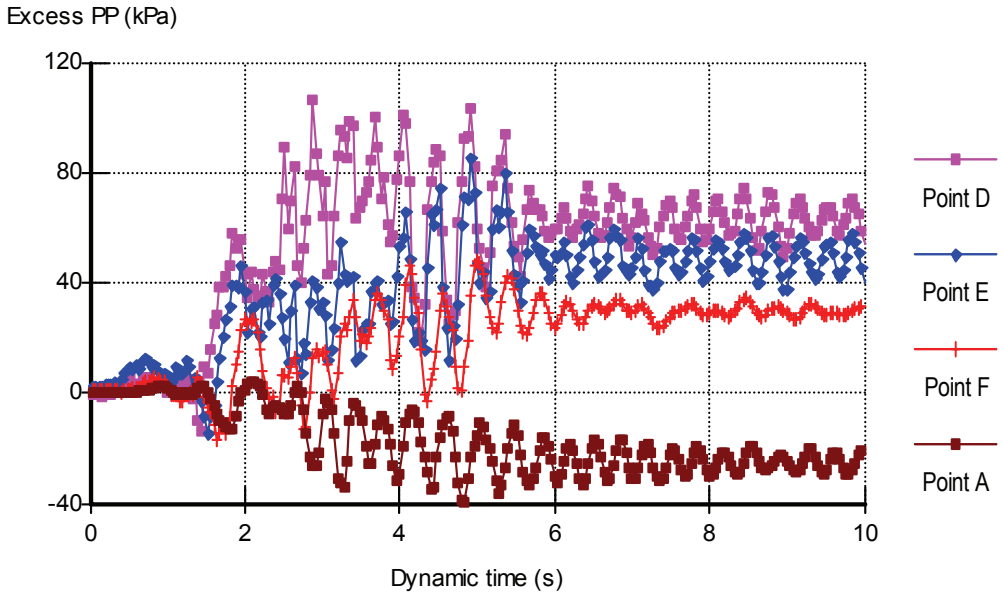

Fig. 6.34 Excess pore pressure (negative side indicates suction) in a damped system

Fig. 6.34 shows the excess pore pressure (PP) again at selected points. A point F in the p2 layer (see Fig. 6.28) was chosen. This point lies sufficiently deep inside the slope (12 m below from the ground surface) and just 1.5 m above GWT. Contrarily, the result shows excess porepressure even above the GWT. From these analyses, it can be concluded that suction may develop closer to the ground surface, but excess pore pressure can be expected deep inside the soil body, no matter where the GWT is located. The excess pore pressure at other locations was also compared with the results from earlier analyses. All surface points, which are located a couple of meters below the ground surface, were found to have a similar trend (i.e. suction), but with reduced quantity. For example, at point A, the suction was about 35 kPa in Rayleigh damped system, whereas it was found equal to 50 kPa in the undamped system.

6.2.8 Discussion on dynamic simulations

Apart from the last verification simulations with Rayleigh damping parameters, the rest of the simulations utilise zero Rayleigh damping. However, the total material damping has been covered under utilized damped Newmark method in the simulations. Some conclusions from the dynamic analyses can be drawn. First, both case study slopes indicate similar patterns of permanent displacements, accelerations and excess pore pressures, with a few exceptions. Second, the locations near the slope surface are more likely to displace permanently compared to the locations inside the soil body. The reason is that the soils can move freely close to the surface. The same conclusion is valid for the acceleration with higher amplitude on the surface.

Concerning the pore pressure, the analyses show increased excess pore pressure at the base of the model, and it decreases towards the GWT. There is no contraction close to the bottom of the model. However, the excess pore pressure may have developed because of horizontal stresses that possibly could increase in the lower layers during cyclic loading. It means that the excess pore pressure is expected to increase during undrained cyclic loading inside the soil body. The difference in excess pore pressure between two simulations at point D, see Fig. 6.21 and Fig. 6.32, can be explained by the difference in total vertical and horizontal stresses after shaking. Similarly, the simulations show increased suction closer to the ground surface. Suction may result from the dilatancy in the soil modelling of the upper layers. In addition, suction can also result from unloading, in this case stress release due to a reduction in the total horizontal stresses during shaking.

Likewise, some conclusions regarding slope stability can be brought forward. Development of suction close to the slope surface is a good sign of a stable slope. However, this conclusion is valid only if the critical SS falls within this zone. This may not be the case during or after earthquake events. In contrast, a significant increase in excess pore pressure may have the adverse effect on the stability, particularly if the critical SS falls inside the GWT. The development of positive pore pressure along the SS will result in a reduced FOS by reducing both effective normal stress and friction properties. Therefore, the stability will largely depend on the developed level of suction or positive excess pre pressure. Moreover, a high excess pore pressure may result in instability due to possible liquefaction ($\sigma_v'<0$) in the slopes. Such possibility is generally higher around the toe of the slopes.

Looking into the shear shading given in Fig. 6.18 and Fig. 6.29, the strain concentrations in the slopes indicate a weak surface, from where failure may initiate. Furthermore, animation of the simulation outputs showed plastic points floating all over the slope. The plastic points indicate that the mobilised shear stresses reached the M-C failure envelope. In addition, the soil properties may further extend towards the right side of the yield surface, which indicates the soil properties in the plastic region. Unrecoverable plastic strains are developed in the plastic region. Moreover, the soil may remain with the residual strength, which is generally lower than the peak strength.

Chapter 7

Discussion on Analysis Methods and Results

7.1 Slope sstability evaluations

Analysis of slopes has traditionally been carried out by limit equilibrium (LE) methods, which are based on the principles of static equilibrium of forces and moments. According to Fredlund and Rahardjo (1993), LE methods are important mainly because of two reasons. First, the methods have proved to be reasonably reliable in assessing the stability of slopes. Second, the methods require a limited amount of input, but can quickly perform an extensive trial-and-error search for the critical shear surface (CSS). However, Krahn (2003) says, "LE methods are missing the fundamental physics of stress-strain relationship, and thus they are unable to compute a realistic stress distribution". In spite of these limitations, the LE methods are still common in practice because of their simplicity and the reasonably accurate FOS obtained.

In recent years, finite element (FE) methods, especially the FE program PLAXIS, are becoming increasingly popular (Nordal & Glaamen 2004). The FE program PLAXIS is widely used in many European countries and its application is spreading. Today, computational software based on the FE principles are developed and frequently applied in practice. Since the FE methods are based on compatibility relationship, and thus can handle the stress-strain behaviour of soil, a more realistic stress situation can be computed. Thus, FE analyses have an advantage over LE analyses for evaluation of the stability of slopes.

7.1.1 Comparison of LE methods

The fundamental differences among LE methods are given in Capter 2, Table 2.1. As Nash (1987) states, "The significant difference among the methods is the assumptions made about the position and inclination of the interslice forces." Janbu's GPS method, for example, assumes a line of thrust where the interslice forces act, whereas the Morgenstern-Price (M-P) method assumes a variable interslice force function. Moreover, some methods compute FOS by force equilibrium (e.g. Janbu's simplified (JS) method) or moment equilibrium (e.g. Bishop simplified

(BS) method). Similarly, the advanced LE methods satisfy both force and moment equilibriums (e.g. Janbu's GPS, M-P and Spencer methods). Furthermore, the general limit equilibrium (GLE) formulation, which is a modified expression of M-P or Spencer method, provides a basis for comparison of the most common LE methods as discussed in Chapter 2, Section 2.2.9.

A comparison made by GLE procedure is illustrated in Fig. 7.1 for the circular SS analysis of the case study given in Chapter 6, Section 6.2.7. The BS and JS methods are compared with reference to M-P method for the two load cases (dry season GWT without and with pseudo-static analysis) as shown in Fig. 7.1.

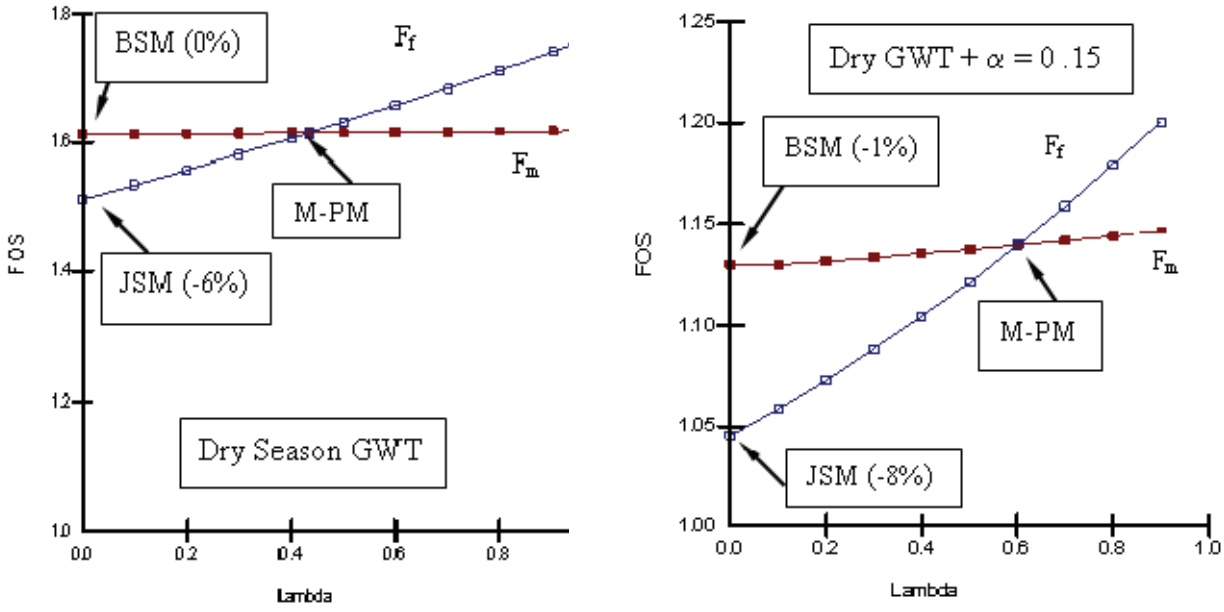

Fig. 7.1 Comparison of LE methods for circular SS analysis (powerhouse slope)

As indicated in Fig. 7.1, the FOS from BSM is found almost equal compared to M-PM. The reason is that the moment equilibrium FOS (F_m) curve is mostly unaffected for a circular SS. As Krahn (2003) says, "Generally the slope of F_m curve is found nearly horizontal for a circular SS, and for such conditions, there is no effect of the interslice force function (f(x))". This is because the whole sliding mass can rotate without any significant movement of slices. However, BSM may overestimate FOS if the external loads, for example anchors and support forces, are applied referring to Fig. 2.4b in Chapter 2. In this situation, the F_m curve will have a downward gradient. In contrast, JSM has computed 6 - 8% lower FOS compared to the FOS from M-PM. The larger difference indicates the sensitivity of the force equilibrium FOS (F_f) due to the interslice forces. A substantial amount of interslice movement is required in this case before sliding takes place.

The pseudo-static analysis carried out for the powerhouse slope (see Fig. 7.3) for an assumed plane SS shows the F_m curve as downward sloping and sensitive to the interslice shear force, whereas the F_f curve is completely independent on lambda (λ), i.e. the interslice force function.

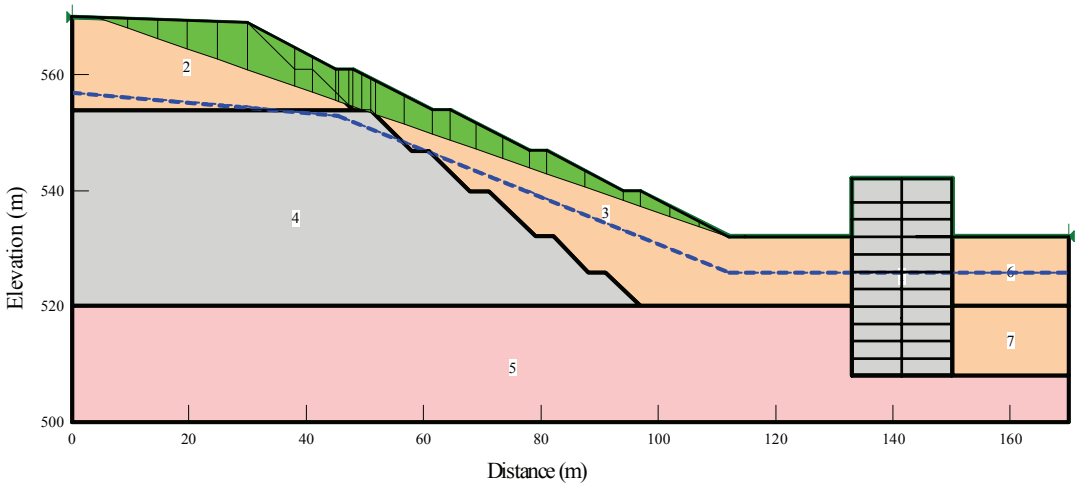

Fig. 7.2 Analysis for the assumed plane SS in SLOPE/W

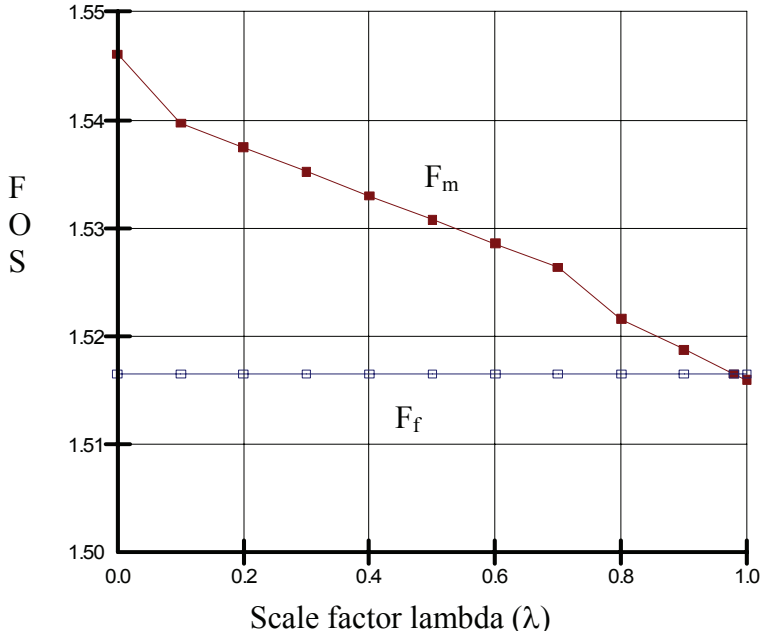

Fig. 7.3 The F_f and F_m curves after the plane SS analysis

According to Krahn (2003), reverse positions of the F_f and F_m curves are found for a plane failure in a vertical slope face compared to the circular failure (see Fig. 7.1). However, in this study of plane SS analysis, the JSM computes identical FOS to M-PM, whereas BSM over- or underestimates depending on negative or positive gradient of the F_m curve. Moreover, an assumed composite SS was also analysed (see Appendix F, Fig. F.7) and the differences were studied. As a result, the gradient of both F_f and F_m curves remains positive (see Fig. F.8), and both BS and JS methods underestimate the FOS compared to M-P method. Unlike to the results from this study, Krahn (2003) presents a negative gradient of the F_m curve for a steeper slope face. In his study, BSM computes higher FOS than M-PM.

The most common LE methods are also compared in Fig. 7.4 using the M-MP as a reference (0%). The comparison is based on the analyses for four different load cases (refer Chapter 3, Section 3.1.2) of an idealised slope, which was analysed in SLIDE for the circular SS.

As in the previous discussion, BSM computes consistent FOS with minor variations (~1 %) on the higher side, and the reason has already been discussed above. Similarly, JGM (GPS) also shows minor variations (<2 %), but on the lower side. However, both JG and M-P methods result in exactly the same FOS (not shown here) if a particular, circular SS is analysed. This indicates that both methods compute the FOS with the same accuracy. In addition, the lower FOS in JGM for the CSS identified by itself means that the method is able to search for the CSS more accurately than M-PM. Nevertheless, the marginal variations in the FOS show that both methods are equally good among the LE methods even for the individual circular SS analysis.

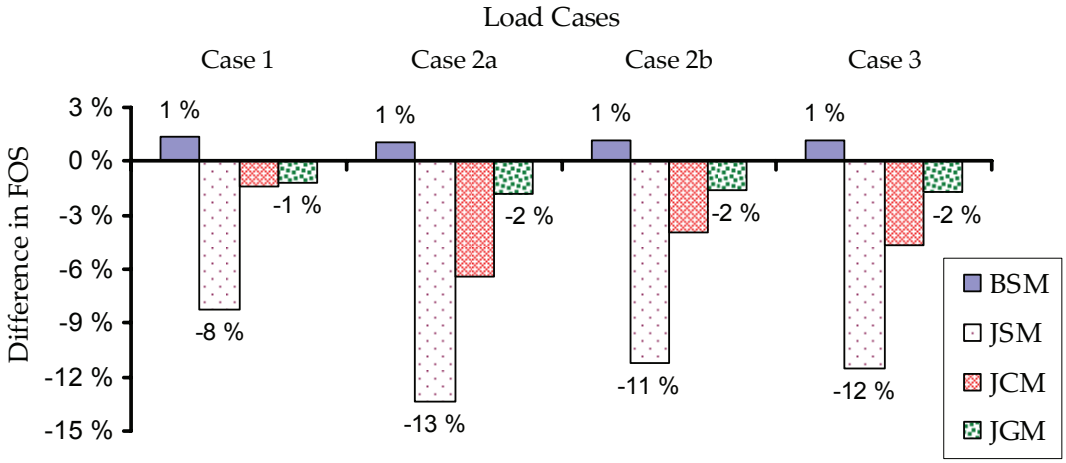

Fig. 7.4 Comparison of LE methods with M-PM (circular SS)

Likewise, JCM seems to be underestimating the FOS from 1 – 5 %, as seen in Fig. 7.4. Moreover, JSM shows the largest variation on the lower side, ranging from 8 - 13 %. Abramson et al. (2002) say, "FOS values may generally differ by ± 15 % upon comparison with the results calculated by the M-P method". In this study also, the variations are found within the range of the previous studies for CSS analysis. Moreover, the FOS from LE analysis in SLOPE/W and SLIDE are found mostly the same with a marginal variation (± 1 %) compared to the results for the same method.

7.1.2 Comparison of LE and FE analyses

As discussed above, LE and FE analyses have fundamental difference in the basic principles. The first is based on the limit equilibrium formulations, which are dependent on static force or moment equilibrium. The second is based on a stress-strain relationship, which can effectively accommodate the change in stresses. The FE analysis in PLAXIS, for example finds the CSS, where the excessive strains are localised, and computes the FOS by a c-ϕ reduction procedure for the Mohr-Coulomb soil model. In this context, the like to like comparison by the computed FOS

can reveal the inherent difference between LE and FE methods. In addition, the fundamental difference within the analysis methods explains the difference in computed results (FOS).

The FE analysis computes FOS for each element along the CSS, whereas a single, weighted average FOS is computed in the LE analyses. Moreover, Krahn (2004) states, "A dynamic FE analyses can handle variations in FOS due to ground shaking in earthquakes, without any difficulty of convergence, i.e. stress redistributions for change in loading conditions". The conversion of simulations in LE is found problematic for steep CSS, whereas FE overcomes such difficulties. This is why the computed FOS from the FE analysis is regarded as a more reliable value for the analysed slopes and hence the methods are compared accordingly.

Using the FOS computed from PLAXIS as a reference (0%), a comparison of the LE and FE methods is presented in Fig. 7.5. The FOS, obtained from the analysed for the circular SS by SLOPE/W in Chapter 3, is used for the comparison. All commonly used LE methods, except the JSM, are found to over-estimate the FOS. The smallest difference is found for the dry slope, i.e. Case 1, whereas the maximum difference occurs when the slope is in fully saturated conditions, i.e. Case 2a.

The larger difference in Case 2a indicates that LE analyses have difficulties to estimate a realistic pore pressure distribution, and further changes in the effective normal stresses along the CSS. However, the seepage analyses, i.e. Case 2b in SEEP/W, which computes the pore pressure using finite elements, have reduced the difference in FOS. This means, more accurate stresses can be computed in FE analyses than in LE analyses.

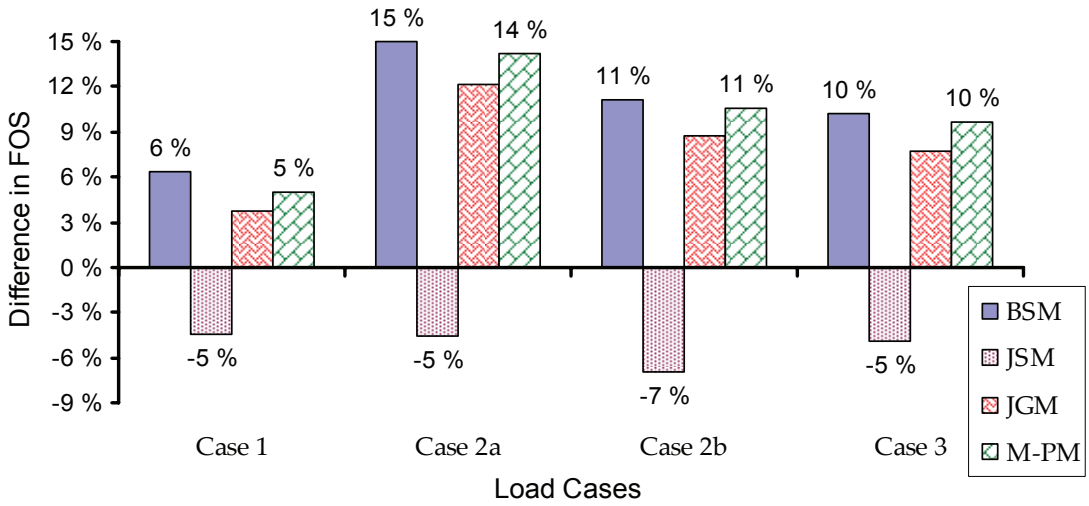

Fig. 7.5 Comparison of LE methods (circular SS) with the FE software PLAXIS

The study shows that the advanced LE (M-P) method may overestimate FOS in saturated condition as much as 14 %, which is a significant difference (see Fig. 7.5). However, the variation is quite low (5 %) for a completely dry slope. Similarly, JGM may overestimate FOS by 4 – 12 %.

In contrast, JSM may underestimate FOS from 5 – 7 %. Nevertheless, the differences in FOS may vary from case to case, and therefore, it cannot be generalised for all kinds of shear surfaces.

The reason for the difference in FOS is primarily related to the normal stress distribution along the CSS. According to a study carried out by Krahn (2004), a significant difference in normal stress distribution, particularly in the toe area, can be found between FE and LE analyses for a particular SS. This difference results in from the shear stress concentrations, which are not captured in the LE analyses, where the normal forces at the base are primarily derived from the weight of the sliding mass. Krahn (2004) further concludes, "The normal stress distribution for a deeper CSS is much closer, and thus the FOS from FE and LE analyses is not much different". Janbu (1973) also suggests studying the shear stress concentrations in critical zones by using a stress-strain relationship, instead of the LE equations. These widespread experiences highlight the computational difficulty of a realistic stress distribution, which can be more precisely computed by the modern FE analyses.

Several others have also experienced the limitations of the LE methods. As Chowdhury (1978) states, "It is difficult in LE analysis to evaluate the interslice forces, which depend on a number of factors including the stress-strain and deformation characteristics of the materials in the slope". Likewise, Nash (1987) comments as follows, "LE methods are not well situated to the analysis of dynamic stability of slopes, for example, debris flows and slopes under earthquakes loading". Thus, the dynamic effects on the pore pressure distributions and shear strength parameters are difficult to model in LE methods. In this study also, no similarity in the interslice forces, line of thrust and critical shear surface was found compared to the analyses in LE and FE methods given in Chapter 3, Sections 3.3.3.2 and 3.3.3.3. These parameters may have influenced the FOS in the analysis.

7.2 Stability conditions of the case study slopes

Two case slopes from Nepal were analysed for various static and dynamic conditions in order to evaluate the critical conditions in the slopes. The detailed stability analyses have been presented in Chapter 6, where detailed discussions on the computed FOS can be found. However, the stability conditions of these case slopes are also briefly discussed in the following sections.

7.2.1 Case study: Dam site LB slope

The summary of the computed FOS is presented in Fig. 7.6. The slope was analysed by both LE and FE methods for various load and groundwater conditions. The LE (SLOPE/W and SLIDE) analyses are based on circular SS and the presented FOS is related to M-P method. The FOS from SLOPE/W and SLIDE is quite comparable, except for those obtained according to the seepage analyses. However, PLAXIS has computed slightly lower FOS, and the reasons for this have been discussed above. The FOS from seepage analysis in SLIDE and SLOPE/W has disagreement as indicated in Fig. 7.6. The reason is the low effective stress due to the CSS,

which is located near the toe of the slope, compared to the CSS obtained in SLOPE/W (refer Chapter 6, Section 6.2.6.3).

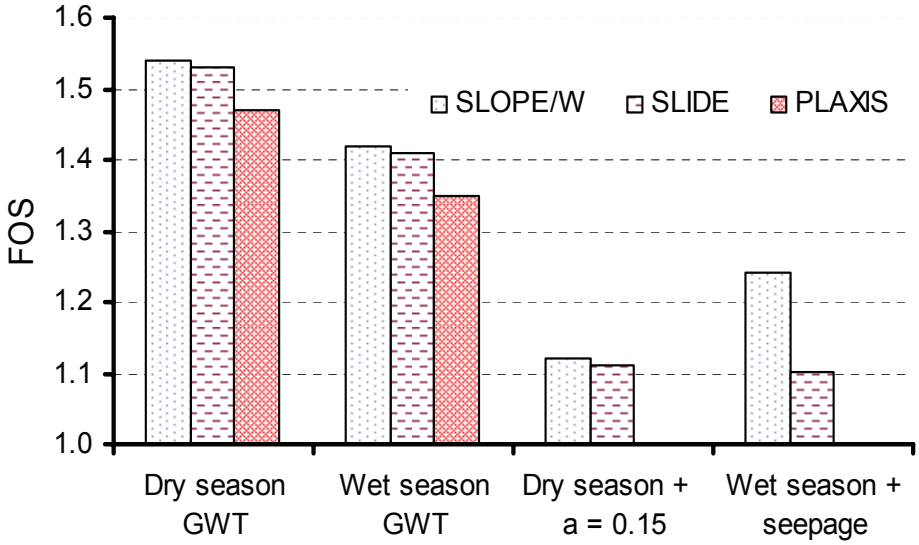

Fig. 7.6 FOS computed by three software programs for the dam site slope

The computed FOS, which are compared in Fig. 7.6, shows that the case slope is stable for all seasonal conditions. However, the last two cases (read a = α_h) indicate that the slope may have critical condition as identified by PLAXIS (F = 1.0). The CSS in FE analysis is found slightly non-circular (i.e. composite) compared to LE analysis. In contrast, a circular CSS is automatically searched for and analysed by the LE (SLOPE/W and SLIDE) software. However, a stability analysis for a composite SS is possible in the LE based software for a user defined SS, which may not necessarily be the critical one.

The seepage analyses indicate that toe of the slope may have critical conditions in the monsoons. The analysis further shows that any pressure relief measure around the toe of the slope will have significant improvement in the FOS (see Fig 6.13, Chapter 6). In addition, well-functioning horizontal drains in the slope will have a positive contribution on FOS.

The dynamic analyses of the case slope show that larger permanent displacements may result close to the surface, indicating a critical condition during earthquakes (see Fig. 6.19, Chapter 6). Similarly, earthquakes may generate suction above the GWT and increased pore pressures below it, as indicated in Fig. 6.21. The soils in the slope may approach to plastic limit due to the dynamic shaking. This indicates that the strength of the soil will be fully utilised if such an earthquake event occurs. In addition, earthquakes may correspond to the undrained triaxial condition, in which the maximum shear strength attains at low axial strain levels, referring to the triaxial test results given in Figs. 5.10 and 5.11, Chapter 5. The significant strain softening beyond the peak strength, and considerable reduction in shear strength at large strains, are both indicators of unstable conditions. Elaborated discussions on the dynamic simulations have been already presented in previous Section 6.2.8.

7.2.2 Case study: Powerhouse slope

As in the previous case study, the FOS for three load cases are summarised in Fig. 7.7 for the powerhouse slope. The computed FOS in LE (SLOPE/W, SLIDE) analyses is based on the M-P method, and the FOS can be compared to the results from PLAXIS analyses.

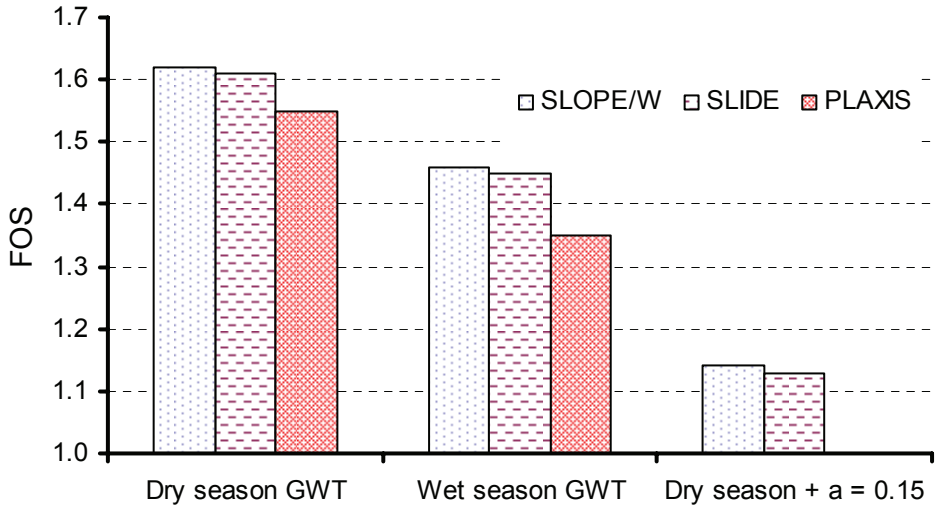

Fig. 7.7 FOS computed by three software programs for powerhouse slope

The FOS from the PLAXIS analyses is found higher than unity, but slightly on the lower side compared to LE analyses for the first two load cases. However, pseudo-static analysis in PLAXIS (read a = α_h) shows the equilibrium state and hence does not appear in Fig. 7.7.

As in the previous case study, the comparison of FOS shows that both the LE based software SLOPE/W and SLIDE compute almost identical FOS in all conditions. However, a slightly higher FOS from LE analyses can be seen compared to the FE analyses. Moreover, a higher FOS than the minimum required value defined for various conditions (normal F>1.5, earthquake F>1.05), indicates that the slope will remain stable for all seasonal conditions. However, the FE analyses indicate that the slope may reach to the limiting equilibrium condition. As studied in Chapter 3 (see Section 3.3.3.1), the FOS can be increased by application of a positive dilatancy angle (ψ) in the FE analysis. The analysis utilises a small dilatancy angle in the p1 layer (see Table 6.1 in Chapter 6). According to the literature, overconsolidated slopes in silty sand materials may however show significant dilatancy behaviour.

Seepage analyses by locating the wet season GWT shows considerably low FOS (see Fig. E.7, Appendix E). The reason is the reduction in normal effective stress and corresponding effect on the shear strength properties of soils. However, the application of horizontal drainage systems increased the stability close to the equilibrium state (see Fig. E.8). Similar to the previous case study, the slope was found unstable, particularly in the lower parts. However, the FOS can significantly be increased by utilising the lowered pressure at the toe as indicated in Fig. 6.26, Chapter 6. Thus, the seepage analysis shows that lowering of the GWT at the toe is highly

recommended. The GWT regime may differ at the toe after regrading of the slope. Even if there is uncertainty about the GWT at the toe, the stability situation will not be much different from the present analyses with respect to the seepage conditions.

On one hand, the dynamic simulations carried out in PLAXIS indicate a similar risk as in the previous case study. The reasons are the shear strain development, permanent displacement and high acceleration close to the surface. Moreover, substantial amounts of plastic points were observed in animation as in the previous case study slope. However, the suction observed close to the surface may improve stability, if the suction appears close or at the CSS.

On the other hand, the p2 material with the dominating percentage of calcite (81 %) has different properties than others. A brittle behaviour at failure was revealed in the undrained triaxial shearing (see Fig. 5.13). The dynamic earthquake events may resemble an identical situation as in the undrained triaxial test, which indicates the significant strain softening after 1 % axial strain. However, earthquake exerts a dynamic loading, whereas the strength parameters are referred to a static loading in triaxial testing. In addition, pore pressure increases and thus, the shear strength nullifies at around 5 % axial strains in undrained conditions (see Fig. D.1, Appendix D). These features indicate that instability conditions may appear during earthquakes. However, the probability of failure may be reduced by installing some pressure release measures at the toe area. This will reduce a possible risk of liquefaction around the slope base.

7.2.3 Investigated strength parameters

Broadly speaking, the slope stability evaluations are irrelevant unless proper input parameters are utilised in the computations. Many authors have highlighted the importance of the quality of the input parameters. For example, Janbu (2001) states, 'The shear strength of subsoil has to be known before the analysis can be performed'. Likewise, Nash (1987) points out, 'The soil properties and groundwater conditions including others are the principle sources of uncertainty in slope stability.' Thus, the investigation of relevant soil parameters is a vital work prior to perform slope stability evaluations.

Accordingly, full-scale laboratory investigations from index tests to the advanced triaxial tests were carried out in this study. An emphasis was given to investigate the effective shear strength parameters for the case study slopes. The specimens were built-in from the representative soil samples taking the reference to the index properties obtained from the Standard Proctor test. Moreover, some of the index properties were verified later by in situ laboratory testing, and only marginally different results were found compared to the Standard Proctor test (see Table 5.2 in Chapter 5). Therefore, the specimens for permeability and triaxial tests were built-in based on the maximum dry density found by the Standard Proctor tests.

Though attempts were made to saturate the triaxial specimen by applying backpressures, the recommended B-value was not possible to attain for the well-graded silty sand materials. To increase saturation level, the specimens were thus built-in at slightly lower dry density than the

Standard Proctor maximum dry density (see index properties in Appendix C, Section C.4). However, this attempt was also not sufficient to get full saturation as recommended. Accordingly, the shear strength parameters were determined. The recorded B-values are given in Section C.4. In the previous studies carried out by other researchers, the use of CO_2 was tried without satisfactory results.

- **Shear strength affecting parameters**

The previous studies carried out for silty clay and silty soils show that shear strength parameters are dependent on the density of the specimen, the moisture content and degree of saturation (see Appendix H, Figs. H.1 - H.3). According to Andrei et al. (2001), a dense specimen will have higher cohesion than a medium dense specimen will at a lower moisture content level, as indicated in Figs. H.1 and H.3. Their study further shows that friction angle decreases as the water content increases in the soils. However, the study further indicates that friction angle is independent on the dry density, i.e. porosity of the specimen. Thus, a higher strength in dense soils can be found at a low moisture content level. Contrarily, both strength parameters show a decreasing trend in saturated conditions even if the density remains constant. This is (one of) the reasons why the slope failure occurs at the increased saturation stage.

Another study, carried out by Melinda et al. (2004) in direct shear tests, conducted for sandy lean clay materials (49 % of sand, 25 % of silt and 26 % of clay), shows that cohesion becomes higher due to the increased suction, whereas the friction angle is almost constant. The conducted direct shear tests results are presented in Appendix H (see Fig. H.4). The tests were carried out for both wetting and drying cycles with varying matric suction. The specimens were compacted at 2.0 g/cm^3 of dry density almost same as in the present study. Their study further shows 13 kPa of cohesion and 30^0 of friction angle at zero suction (fully saturated condition). The partial saturated specimens in the present study may have small suction, and thus the cohesion parameter may have been theoretically on the higher side. However, the investigated cohesions were found in low range (5 – 10 kPa in undrained triaxial tests and 10 - 13 kPa in drained triaxial tests). Moreover, even if the B-values showed lower saturation level, the test results were found closer compared to the previous full-saturated advanced triaxial tests (see Fig. 5.12, Chapter 5). Even the cohesion of 20 kPa was found in one of the previous tests (see Fig. 4.8, Chapter 4). In supports that the investigated cohesion represents the true value even if the B-values were recorded lower than recommended ones.

- **Dilative behaviour**

Dilative behaviour in soils is related to the plastic volumetric strains increments. As Bolton (1986) states, "Dilatancy in sand depends on density and on the friction angle". According to Nash (1987), overconsolidated materials tend to dilate on shearing and the shear strength reaches a peak at small strains. Even if the built-in specimens did not reveal the dilative properties, i.e. volume increase during shearing in the triaxial tests, the overconsolidated case slopes may have this property in situ. Since the present stability evaluations utilise very small

dilatancy, higher value will increase the FOS. It is noteworthy that the dilatancy can only be used for soils showing volume expansion in drained shearing, such as sand or silty sand or OC-clayey soils.

7.2.4 Additional analysis considerations

Present stability evaluations of the case study slopes are based on common analytical approach, in which the negative pore pressure (suction) above the GWT is ignored. As Fredlund (1987) states, 'It is a reasonable assumption to neglect suction for many situations where the major part of the CSS passes through a saturated soil'. According to the principles of saturated soils, the applied LE and FE analyses utilise the saturated shear strength parameters, which have been discussed in previous Section 7.2.3. Moreover, heavy rainfall occurs in the case study area from June to July (see Chapter 4, Section 4.5) and there is hence a high possibility of a diminished suction in the unsaturated zone during the monsoon period. This explains the reason of suction, being a temporary feature, and it generally is neglected in slope stability evaluations.

Actually, the approach of neglecting the suction results in a conservative FOS. Therefore, for situations where the GWT is deep, or a shallow failure occurs above the GWT in the partially saturated zone, the stability of slopes are better analysed using an assumption of unsaturated soils. Accordingly, the effect of suction is incorporated in the extended Mohr-Coulomb failure criteria and the shear strength at failure as proposed by Fredlund (1987) is given by:

$$\tau_f = c' + (u_a - u_w)\tan\phi^b + (\sigma_n - u_a)\tan\phi' \qquad (7.1)$$

where,

τ_f = shear strength of unsaturated soil at failure

c′ and ϕ′ = effective cohesion and internal friction angle,

σ_n = normal stress

u_a = pore-air pressure

u_w = pore-water pressure

$(u_a - u_w)$ = matric suction at failure

ϕ^b = angle indicating rate of increase in shear strength relative to the matrix suction (~15^0)

Shear strength of soil relies on the effective stresses, whatever is the condition of drainage. The suction results in positive effective stresses and hence increases the shear strength of the soil (Nash 1987). Thus, the suction above the GWT will have additional improvement in FOS, if the investigated parameters are utilised in the analyses.

The steep slopes encountered in tropical regions, for example in Nepal, are capable of maintaining the stability due to the suction effects in the dry season. The soils are typically in an

unsaturated state with negative pore-water pressure since the groundwater tables in steep slopes are often deep. Many slopes that are stable in dry seasons become unstable just at the middle or at the end of the wet (monsoon) seasons. The loss in suction is the main reason of the majority of slope failures just after the monsoon. As saturation is reached due to the rainfall infiltration and rise in GWT, the pore-air pressure becomes equal to the pore-water pressure (i.e. $u_a = u_w$), and thus, the last term in Eq. (7.1) disappears resulting to the lower shear strength.

Nevertheless, the suction existing above the GWT may be utilised in the design if the applied suction level in analysis can be maintained by some means all the year round. This is an interesting topic for further research, which requires special equipment to measure suction in laboratory and control the similar conditions in the field.

Moreover, the present study covers the 2D-analyses of slopes for a circular SS in LE analyses and a composite SS in FE analyses. A large number of previous studies show that the 3D-analysis of slopes gives greater FOS than the 2D-analyses (Duncan 1996). In fact, the 3D- analyses of slopes were based on the curved SS, with loads in a limited extent and a constrained failure surface by physical boundaries. The conclusion from those studies was particularly valid for the circular SS and the 2D-analysis carried out for the most critical section of a slope. However, as Hutchinson and Sharma (1985), and Leshchinsky and Baker (1986) pointed out, the 2D- and 3D-analyses should give the same FOS for slopes in homogeneous cohesionless soils, because in such soils, the SS is usually a shallow plane parallel to the surface of the slope. Furthermore, Azzouz et al. (1981), and Leshchinsky and Huang (1991), noted that if 3D effects are neglected, the back calculated strength parameters (from 2D-analysis) will be too high (Duncan 1996). Further application of the calculated strength parameters in 3D-analysis gives the FOS greater than unity, and if so the slope would never have failed. Back analysis means the analyses of previously failed slopes, where the FOS is less than unity. This indicates a considerable 3D effect on FOS. Moreover, the stability analyses with 3D considerations not only increase the FOS and optimise the design, but substantial resources can be saved if the reliable input parameters are investigated and applied in the analyses.

The performed dynamic analyses for the case study are based on the undamped vibrations, except for the latter few results given at the end of Chapter 6. For such vibrations, the term of the damping matrix in Eq. (2.24) (given in Chapter 2) is zero (Kramer, 1994). However, the damped Newmark method with the applied coefficients ($\alpha = 0.3025$ and $\beta = 0.6$) considers an artificial damping even if Rayleigh damping is neglected. Moreover, the consideration of undamped Rayleigh system resulted in a conservative solution. In reality, soils will have certain damping property. Therefore, dynamic analysis should be performed using proper damping ratios (ζ), which can be determined experimentally by a resonance column test. The damping ratio (ζ) depends on plasticity index (PI) and cyclic shear strains. According to Vucetic and Dobry (1991), the soil with lower PI will have higher damping ratio and vice versa at the same cyclic shear strain. In their study, for example, if PI = 0, the value of ζ can be as high as 24 %, whereas at PI = 100, the value of ζ can be reduced down to 10 % at 1% cyclic shear strain.

Chapter 8

Conclusions and Recommendations

8.1 Conclusions

Today, the two approaches of stability analyses, one based on limit equilibrium (LE) formulations and the other based on finite element (FE) principles are widely used in practice. The basic physics of stress-strain relationship, which is lacking in LE methods, has been well covered by the FE methods. As a result, complicated geotechnical computations can easily be performed. In addition, FE analysis can simulate stress concentrated problems and deformation compatibility, which have been experienced problematic in LE analysis. This has been one of the advantages of FE calculations. On the other hand, LE methods have been applied for many years. Hence, they are well-established and common in practice. User-friendliness, simplicity and relatively good FOS for a particular case are the advantages of the LE methods.

The scope of this study was to compare various stability evaluation methods. Accordingly, most common LE approaches were compared with the advanced LE (M-P) method. Similarly, the differences in FOS computed from LE and FE analyses were compared based on a simple slope considering various load cases. In addition, two real slopes in a case study were analysed for the recorded minimum-maximum GWT, pseudo-static and dynamic conditions. Moreover, the stability evaluations of these slopes were based on both LE (M-P) and FE (PLAXIS) calculation approaches, which both utilised shear strength parameters from advanced triaxial tests. Similarly, Mohr-Coulomb model was applied in both approaches. The following conclusions are hence derived based on the reported work on both idealized and real slopes.

8.1.1 Evaluation of the analytical methods

The conclusions are mainly based on the circular SS analyses. However, plane SS and composite SS were analysed in SLOPE/W for one of the case studies, as an additional comparative study.

The main findings from the studies are summarised as follows for the application of LE methods.

- The simplified Bishop (BS), generalised Janbu (GPS), Morgenstern-Price (M-P) and Spencer methods yield in most cases identical FOS for circular SS without any external loads on the slopes. However, the simplified Janbu (JS) method may underestimate the FOS from 8 - 13 % for the circular CSS obtained by this method.
- The JS, GPS and M-P methods result in the same FOS for plane SS without any external loads. However, the BS method either over- or underestimates the FOS for the plane SS.
- The GPS and M-P methods compute identical FOS for composite (non-circular, i.e. partly circular and partly plane) SS analysis. In addition, both methods were found computing the same FOS for a particular circular SS.
- The M-P method, or general limit equilibrium (GLE) procedure, is recommended to use in any kind of SS analyses, including external forces, unless FE methods are available.
- The FOS computed from force equilibrium methods (e.g. JS) is sensitive to the interslice force function (f(x)), one exception occurs for plane SS analyses. Similarly, the FOS computed from moment equilibrium methods (e.g. BS) is sensitive to the f(x), except for circular SS analyses. Moreover, the sine function used for interslice shear force computation is inappropriate, particularly for computation of interslice shear forces at the toe and crest areas of the slopes.
- The two LE based software, SLOPE/W and SLIDE, compute identical FOS within ± 1% variations compared with method to method except in seepage analyses. Otherwise, both software programs are found reliable for slope stability evaluations. Moreover, SLIDE has both groundwater calculation feature (seepage analysis) and slope stability analysis, i.e. two-in-one package, whereas SLOPE/W requires separate software, such as SEEP/W for seepage analysis.

Similarly, further conclusions are derived from the comparative study between the LE based software (SLOPE/W and SLIDE) and the FE based software (PLAXIS). The comparative studies were made using the PLAXIS calculations as reference. This program searches for the CSS and computes the effective base normal stress utilising the stress–strain relationship, also for non-circular geometries.

- All LE methods, except the Fellenius (Ordinary) and JS methods, estimate higher FOS than FE analysis in PLAXIS. The JS method may underestimate FOS from 5 – 7 % compared to FE. However, the correction factor applied in JS method (i.e. JCM) computes almost identical FOS compared with the FE analysis.

- The most rigorous M-P method or GLE procedure may overestimate FOS with as much as 14 % in fully saturated slopes with hydrostatic porepressure distributions. However, the overestimation may drop as low as 5 % for dry slopes.
- The FE methods are best suited for external loads, complicated geometry and more realistic normal stress distributions and resulting FOS. Hence, the FE analysis is recommended to use in stability evaluations with investigated relevant soil parameters.
- The pore pressure distribution from seepage analyses in PLAXIS are found comparable to those obtained in SEEP/W and groundwater calculations in SLIDE using a finite element approach. Even in this case, the LE (M-PM) analysis may overestimate FOS as high as 11% compared to the FE analysis.
- Where appropriate, application of a positive dilatancy angle ($\psi = \phi - 10^0$) in the FE analysis may improve the FOS in the range of 4 – 10 % depending on the pore pressure conditions. Similarly, the analyses with optimisation (slightly non-circular SS) in SLOPE/W (M-PM) and with the application of ψ in PLAXIS may result in the identical FOS. However, the difference in FOS between LE (M-PM) and FE analyses may sometimes rise to moderate variations (<5 %) even if these parameters are considered.
- The interslice forces, line of thrust and the base normal stresses are not identical in FE and LE analyses, which explain the differences in FOS computed from LE and FE methods in these studies.

8.1.2 Application of the analytical methods

In addition to the FE software (PLAXIS), the LE software (SLOPE/W and SLIDE) with the selected BS and M-P methods were utilised for the case stud slopes from Nepal. Based on the analyses, which studied mainly the effect of groundwater variations, seepage analyses, pseudo-static and dynamic earthquakes, the following conclusions are made.

- Both SLOPE/W and SLIDE software is found computing identical FOS for the selected M-P method even for various load combinations and complicated slope geometry. Concerning the particular case study, the slopes are found stable for all seasons, and will remain stable unless the GWT or other destabilising forces are increased. The conclusion is based on the analyses utilising the recorded GWT, which are expected as low as possible, even in the wet season, due to the installed drainage system. Any fault or blockage in the drainage may decrease the stability of the slopes.
- Stability evaluations by using the pore pressure distribution from seepage analyses indicate that the toe of the case study may have critical conditions in wet seasons. Further analyses of the particular case study, using a sub-surface horizontal drainage

system, indicate an improved FOS. Similarly, significant improvement in FOS was found due to the introduction of pressure relief wells around the toe of the slopes. Based on these findings from the research study, it is concluded that the toe of a slope in general is the most critical part in the wet season concerning the seepage. Considering the particular case study, any measures carried out to lower the pore pressures, especially around the toe of the slope, will have substantial improvement in the FOS.

- Limited to the case study, it is concluded that the slopes are found stable from the pseudo-static analyses, using the recommended horizontal seismic acceleration (α_h = 0.15g) from the LE methods. However, FE analyses indicate that both case study slopes may reach critical conditions during earthquake events.
- Based on the dynamic analyses, it is concluded that the crest of the studied slopes may be permanently displaced some centimetres, and thus may have critical conditions. Moreover, the unusual properties of p2 material in the powerhouse slope were investigated in the undrained triaxial tests, which may simulate the conditions during the earthquake events. Among them, a significant strain softening behaviour (at ~1 % axial strain) and zero shear strength (at ~5 % axial strains) may initiate critical conditions during earthquakes. However, the worst-case scenario, which assumes the acceleration across the river and out of the slopes, was used in both pseudo-static and dynamic earthquake analyses. This condition may not necessarily appear during earthquakes.
- The computed FOS herein may be the absolute minimum, since the analyses neither utilise the suction in the unsaturated SS above the GWT, nor consider higher positive dilatancy parameter, which can be expected in the stiff, overconsolidated materials in the natural slopes. Moreover, the 3D analysis effect, as commented on by e.g. Duncan (1996), should also be considered, resulting in an additional improvement in the FOS.

8.2 Further research and recommended works

The stability evaluations of the case study slopes utilise the common analytical approach based on the principles of saturated soils. This approach is realistic for the slopes where the majority of the CSS falls within the saturated zone. However, for situations where a failure occurs above the GWT in the partially saturated zone, the stability of slopes are better evaluated using an assumption of unsaturated soil. The advantage of such analysis will have both cost effective solution and advanced understanding of the suction contribution in the slope stability.

Similarly, the studies of 3D-slope stability analyses show better FOS than in 2D-analyses (Duncan 1996). Therefore, such studies not only increase the FOS and optimise the design, but substantial saving on resources can also be assured with reliable input parameters in the analyses. Within these perspectives, further studies on the following areas are recommended:

- Further research on slope stability analysis in unsaturated soils is recommended, focusing on particular measures that can increase or maintain suction during rainfall infiltration. In this respect, in situ and laboratory investigations for suction measurements, and the measurements of the additional strength parameters (e.g. u_a and ϕ^b) are most essential for subsequent stability evaluation in unsaturated slopes.
- 3D-slope stability analyses are recommended to compare the FOS obtained from 2D-analyses, which are generally considered providing conservative results (i.e. low FOS). With the expected higher FOS in 3D-analyses, a cost-effective steeper slope may be designed maintaining adequate stability.
- A detail study on dynamic response is recommended by conducting resonance column test for site-specific damping ratio (ζ). The performed dynamic analyses utilise mainly undamped force vibrations except the last verification analyses. The Rayleigh undamped condition was found resulting in conservative solutions especially at the surface, where large acceleration - time series and more permanent displacements have been observed. Therefore, further research on this area will have additional advantage.

Particularly focusing on the case study slopes, the following remedial measures are recommended for the improvement of the stability in critical conditions, like monsoons and earthquakes. The recommended measures may be useful also for general slopes if these conditions are found as critical events.

- Since, the lowering of the GWT at the toe of the slopes was found providing substantial improvement on FOS, such installations are strongly recommended to keep the slopes stable in critical conditions. This applies to both case study slopes.
- Plantation of vegetation will not only control surface erosion and reduce rainwater infiltration, but also maintain suction in the unsaturated part of the slopes during the monsoons. It is therefore strongly recommended to continue such measures in the slopes.
- Additional instrumentations, for example inclinometers or tiltmeters and in situ suction measurement systems are recommended to install for future monitoring and evaluations of the stability conditions.

List of References and Literatures

List of References

1. Abramson, L. W., Lee, T. S., Sharma, S., and Boyce, G. M. (2002). *Slope Stability Concepts*. Slope Stabilisation and Stabilisation Methods, Second edition, published by John Willey & Sons, Inc., pp. 329-461.
2. Al-Khafaji, A. W. and Andersland, O. B. (1992). *Soil Compaction*. Geotechnical Engineering and Soil Testing, Saunders College Publishing, pp. 113-131, 486, 559.
3. American Society for Testing Materials (ASTM) D2487-90 (1992). *Standard test methods for classification of soils for engineering purposes*. ASTM Standards, Vol. 04.08, Sec.4, pp. 326-36.
4. Andrei, S., Antonescu, I., Manea, S. and Paunescu, D. (2001). *Guide for using the systematization, storing and predicting the geotechnical parameters*. Technical University, Bucharest, (in Romanian).
5. Aryal, K. Sandven, R. and Nordal, S. (2005). *Limit Equilibrium and Finite Element Methods*. Proc. of the 16th Int. Conf. on Soil Mech. and Geotech. Engineering, 16 ICSMGE, Osaka, Japan, pp. 2471-76.
6. Aryal, K. and Sandven, R. (2005). *Risk evaluation of a slope and mitigation measures*: *A case study from Nepal*. Proc. of the 11th Conf. and field trip on Landslides. Landslides and Avalanches, ICFL 2005, Norway, pp. 31-36.
7. Aryal, K., Rohde, J. K. and Sandven, R. (2004). *Slope Stability, Stabilization and Monitoring: A Case Study from Khimti Power Plant, Nepal.* Int. Conf. on Geosynthetics and Geoenvironmental Engineering, ICGGE – 2004, Bombay, India, pp. 100-05.
8. Athanasiu, C. (2005). *Discussions on influencing factors on shear strength parameters*. Norwegian University of Science and Technology, Trondheim.
9. Azzouz, A. S., Baligh, M. M., and Ladd, C. C. (1981). *Three dimensional stability analyses of four embankment failures*. Proc., 10th Int. Conf. on Soil Mech. ad Found. Engg., A. A. Balkema, Rotterdam, The nederlands, 3, pp. 343-46.
10. Bathe, K. - J. (1996). Finite element procedures. Prentice Hall.
11. Bishop, A. W. and Henkel, D. J. (1962). *The measurement of soil properties in triaxial test*. Eward Arnold, London, p. 228.
12. Bishop, A. W. (1955). *The use of slip circles in stability analysis of slopes.* Geotechnique, Vol. 5 No. 1, pp. 7-17.
13. Bolton, M. D. (1986). *The Strength and Dilatancy of Sands.* Geotechnique, Vol. 36 (1), pp. 65-78.
14. Brauns, J. (2000). *Additional comments upon site visits*. Middle Marsyangdi Hydroelectric Project, Nepal, Geotechnical report.

15. Chaney, R. and Mulilis, P. J. (1978). *Suggested method for soil specimen remoulding by wet raining*. ASTM Geotechnical testing Journal, Vol. 1, No. 2, pp. 107-08.

16. Chowdhury, R. N. (1978). *Slope Analysis*. Developments in Geotechnical Engineering Vol 22, pp. 137-53.

17. Chugh, A. K. (1986). *Variable Interslice Force Inclination in Slope Stability Analysis*. Soils and Foundation, Japanese Society of SMFE, Vol 26, No. 1, pp. 115-21.

18. Coduto, D. P. (1999). *Geotechnical Engineering Principles and Practices*. Price Hall, upper Saddle River, NJ 07458, pp. 464-517.

19. Corps of Engineers (1970). *Slope Stability manual*. *EM 1110-2-1902*, Washington, DC: Department of the Army, Office of the Chief Engineers.

20. Consulting Engineers Salzgitter (CES) GmbH, (2005): *Hydropower / Hydroelectric Schemes* (PDF). Middle Marsyangdi Hydroelectric Project, Nepal. Nepal Electricity Authority, Durbar Marg, Kathmandu. http://www.ces.de/05/01/22-9901e-c.pdf.

21. Das, B. M. (2002). *Soil Mechanics Laboratory Manual*. Sixth Edition, Published by Oxford University Press.

22. Das, B. M. (1995). *Fundamentals of soil dynamics*. Elsevier, University Press.

23. DeGroff, W., Donaghe, R., Lade, P. and Rochelle, P. L. (1988). *Correction of Strength for Membrane Effects in Triaxial Test*. Geotechnical Testing Journal, ASTM, Vol. 11 (1), pp. 78-82.

24. Department of Hydrology and Meteorology (DHM) (2004). *Rainfall recordings data in Lamjung Distsrict*. Babar Mahal, PO Box 406, Kathmandu Nepal.

25. Deoja, B. B. (2000). *Mountain roads developments in Nepal*: Engineering geological concerns. Journal of Nepal Geological Society, Vol. 22, p. 167.

26. Dixit, A. M., Samant, L. D., Nakarmi, M., Tucker, B. and Pradhang, S. B. (1999). *The Kathmandu Valley Earthquake Risk Management Action Plan*. Published by National Society for Earthquake Technology, Nepal and Geohazards International, USA.

27. Duncan, J. M. (1996): *State of the Art: Limit Equilibrium and Finite Element Analysis in Slopes.* Journal of Geotechnical Engineering, Vol. 122 (7), pp. 577-96.

28. Edgers, L. and Nadim, F. (2004). *Rainfall induced slides of unsaturated slopes*. Landslides Evaluations and Stabilization. Proc. of the 9th Int. Symp. on Landslides, Rio De Janeiro, Vol. 2, p. 1091.

29. Emdal, A. (1994). *Setninger*. Kompendium I, Geoteknikk, Institutt for Geoteknikk, NTH (In Norwegian), pp. 94-96.

30. Fellunius, W. (1936). *Calculations of the Stability of Earth Dams.* Proceedings of the Second Congress of Large Dams. Vol. 4, pp. 445-63, Washington D. C.

31. Fredlund, D. G. and Rahardjo, H. (1993). *Slope Stability*. Soil Mechanics for Unsaturated soils. Wiley: pp. 320-45.

32. Fredlund, D. G. (1987). *Slope Stability Analysis Incorporating the Effect of Soil Suction.* Slope Stability, Chapter 4. M. G. Andersen and K. S. Richards, Eds. New York: Wiley, pp. 113-44.

33. Fredlund, D. G., Krahn, J. and Pufahl, D. E. (1981). *The relationship between Limit Equilibrium Slope Stability Methods*. Proc. Of the 10th ICSMFE, Vol. 3, Stockholm, Sweden, pp. 409-16.

34. Fredlund, D. G. and Krahn, J. (1977). *Comparison of slope stability methods of analysis*. Canadian Geotechnical Journal, Vol. 14, pp. 429-39.

35. Fichtner J. V. (2005). *Piezometer records for Dam site LB and Powerhouse slopes.* Middle Marsyangdi Hydroelectric Project.

36. Fichtner J. V. (2003). *Revised construction drawings*. Middle Marsyangdi Hydroelectric Project.

37. Fichtner J. V. (2001). *Tender Design Report Vol. 5*. Geological Report, Middle Marsyangdi Hydroelectric Project.

38. Fichtner J. V. (2001). *Stage 2 Detailed Design, Powerhouse area*. Middle Marsyangdi Hydroelectric Project.

39. Fichtner J. V. (2000). *Basic Design Memorandum*. Middle Marsyangdi Hydroelectric Project.

40. Fichtner J. V. (2000). *Detailed Engineering Study, Geotechnical Investigations*. Report on Soil Investigation, Middle Marsyangdi Hydroelectric Project.

41. Goodman, R. E. (1993). *Soluble Rocks: Limestone, Dolomite and Evaporates*. Engineering Geology, Rock in Engineering Construction, Publisher John Wiley & Sons, Inc., pp. 143-58.

42. Grande, L. (1997). *Skråningsstabilitet.* Kompendium Geoteknikk 2, grunnkurs. Norges teknisk- naturvitenskapelige universitet, NTNU (In Norwegian).

43. Grande, L. and Waterman, D. (2005). *Phreatic level correction in PLAXIS.* Personal communications and discussions for adjustment of phreatic surface of inclined groundwater table for stability analysis (lars.grande@ntnu.no, support@plaxis.nl).

44. Head, K. H. (1989). *Soil Technicians' Handbook*. Pentech, Press, London, John Willey & Sons, New York, Toronto.

45. Head, K. H. (1985). *Manual of Soil Laboratory testing*. Vol. 3, Effective stress tests, Pentech, Press, London, John Willey & Sons, New York, Toronto.

46. Hurlbut, C. S. and Sharp, W. E. (1998). *Dana's Minerals and How to Study Them*. Fourth Edition, pp. 197-99.

47. Hutchinson, J. N. and Sarma, S. K (1985). *Discussion of 3D- limit equilibrium analysis of slopes, by H. R. Chen and. L. Chameau.* Geotechnique, London, 35 (2), pp. 215-16.

48. ICOLD (1989). *Selecting Seismic Parameters for Large dam.* Design Guidelines, Bulletin 72.

49. Janbu, N. (2001). *Slope Stability Procedures used in Landslide Evaluations in Practice.* Landslide Journal of the Japanese Landslide Society, Vol. 38, No 3, pp. 161– 68.

50. Janbu, N. (1996). *Slope Stability Evaluations in engineering practice.* 7th International Symposium on Landslides, Trondheim, Norway, Vol. 1 pp. 17-34.

51. Janbu, N. (1973). *Slope Stability Computations*. Embankment Dam Engineering, Casagrande Volume, pp. 47-86.

52. Janbu, N. (1970). *Beregning av relativdeformasjonen*. Grunnlag i geoteknikk (In Norwegian). Tapir Forlag, pp. 181-82.

53. Janbu, N. (1968). *Slope Stability Computations*. (Geoteknikk, NTH). Soil Mechanics and Foundation Engineering, Technical University of Norway.

54. Janbu, N. (1963). *Soil compressibility as determined by oedometer and triaxial tests.* III European Conference on Soil Mechanics and Foundation Engineering (ECSMFE), Wiesbaden, Germany. Proceedings, Vol. 2 (1), pp. 129-36.

55. Janbu, N. (1957). *Earth pressure and bearing capacity calculations by generalised procedure of slices*. Proceedings of the 4th International Conference, SMFE, London, 2, pp. 207-12.

56. Janbu, N. (1954a). *Stability analysis of Slopes with Dimensionless Parameters*. Thesis for the Doctor of Science in the Field of Civil Engineering, Harvard University Soil Mechanics Series, No. 46.

57. Janbu, N. (1954b). *Application of Composite Slip Surface for Stability Analysis.* European Conference on Stability of Earth Slopes, Stockholm.

58. Kezdi, A. (1980). *A Hand book of Soil Mechanics.* Vol 2, Soil Testing, Elsevier Scientific Publishing Company, Amsterdam, Oxford, New York.

59. Kezdi, A. (1974). *A Hand book of Soil Mechanics*. Soil Physics Vol 1, Elsevier Scientific Publishing Company, Amsterdam, Oxford, New York, p. 32.

60. Krahn, J. (2004). *Stability Modelling with SLOPE/W*. An Engineering Methodology, Published by GeoSlope International.

61. Krahn, J. (2003). *The limits of limit equilibrium analysis*. Canadian Geotechnical Journal, Vol. 40, pp. 643-60.

62. Kramer, S. (1994). *Damping and surface waves*. Geotechnical Earthquake Engineering.

63. Ladd, R. S. (1978). *Preparing Test Specimens Using Undercompaction*, Geotechnical testing Journal, GTJODJ, Vol. 1, No. 1, pp. 16-23.

64. Leroueil, S. and Hight, D. W. (2003). *Behaviour and properties of natural soils and soft rocks*. International Workshop on Characterisation and engineering properties of natural soils, Singapore, 2-3 Dec. 2002. Proceedings, Vol. 1, p. 133.

65. Leshchinsky, D., and Baker, R. (1986). *Three dimensional slope stability*: end effects. Journal Soils and Foundations, 26 (4), pp. 98-110.

66. Leshchinsky, D., and Huang, C. (1992). *Generalised three dimensional slope stability analyses*. Journal Geotech. Engg., ASCE, 118 (11), pp. 1748-64.

67. Lowe, J., and Karafiath, R. V. (1960). *Stability of Earth Dam upon Drawdown*. Proceedings of the of the first Pan American Conference on Soil Mechanics and Foundation Engineering, Maxico City, pp. 537-52.

68. Melinda, F., Rahardjo, H., Han, K. K., and Leong E. C. (2004). *Shear Strength of Compacted Soil under Infiltration Condition.* Journal of Geotechnical and Geoenvironmental Engineering, Vol. 130 (8), pp. 807-17.

69. Ministry of Water Resources (MWR) (2003). *Nepal Country Report presented by Minister for Water Resources.* The 3rd World Water Forum, Kyoto.

70. Mitchell, J. K. (1993). *Soil Mineralogy and Behaviour of Minerals*. In Fundamentals of Soil Behaviour, Second edition, Published by John Wiley & Sons, Inc.

71. Morgenstern, N. R. and Price, V. E. (1965). *The Analysis of the Stability of General Slip Surfaces*. Geotechnique, Vol. 15, No. 1 pp. 77-93.

72. Nash, D. (1987). *Comprehensive Review of Limit Equilibrium Methods of Stability Analysis*. Slope Stability, Chapter 2. M. G. Andersen and K. S. Richards, Eds. New York: Wiley, pp. 11-75.

73. NEA Lab. (2001). *Report on Additional Soil Investigation.* Middle Marsyangdi Hydroelectric Project. Soil, Rock and Concrete Laboratory, NEA, Kathmandu.

74. NEA Lab. (2000). *Middle Marsyangdi Hydroelectric Project*. Detail Engineering Study, Geotechnical Investigation, Report on Soil investigation. Soil, Rock and Concrete Laboratory, NEA, Kathmandu.

75. Nepal, K. M. and Olsson R. (2001). *Geological and Foundation Studies for Spillway Dam.* Middle Marsyangdi Hydroelectric Project, Central Nepal. Workshop on Rock Mechanics and Tunnelling Techniques, Kathmandu, Nepal, 10-12 September, 2001.

76. Norwegian Geotechnical Institute (NGI) (2001). *Seismic slope stability*. Technical Note 2, Middle Marsyangdi Hydroelectric Project, Nepal.

77. Norwegian Geotechnical Institute (NGI) (2001). *Laboratory Test Results*. Middle Marsyangdi Hydroelectric Project, Nepal.

78. Norwegian Standard (NS) (1982): *Geotekniske proving*. Laboratoriemetoder - Jords oppbygning. Begreper, terminologi og symboler (NS 8010) , og Korndensitet (NS 8012).

79. Nordal, S. (2002). *Elasto-plasticity*. Course materials for Geotechnical Constructions, Geotechnical Division, NTNU, Norway.

80. Nordal, S. and Glaamen, M. G. (2004). *Some examples of slope stability evaluations from Norwegian geotechnical practice*. Geotechnical Innovations, Edited by Brinkgreve, R. B. J., Schad, H., Schweiger, H. F. and Willand, E., pp. 347-63.

81. Nordal, S., and Kramer, S. (2003). *Geodynamics*. Teaching materials for PhD Course BA 8300. Geotechnical Division, NTNU, Norway.

82. NSCN (1994). *National Seismological Network Nepal*. Ministry of Industry, DMG, Nepal.

83. Perkins, D. (1998). *X-ray Diffraction*. Mineralogy, University of North Dakota, Prentice Hall, New Jersey, pp. 258-77.

84. PLAXIS (2004). *Finite Element Code for Soil and Rock Analyses*. PLAXIS-2D Version 8, Reference Manual, Edited by Brinkgreve, et al., DUT, the Netherlands. www.plaxis.nl.

85. Sandven, R. (2003). *Geotechnical field and laboratory tests*. Geotechnics, material properties, Course material SIB 2020, Geotechnical Division, NTNU.

86. Sandven, R. and Svaan, O. (1993). *Laboratorium for Geoteknikk*. Veileding for Gejennomføring av Permeabilitetsforsøk, Utstyrsbeskrivelse, Forsøksrutiner (In Norwegian).

87. Sandven, R. (1992). *Incremental Oedometer test*. Test routines, Application of software, Institute for Geotechnic, Norwegian University of Science and Technology.

88. Sarma, S. K. (1973). *Stability Analysis of Embankment and Slopes*. Geotechnique, Vol. 23 (3), pp. 423-33.

89. SLEEP/W (2005). *Seepage analyses*. Software permitted for limited period of use by GeoSlope Office, Canada, (lorin@geo-slope.com), www.geoslope.com.

90. SILT Consultant (2001). *Additional Soil Investigation*. Middle Marsyangdi Hydroelectric Project, Nepal.

91. SLIDE (2003). *Stability analysis for soil and rock slopes*. Slide, User's Guide, Geomechanics Software Solutions, Rocscience Inc., Canada. www.rocscience.com.

92. SLOPE/W (2002). *Stability Analysis*. Users Guide Version 5, GeoSlope Office, Canada. www.geoslope.com.

93. Spencer, E. (1967). *A method of Analysis of the Stability of Embankments, Assuming Parallel Interslice Forces.* Geotechnique, Vol. 17, pp. 11-26.

94. Skinner B. J., Porter S. C. (2000). *The Dynamic Earth*. An Introduction to Physical Geology, 4th Edition, Published by John Willey and Sons, Inc., pp. 74, 125-26.

95. Statens vegvesen (1997). *Laboratory Investigations*. Handbook 014 and 015 (in Norwegian), Published by Norwegian Road Authorities.

96. Thielen, A., Friedel, S., Plotze, M. and Springman, S.M. (2005). *Combined approach for site investigation in terms of the analysis of rainfall induced landslides*. Proceedings of the 16th Int. Conf. on Soil Mechancis and Geotechnical Engineering, Osaka Japan, p. 2591.

97. Taylor, M. J. and Burns, S. F. (2005). *Slope and seismic stability of Castle Lake Debris Dam, St. Helens, Washington*. Landslide and Avalanches: ICFL 2005 Norway, Edr. Senneset, Flaate and Larsen.

98. Wenk, H. R. and Bulakh, A. (2003): *Minerals, Their Constitution and Origin*. Cambridge Universality Press, pp. 365-75.

99. Wood, D. M. (1990). *Soil Behavior and Critical State Soil Mechanics*. Soil testing: Stress and strain variables, Cambridge University Press, pp. 16–25.

100. Yamanaka, H. and Iwata, S. (1982). *River terraces along the middle Kali Gandali and Marsyangdi Khola, Central Nepal*. Journal of Nepal Geological Society, Vol. 2, Special Issue, pp. 95-111.

101. Vucetic, M. and Dobry R. (1991). *Effect of soil plasticity on cyclic response*. Journal of Geotechnical Engineering, ASCE, Vol 117 No 1, pp. 89–107.

List of literatures

102. Andersen, M. and Richards, K. S. (1987). *Modelling of slope stability: the complimentary nature of geo-technical and geo-morphological approaches.* Slope Stability, Geo-technical Engineering and Geomorphology, Published by John Wiley & Sons, Inc, pp. 1-9.

103. Deer, W. A., Howie, R. A. and Zussman, J. (1996). *An Introduction to the Rock Forming Minerals*. Second Edition, Printed in Honkong.

104. Lahmeyer International (1998). *Upgrading of Feasibility Study Report*. Addendum No.3, Geology and Geotechnics, Middle Marsyangdi Hydroelectric Project, Nepal.

105. Lahmeyer International (1997). *Upgrading of Feasibility Study Report*. Vol.3.6, Geology and Geotechnics, Middle Marsyangdi Hydroelectric Project.

106. Larsen, J. O. (2002). *Some aspects of physical and weather related slope processes*. A Doctoral Thesis summated to the Norwegian University of Science and Technology.

107. Larsen, J. O., Okamoto, T., Matsuura, S., Grande, L. and Asano, S. (2002): *Slope stability related to weather parameters in a quick clay deposit*. An article submitted to the Canadian Geotechnical Journal, (Article 4, and Doctoral Thesis by Larsen).

108. Larsen, J. O., Okamoto, T., Matsuura, S., Grande, L. and Asano, S. (1999). *Slide activity in Quick clay related to Porepressure and Weather parameters*, (Article 3, Doctoral Thesis by Larsen).

109. Okamoto, T. S., Asano, S. Matsuura S. and Larsen, J. O. (1999). *Monitoring of Slope Failure in a Quick clay Deposit Area*. Journal of Japan Landslide Society, 36-2 (In Japanese), (Article 2, Doctoral Thesis by Larsen 2002).

110. Olsson, R. (2001). *Fjellsprengningskonferansen*. Bergmekanikkdagen og Geotecknikkdagen, (In Norwegian), pp. 38-1 to 19.

111. Pandey, M. R., Chitrakar, G. R., Kafle, B. Sapkota, S. N., Rajaure, S. and Gautam, U. P. (2002). *Seismic Hazard Map of Nepal*. Department of Mines and Geology, National Seismological Centre, Kathmandu, Nepal.

112. Pascual, P. (2001). *Overview of a Micro-scale Study of the Causes and Effects of Landslides in the High Himalaya.* Newsletter No 40 published by, and ICIMOD, NEPAL.

113. Tadesse S. (2000). *Behaviour of Saturated Sand under Different Triaxial Loading and Liquefaction*. PhD thesis. Norwegian University of Science and Technology, NTNU.

114. Tianch, L. (2001). *Risk, Hazard and Vulnerability*. Newsletter No 40, ICIMOD, Nepal.

115. Wille Goetechnikk GmbH (1999). *Operating Instruction Manual*. Triaxial equipment, prepared by Wille Geoteknikk GmbH, Germany.

116. Yang, S. (2004). *Characterization of the properties of sand-silt mixtures*. A Doctoral Thesis NTNU, pp. 53-58.

117. Youngs, R. R. et al. (1997). *Strong ground motion attenuation relationship for subduction zone earthquakes*. Seismological Research Letters, Vol. 68, No. 1, pp. 59-73.